From Fauna to Flames

Remote Sensing with Scheimpflug Lidar

Malmqvist, Elin

2019

Document Version:
Publisher's PDF, also known as Version of record

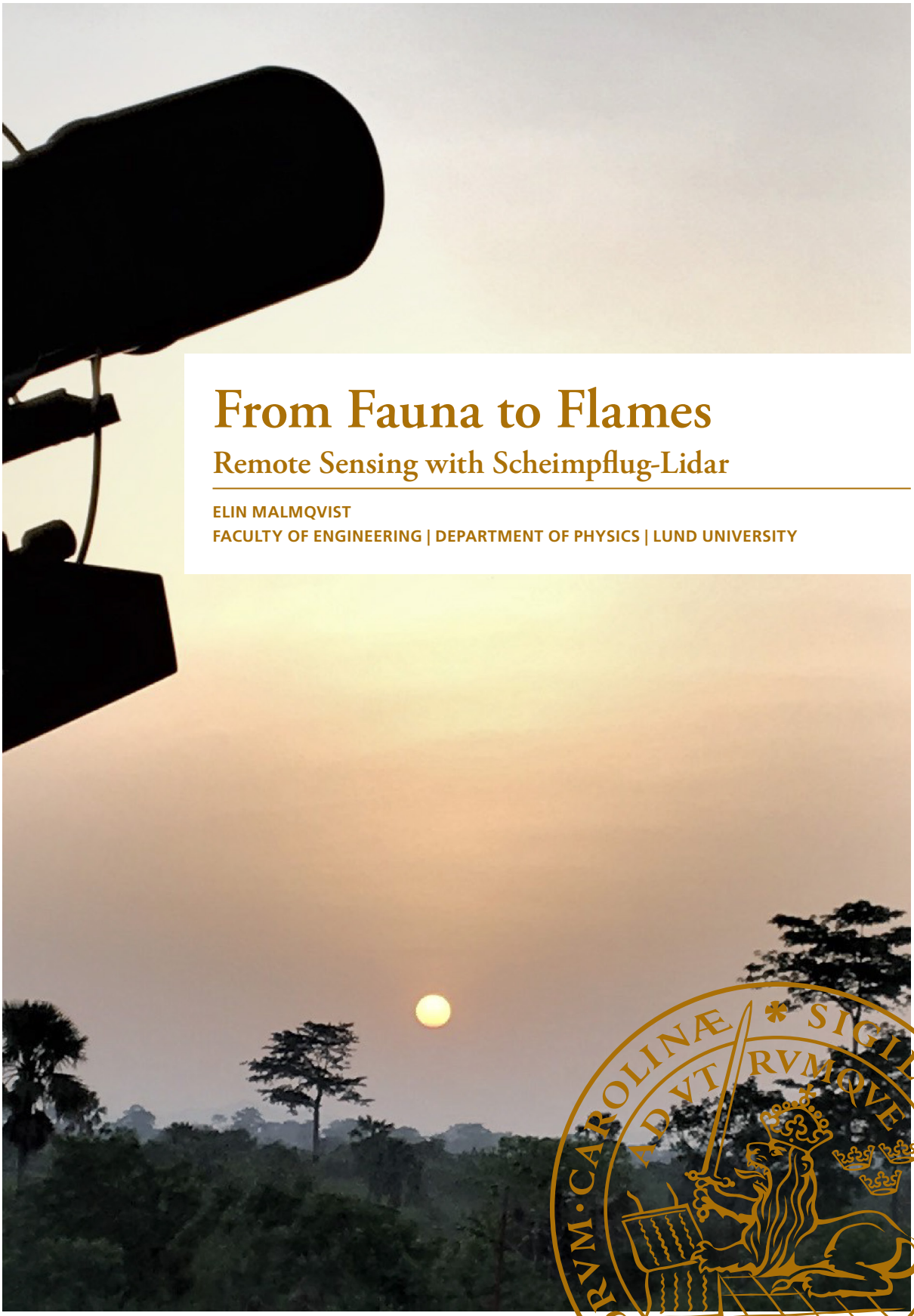

From Fauna to Flames

Remote Sensing with Scheimpflug-Lidar

ELIN MALMQVIST
FACULTY OF ENGINEERING | DEPARTMENT OF PHYSICS | LUND UNIVERSITY

From Fauna to Flames

Remote Sensing with Scheimpflug-Lidar

Elin Malmqvist

LUND
UNIVERSITY

DOCTORAL DISSERTATION
by due permission of the Faculty of Engineering, Lund University, Sweden.
To be defended at Rydbergsalen, Fysicum, Professorsgatan 1.
29th March 2019 at 09.15.

Faculty opponent
Prof. Xinzhao Chu, Department of Aerospace Engineering Sciences,
University of Colorado, Boulder, Colorado, USA

Organization: LUND UNIVERSITY Division of Combustion Physics, Department of Physics P.O Box 118, SE-211 00 Lund, Sweden	Document name: Doctoral Dissertation
	Date of issue: 2019-02-18
Author: Elin Malmqvist	CODEN: LUTFD2/TFCP-218-SE
	Sponsoring organization

Title: From Fauna to Flames Remote Sensing with Scheimpflug-Lidar

Abstract

This thesis presents applications of the Scheimpflug Lidar (S-Lidar) method. The technique has been applied to combustion diagnostics on a scale of several meters as well as fauna detection and monitoring over distances of kilometers. Lidar or laser radar is a remote sensing technique where backscattering of laser light is detected with range resolution along the direction of the laser beam. It is an established method in e.g. atmospheric sensing where it is used to map and monitor gases and aerosols. In contrast to conventional Lidar, which uses a time-of-flight approach, Scheimpflug Lidar uses imaging to achieve range resolution. The laser beam transmitted from the Lidar system is sharply imaged onto a detector, resulting in range resolution along the sensor. This is done by placing the laser beam, the collection optics and the detector according to two trigonometrical conditions called the Scheimpflug and hinge rules. This kind of Lidar technique enables the use of small, continuous-wave diode lasers and line-array detectors with kHz sampling rates.

A general description of the equations governing the achievable measurement range and resolution of S-Lidar are presented. The way the equations relate to the conventional Lidar equation is also discussed as well as the impact of the beam width. The instrumentation and experimental considerations for far range S-Lidar for aerial fauna monitoring are described and some temporally and spatially resolved data from field campaigns in Africa, China and Sweden are presented. A method used to reduce and analyze the large amount of collected data is also described.

For the short-range applications, down-scaled versions of the system were developed. These systems are described as well as their applications. The short range system has mostly been used to investigate the potential of the technique to be applied for combustion diagnostics, and results from measurements in flames using both elastic and inelastic optical techniques, such as Rayleigh scattering and two-line atomic fluorescence are presented. A hyperspectral Lidar system aimed at aquatic applications is also presented.

Key words: Lidar, Laser radar, Scheimpflug Lidar, Combustion diagnostics, Entomological Lidar

Classification system and/or index terms (if any)

Supplementary		Language: English
ISSN and key title: 1102-8718		ISBN (print): 978-91-7753-995-7 ISBN (pdf): 978-91-7753-996-4
Recipient's notes	Number of pages: 212	Price
	Security classification	

From Fauna to Flames

Remote Sensing with Scheimpflug-Lidar

Elin Malmqvist

LUND
UNIVERSITY

Front cover photo by Elin Malmqvist

Back cover photo by Hugh Sturrock (mosquito) and Alexios Matamis (flame)

Faculty of Engineering
Department of Physics
Lund University

Lund Reports on Combustion Physics, LRCP-218
ISBN 978-91-7753-995-7 (print)
ISBN 978-91-7753-996-4 (pdf)
ISSN 1102-8718
ISRN LUTFD2/TFCP-218-SE

Printed in Sweden by Media-Tryck, Lund University
Lund 2019

Media-Tryck is an environmentally certified and ISO 14001:2015 certified provider of printed material.
Read more about our environmental work at www.mediatryck.lu.se

MADE IN SWEDEN

"Light thinks it travels faster than anything but it is wrong.
No matter how fast light travels,
it finds the darkness has always got there first,
and is waiting for it."

Terry Pratchett, Reaper Man

"Eternity is a terrible thought. I mean,
where's it going to end?"

Tom Stoppard, Rosencrantz and Guildenstern Are Dead

Content

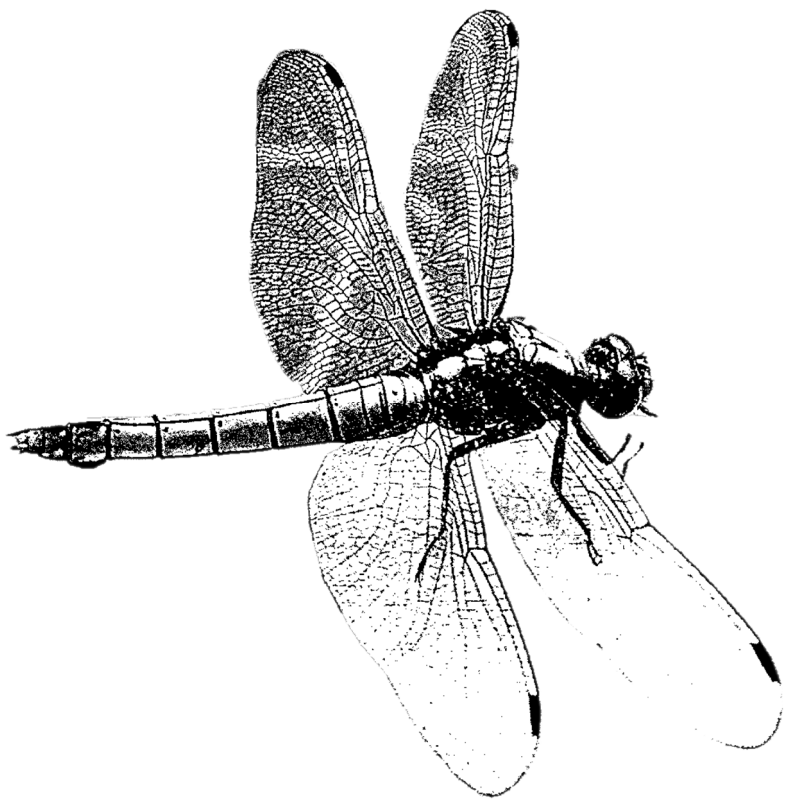

Abstract

This thesis presents applications of the Scheimpflug-Lidar (S-Lidar) method. The technique has been applied to combustion diagnostics on a scale of several meters as well as fauna detection and monitoring over distances of kilometers. Lidar or laser radar is a remote sensing technique where backscattering of laser light is detected with range resolution along the direction of the laser beam. It is an established method in e.g. atmospheric sensing where it is used to map and monitor gases and aerosols. In contrast to conventional Lidar, which uses a time-of-flight approach, Scheimpflug Lidar uses imaging to achieve range resolution. The laser beam transmitted from the Lidar system is sharply imaged onto a detector, resulting in range resolution along the sensor. This is done by placing the laser beam, the collection optics and the detector according to two trigonometrical conditions called the Scheimpflug and hinge rules. This kind of Lidar technique enables the use of small, continuous-wave diode lasers and line-array detectors with kHz sampling rates.

A general description of the equations governing the achievable measurement range and resolution of S-Lidar are presented. The way the equations relate to the conventional Lidar equation is also discussed as well as the impact of the beam width.

The instrumentation and experimental considerations for aerial fauna monitoring with S-Lidar are described and some temporally and spatially resolved data from field campaigns in Africa, China and Sweden are presented. A method used to reduce and analyze the large amount of collected data is also described.

For the combustion applications, down-scaled versions of the system were developed. These systems are described as well as their applications. These short range system has mostly been used to investigate the potential of the technique to be applied for combustion diagnostics, and results from measurements in flames using both elastic and inelastic optical techniques, such as Rayleigh scattering and two-line atomic fluorescence are presented. A hyperspectral Lidar system aimed at aquatic applications is also presented.

Populärvetenskaplig sammanfattning

Tänk dig att du är ute i skogen och campar. Natten utanför är kolsvart så du använder en ficklampa när du går ut ur tältet. När du riktar ljusstrålen från lampan ut i natten ser du plötsligt träden och snåren som omger dig. Anledningen till detta är, så klart, att ljuset från lampan har träffat träden och studsat tillbaka till dina ögon. Efter en stund inser du att ljuset inte bara studsar på trädens solida stammar, utan även på nattdimmans svävande vattendroppar och på luftens molekyler, vilket gör att du faktiskt kan se hela ljusstrålen. Då och då ser du också starka ljusglimtar när flygande insekter korsar ljusstrålen eller när större regndroppar faller genom den.

Facktermen för det du precis ägnat dig åt är aktiv optisk fjärranalys, dvs du har, genom att använda en ljuskälla, fått upplysningar om avlägsna objekt som döljer sig i det omgivande mörkret. Detta har skett genom att en del av ficklampans ljus har spridits tillbaka och samlats in av dina ögon. Din hjärna har sedan omvandlat denna ”signal” till information om omvärlden så som ”Där står ett träd med en mörk stam”, ”Där borta hänger en blå tröja”, och ”Luften är fuktig ikväll”. Det du har gjort är väldigt likt fladdermöss och delfiners ekolokalisering som låter dem navigera och jaga i ljusfattiga miljöer. Istället för ljus så skickar dessa djur ut ljudvågor med bestämda egenskaper och de resulterande ekona samlas in och analyseras av speciellt utvecklade hörselorgan. Dessa kan sedan ge djuren information om avstånd till och rörelse hos omgivande objekt. Skillnaden mellan din nattliga utforskning av skogen och dessa djurs ekolokalisering är framförallt egenskaperna hos de utskickade vågorna och din (o)förmåga att analysera signalen.

Tänk dig nu att vi istället för ficklampan, använde en ljuskälla som skickar ut ljus med välkända egenskaper i tid och rum, och att det bakåtspridda ljuset samlats in med en kamera och sparats på en dator. Genom att analysera signalen på rätt sätt så hade vi potentiellt kunnat fastställa det exakta avståndet till trädet vi lyser på, eller kanske identifiera positionen hos alla insekter som flyger genom strålen varje sekund. Om vi vet tillräckligt mycket om ljusets egenskaper och hur det växelverkar med olika sorters material så kan vi inte bara identifiera de avlägsna trädets position utan också potentiellt erhålla information om dess storlek och sammansättning på molekylnivå. Detta är precis vad man gör i den optiska fjärranalysmetoden Lidar, även ibland kallad laser-radar. En laserstråle som består av ljus med bestämd riktning, energi och tidsegenskaper skickas ut i atmosfären och det ljus som sprids tillbaka av objekt i stålen, så som partiklar och molekyler, detekteras med tids-och rumsupplösning. I denna avhandling används en Lidarmetod som kallas Scheimpflug-Lidar. I denna metod så skickas en laserstråle

ut i atmosfären och sedan avbildar man bakåtspridningen från strålen på en kamera. Mätningarnas rumsupplösning fås genom att varje bildelement, eller pixel, på kamerachipet kommer avbilda en viss del av strålen, och tidsupplösning erhålls genom att man tar många bilder i sekunden.

För att kunna ta en skarp bild av stålen så kan man inte använda sig av en vanlig kamerauppställning. Om du försöker ta en bild av ett långt objekt som inte är parallellt med objektivet, så som vår utskickade laserstråle, kommer bara en liten del av objektet bli skarpt på bilden. Om man vill få bra skärpa längs objektet så kan man dock vinkla objektivet enligt en optisk regel som kallas Scheimpflugprincipen. Principen är, lite felaktigt, döpt efter den österrikiska armékaptenen Theodor Scheimpflug, som använde principen för att korrigera perspektivet i flygbilder tagna från luftballonger runt förra sekelskiftet. Principen hade tidigare beskrivits av en ingenjör vid namn Jules Carpentier, vilket Scheimpflug också refererar till i sitt patent från 1904. Scheimpflugs bidrag var att han formulerade ytterligare begränsningar som garanterar skärpa längs objektet. I Scheimpflug-Lidar arrangeras utrustningen, dvs kameran, objektivet och laserstrålen, enligt dessa regler. Man kan därefter skarpt avbilda bakåtspridningen från en laserstråle som sträcker sig från några meter till flera kilometer.

I detta arbete så har Scheimpflug-Lidar använts för att, på avstånd, samla in information om atomer och molekyler i gaser, oftast i en förbränningstillämpning. Precis som spridningen från luftens partiklar kunde ses när ficklampan lyste ut i skogen så kan vi nu detektera spridningen från molekylerna i t.ex. en eld, och från denna bestämma egenskaper som t.ex. temperatur och koncentration med rumsupplösning. Fördelen med Scheimpflug-Lidar tekniken är att den kan mäta på stora mätvolymer med begränsad åtkomst. Genom att kombinera Lidar med etablerade mätmetoder så kan information från sådana miljöer erhållas och sedan användas för att göra förbränningsprocessen mer effektiv och mer miljövänlig.

Faktumet att du, under din nattliga utforskning av skogen med ficklampan, ser snabba glimtar av flygande insekter i ljusskenet är jämförbart med den andra tillämpningen av Scheimpflug-Lidar som diskuteras i avhandlingen. Metoden har använts för att övervaka aktiviteten hos flygande insekter i atmosfären på flera platser runt om i världen. När insekter flyger genom laserstrålen så ger detta en hög signal på det specifika avståndet. Antal insekter som flyger genom strålen kan därför räknas och deras rörelsemönster kan utforskas. Egenskaper så som hur snabbt en insekt slår med sina vingar kan också fastställas eftersom vingarnas rörelse syns som periodiska blinkningar på signalen. Detta kan t.ex. ge ledning om insektens art och kön. Kunskap om insekters beteende är av grundläggande värde för biologisk och ekologisk forskning, men har även ekonomiskt och humanitärt värde. Om vi tillexempel vet när skadeinsekter är aktiva så kan jordbrukare använda bekämpningsmedel mer effektivt, och därmed spara pengar och producera mer livsmedel. Kunskap om rörelsemönstret hos insekter som sprider sjukdomar, så som Malariamyggor, kan hjälpa till att utveckla bättre och billigare förebyggande åtgärder för dessa sjukdomar, och i och med det rädda liv.

List of papers

I. **E. Malmqvist**, S. Jansson, S. Török, M. Brydegaard, "Effective parameterization of laser radar observations of atmospheric fauna", IEEE Journal of Selected Topics in Quantum Electronics, 22(3), May/June 2016, DOI: 10.1109/JSTQE.2015.2506616

II. G. Zhao, M. Ljungholm, **E. Malmqvist**, G. Bianco, L.A, Hansson, S. Svanberg, M. Brydegaard. "Inelastic hyperspectral Lidar for profiling aquatic ecosystems", Laser and Photonics Review, 10(5), 807-813, 2016, DOI: 10.1002/lpor.201600093

III. M. Brydegaard, **E. Malmqvist**, S. Jansson, J. Larsson, S. Török, G. Zhao. "The Scheimpflug Lidar method" SPIE Proceedings, 10406, 2017, DOI: 10.1117/12.2272939

IV. **E. Malmqvist**, S. Jansson, S.Zhu, Li, W, Svanberg, K, Svanberg, J. Rydell, Z. Song, J. Bood, M. Brydegaard, S. Åkesson. "The bat-bird-bug battle: Daily flight activity of insects and their predator over a rice field revealed by high-resolution Scheimpflug Lidar", Royal Society Open Science, 5(4), 2018, DOI:10.1098/rsos.172303

V. **E. Malmqvist**, M. Brydegaard, M. Aldén, J. Bood. "Scheimpflug Lidar for combustion diagnostics", Optics Express, 26(12), 14842-14858, 2018, DOI: 10.1364/OE.26.014842

VI. **E. Malmqvist**, J. Borggren, M. Aldén, J. Bood. "Lidar thermometry using two-line atomic fluorescence", Applied Optics, 58(4), 1128-1133, 2019, DOI: 10.1364/AO.58.001128

Related work

VII. **E. Malmqvist**, M. Jonsson, K. Larsson, M. Aldén, J. Bood, "Two-dimensional OH-thermometry in reacting flows using photofragmentation laser-induced florescence thermometry", Combustion and Flame, 169, 297-306, 2016, DOI: 10.1016/j.combustflame.2016.05.002

VIII. S. Zhu, **E. Malmqvist**, W. Li, S. Jansson, Y. Li, Z. Duan, K. Svanberg, H. Feng, Z. Song, G. Zhao, M. Brydegaard, S. Svanberg "Insect abundance over Chinese rice fields in relation to environmental parameters, studied with a polarization-sensitive CW near-IR Lidar system", Applied Physics B: Lasers and Optics, 123(7), 1-11, 2017, DOI: 10.1007/s00340-017-6784-x

IX. G. Zhao, **E. Malmqvist**, S. Török, P.E. Bengtsson, S. Svanberg, J. Bood, and M. Brydegaard. "Particle profiling and classification by a dual-band continuous-wave lidar system" Applied Optics, 57(35), 10164-10171, 2018, DOI: 10.1364/AO.57.010164

X. M. Brydegaard, J. Larsson, S. Török, **E. Malmqvist**, G. Zhao, S. Jansson, M. Andersson, S. Svanberg, S. Åkesson, F. Laurell. "Short-Wave infrared atmospheric Scheimpflug lidar", EPJ Web of Conferences 176, ILRC28, 2018, DOI: 10.1051/epjconf/201817601012

Abbreviations

Charge Couple Device	CCD
Complementary Metal Oxide Semiconductor	CMOS
Continuous Wave	CW
Degree of Linear polarization	DoLP
Degrees of Freedom	DoF
Differential Absorption Lidar	DIAL
femtometer	fm
Field of View	FoV
Full Width Half Max	FWHM
Height Above Burner	HAB
Infrared (700nm-1mm)	IR
Intensified Charge Couple Device	ICCD
Interquartile range	IQR
kilohertz	kHz
Laser Diode	LD
Laser-Induced Fluorescence	LIF
Light Emitting Diode	LED
Near Infrared (700-1000 nm)	NIR
One dimensional	1D
Optical Cross Section	OCS
picometer	pm
Radar Cross Section	RCS
Scheimpflug Lidar	S-Lidar
Short Wave Infrared (1000-2500 nm)	SWIR
Three Dimensional	3D
Time-of-Flight	ToF
Two Dimensional	2D
Two-Line Atomic Fluorescence	TLAF
Ultra Violet (<400 nm)	UV
Visible (400-700 nm)	VIS

Chapter 1

Introduction

1.1 Remote sensing

Imagine that you are standing by a road in a hilly landscape and a car is approaching you in the distance. While the car is still obscured by the landscape, the sound it produces informs you of its presence and that it is moving towards you with a high velocity. When the car is within visible range, this information is confirmed by your eyes and you can tell that the car has a shiny red color and a sleek shape. Without physically touching the car, you have acquired information about its properties and movements. This is a very basic example of remote sensing, i.e. obtaining information about the surrounding world without physically probing it. Human hearing and eye sight are both based on *passive* remote sensing. That means that the sound or light waves transferring the information from the object of interest, i.e. the car, to the sensors, your ears and eyes, are not transmitted by yourself, but originates from a source in the environment around you. Some animals have senses based on *active* remote sensing, where information about the surroundings is obtained from waves transmitted by the animal itself. Two well-known examples are the echolocation, or bio-sonar, used by dolphins and bats to navigate and hunt prey in low-light environments. The animals transmit sound waves with well characterized properties into their environment and the resulting echoes may provide information about the distance to and possibly the velocity of an object. Another animal that uses active remote sensing is a deep-sea fish called the Stoplight loosejaw [1]. It transmits a beam of red bioluminescent light and utilizes it to find prey in the darkness. Since the eyes of most creature living in the deep-sea are insensitive to red wavelengths, the beam is invisible to both their prey and potential predators.

As seen by the examples above, active remote sensing enables us to retrieve information from environments where we otherwise would have been blind. Active techniques also tend to provide more precise information than passive techniques, since

the source and properties of the transmitted waves are better known than those from an external source.

Thanks to technology, humans can also use active remote sensing. A simple example of active optical remote sensing would be if the aforementioned car was approaching you in the dark, and you used the light from a flash lamp to see it. Optical remote sensing is, in fact, used in many applications in both industry and research. The signal is then collected by specialized optics, detected by a sensor, sensitive in an appropriate wavelength region, and saved into a memory. The measurement volume will be defined by the overlap between the field-of-view (FoV) of the sensor and the volume into which the light is transmitted. If the properties of the transmitted light and the receiver are well-known, it is possible to acquire spatially and temporally resolved information from the measurement volume.

The active optical remote sensing technique used throughout the current work is called Lidar (Light Detection And Ranging). In Lidar, backscattered light from a transmitted laser beam is detected with range resolution. With Lidar, it is possible to extract information about a probe volume stretching over many kilometers, due to the well-defined spatial, temporal and spectral properties of laser light. It is an established method in the atmospheric research community, where it is used to monitor and characterize e.g. temperature, wind speed as well as molecular and particulate species. Other applications include mapping of topography of land and oceans, monitoring vegetation in forestry, land cover, and ecological research. The principles and some applications of Lidar are described in e.g. [2–9].

Conventional Lidar is based on a time-of-flight (ToF) approach to achieve ranging. Short laser pulses (often ns-scale) are transmitted into the atmosphere and the backscattered signal is detected with time resolution. The speed of light is then used to convert measured arrival time into distance. Thus, ToF-Lidar is based on a similar concept as Radar (Radio detection and ranging) [10,11], but the wavelengths used in Lidar are typically 10,000-100,000 times shorter, and thereby provides much higher resolution than Radar. The concept was developed parallel to the development of lasers, starting in the 1960s.

Scheimpflug-Lidar (S-Lidar) [12–15] is a new Lidar concept, which is not based on the ToF approach to achieve range resolution. Instead, it uses an approach reminiscent of the very starting point of the Lidar development, which was prior to the invention of the laser. This origin lies in triangulation efforts done in the 1930s to 1950s using continuous-wave searchlights to measure e.g. cloud height and particle distributions in the atmosphere, see e.g. [16–18]. In S-Lidar, the detector, collection optics and laser beam are placed according to the Scheimpflug condition and the hinge rule, which ensure that the focus plane of the camera lies along the laser beam. This means that the laser beam can be sharply imaged onto the detector with range resolution along one spatial direction. Continuous-wave (CW) diode lasers may thus be employed, enabling a compact setup with a sampling rate limited by the read-out rate of the detector. In many of the current works, S-Lidar has been applied to biological applications [19–

22], including Papers I-IV, but the technique has also been developed and applied to atmospheric research such as particle detection [12,13,23–25], differential absorption Lidar (DIAL) measurements [26] and combustion diagnostic (Papers V and VI).

1.2 Motivation

The PhD work presented in this thesis was divided into two different projects, one focused on aerial fauna applications of S-Lidar and one on combustion applications. The aerial fauna, particularly insects, have been monitored and detected over distances of kilometers. While the combustion diagnostics, i.e. remote detection of signals from species in gas phase, has been carried out from a distance of several meters. As illustrated by Fig. 1.1, the measurement targets in this work thus span over a wide range of sizes, extending from indium atoms and molecules with picometer (pm) or nanometer (nm) size to birds and bats, with a size of approximately a decimeter. Motivations for each project are discussed in the next section.

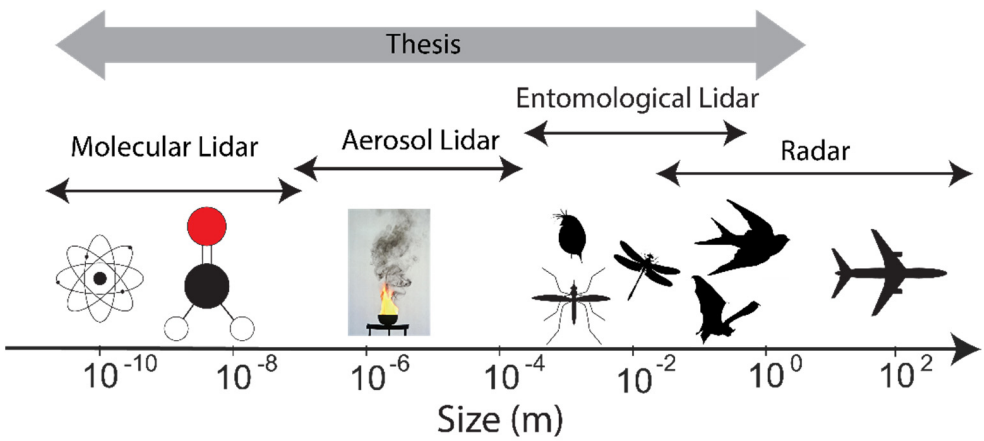

Figure 1.1. Measurement targets and their sizes.The approximate size range at which different Lidar types opperate are also shown.

1.2.1 Aerial fauna monitoring

There are several reasons why efficient monitoring of insect behavior and movement, *in situ*, is important. The reasons may have their basis in ecosystem conservation and sustainability, humanitarian concerns, economical issues, or a combination of several of these.

Insects is a very large group of animals, which has great impact on function and biodiversity in most ecosystems [27]. Insects play the vital role of pollinator, without which many ecosystems would collapse and human food production would break down. Furthermore, insects function as a food source for animals higher up in the food-chain, such as bats and birds, which means that the behavior of insects, directly affects the behavior of the predators. Information about the behavior, movements and distribution of flying insects are thus not only key to understanding insects, but also the ecosystem as a whole.

Some insects are also disease vectors, infecting both humans and animals. For instance, diseases transmitted by mosquitos, such as Malaria, Dengue fever or Zika fever, result in enormous human suffering around the world each year. Malaria alone kills around half a million people annually, mostly people living in poverty and many of them children [28]. The World Health Organization estimates that 219 million cases of Malaria occurred worldwide in 2017, 92% of them on the African continent [28]. The spread of Malaria also has large negative economic impact on whole societies and may in fact be one of the factors halting the economic development in many African countries, though the exact impact is hard to quantify [29,30]. Transmission and spread of these diseases are strongly connected to the distribution and movements of their carriers. Methods which can deliver extensive information about this may help in the implementation and development of efficient preventive methods [31]. This is also the case for monitoring of pest insects, since better knowledge about where and when a certain pest insect is active may lead to a much cheaper and more efficient use and development of pesticides.

Stand-off detection methods can provide continuous and extensive monitoring of flying insects, which is impossible with manual methods, such as collection in sweep-nets or traps. Radar has been used for this purpose for around 50 years [32,33]. Radars are used to carry out long term migratory flight studies and the field have made a great contribution to the understanding of insect and bird migration. Radars can track swarms of insects, and radars purpose-built for the application may also identify the signal from individual larger insects [34]. In general, radars tend to have a blind range of a couple of hundreds of meters, and signals close to the ground are ruined by clutter from the terrain, vegetation and the ground itself. So-called harmonic radars allow detection and tracking of individual insects close to the ground, but the insect then has to be tagged with a transponder [32,33]. The main limitation of the radar technique in entomology is that the selectivity is low. The interaction between the long wavelength of the microwaves and the small structures of an insect results in signals containing very

little information that can be used for classification of specific insects. Lidar, which uses much shorter, optical, wavelengths, can provide information about much smaller structures than Radar, even extracting molecular information. The low divergence of the laser beam used in Lidar also allows it to measure close to the ground.

A conventional atmospheric Lidar can be used to detect insects, but due to the low pulse-repetition rate of the laser and the required temporal averaging, the insect signals are not adequately resolved and most of the information is lost. A group at Montana State University performed some early work using a pulsed Lidar system specifically to detect honey bees [35]. In their following work they used a pulsed Nd:YAG laser with kHz repetition rate to resolve the wingbeats of the bees [36,37] and recently they reported on 3D mapping of insects using this kind of system [38].

Scheimpflug Lidar was first developed at Lund and Stellenbosh Universities as an attempt to demonstrate Lidar beyond the diffraction limit, by utilizing the blinking nature of insect signals [39]. This was inspired by methods used in super-resolution microscopy. The technique was then further developed as a mean to perform range resolved fauna detection with kHz sampling rates. The aim was to move away from heavy and expensive pulsed-laser systems and detectors requiring high voltage, and instead use small CW diode lasers and a line-array camera. The reason for this was to develop a practical and low-cost entomological Lidar instrumentation that would be robust and inexpensive enough for use in developing countries [40], where many of the issues related to flying insects, such as Malaria, are prevalent. The project focused on the aerial fauna monitoring presented in this thesis is a direct continuation of that work. The work has included development of data analysis routines, testing of the system in the field, and working with biologists to tackle biological queries.

1.2.2 Combustion diagnostics

Whether it has been in the form of cooking fires or as the driving mechanism behind car engines and industrial power plants, combustion has been the dominating basis of human energy consumption for many thousands of years. Combustion is the high-temperature reaction between a fuel and an oxidant, during which a large amount of energy is released, e.g. when methane is burnt with oxygen, resulting in CO_2 and water:

$$CH_4 + O_2 \rightarrow CO_2 + H_2O. \tag{1.1}$$

This is an example of global reaction, which only shows the initial reactants and the final, stable, products. In reality, combustion is a very complex process, in which a large number of elementary reactions occurs (ranging from a few hundreds to a few thousands for hydrocarbon combustion) involving many intermediate species, in between the initial and final states (see more in e.g. [41]). To meet the growing concern about pollution and the impact of fossil-fuel combustion on the climate, knowledge

about combustion processes is vital. Optical combustion diagnostics, which is often nonintrusive, is able provide spatially and temporally resolved information about species distributions, concentrations, temperatures and flows [42,43]. This is necessary information both when the efficiency of current combustion concepts is to be improved, as well as when alternative methods or fuels are to be found. Many of the conventional combustion-diagnostic concepts are difficult to apply in large combustion facilities, such as full-scale furnaces, power plants or boilers, due to the limited optical access, the need for spatial resolution, or simply the sheer size of the measurement volume.

A technique that could fill this gap in practical combustion diagnostics is Lidar. As mentioned above, this is an established measurement technique that has been used for decades to retrieve information about atmospheric constituents. It allows *in-situ*, range resolved measurements in the backward direction using only one optical access. Previously, the Lund group has developed a ToF-Lidar system based on picosecond (ps) laser pulses and an ultrafast detector, such as a streak camera, to achieve adequate range resolution. The ps-Lidar system has been demonstrated for several common combustion diagnostic applications, such as thermometry, soot diagnostics and species detection [44–47]. Laser-induced fluorescence (LIF), which is a very important tool in combustion diagnostics, since it is very sensitive and highly species specific, is difficult to utilize in ps-Lidar. The reason for this is that the fluorescence lifetimes will degrade the attained range resolution and adequate range resolution for combustion diagnostics is therefore difficult to achieve with ToF-Lidar [48]. This issue is one of the reasons why the potential of the S-Lidar concept has been investigated for combustion. Since S-Lidar obtains its range resolution through imaging of the laser-induced emission, instead of time-resolved detection, LIF is fully applicable with this method. The S-Lidar concept also enables the use of small and very robust CW diode lasers, which are very practical in an industrial environment.

In this project, the S-Lidar concept, initially used for fauna monitoring in the atmosphere, has been rescaled to construct systems adapted to range resolved measurements over distances of a couple of meters. These systems have primarily been used to demonstrate applications for combustion diagnostics.

Chapter 2

Background physics

2.1 Light matter interaction

The nature of light can be described both as travelling electromagnetic waves, according to Maxwell's equations, and as particles (photons), according to quantum theory. In certain situations, e.g. when dealing with the geometrical optics of imaging systems, an even simpler approach is favorable, i.e. treating light as rays. The different descriptions of light are used depending on the system that is to be characterized and the information desired. All three models, or combinations of them, will be used in this thesis to describe how light interacts with matter. The outcome of a light-matter interaction will be determined both by the properties of the impinging light, such as wavelength and polarization, and by the structure and composition of the matter that the light impinges on. Some of these aspects will be discussed below.

2.1.1 Energy

The probability and outcome of light-matter interaction are highly dependent on the quantum energy of the light, E_q. This quantum energy, is proportional to the frequency, ν, of the electromagnetic wave, which in turn is inversely proportional to the wavelength of the light, λ:

$$E_q = h\nu = \frac{hc}{\lambda}. \tag{2.1}$$

Here, h is Planck's constant and c is the speed of light in vacuum. Both frequency and vacuum wavelength can thus be used to define the energy of light. In this thesis, energy of light will generally be described using wavelength. As seen in Eq. 2.1, higher energy corresponds to shorter wavelength, while lower energies correspond to longer wavelengths.

2.1.2 Polarization

The polarization of a travelling electromagnetic wave is defined as the direction of the wave's transverse electric-field component. The direction of the electric field in unpolarized light is random while the direction is well defined for polarized light.

The polarization of light is generally said to be elliptical. The electric field component rotates with a constant speed in a plane while the wave propagates. When the magnitude of the electric-field component is constant the light is said to be circularly polarized. The tip of the electric-field component will then trace out the shape of a circle in a plane perpendicular to the propagation direction. Linear polarization is the special case when the rotation speed of the electric field-component is zero, i.e. it only oscillated in one direction. A full description of the polarization state of light is given by the experimentally observable Stokes parameters, see [49,50].

In many cases, the polarization of light influences how it will interact with matter, determining what kind of process will take place. Moreover, the polarization state of light often changes after an interaction. Throughout this thesis, linearly polarized light that retains its original linear polarization after interactions, i.e. the polarization of the light is parallel to the original direction, is referred to as co-polarized light, while light that has changed its polarization 90 degrees (perpendicular to the original direction), is called de-polarized light. When linearly polarized light travels through a scattering medium it will lose its linear polarization. The ratio between the co- and depolarized components of the light, called the degree of linear polarization (DoLP), will decrease with increasing path length. When the polarization of the light has become completely random the DoLP is 1/2 [50]. This ratio thus gives information about e.g. the scattering properties of the material through which polarized light has propagated.

2.1.3 Scattering

Light scattering is a process in which light is made to deviate from its original propagation direction by inhomogeneities in its path. A scattering event may be either elastic, where the scattered light has the same wavelength as the incident light, or inelastic, where the wavelength is changed. Figure 2.1 shows a summary of the types of scattering discussed in this thesis. The figure shows a schematic energy level diagram and a corresponding spectrum, displaying the resulting signals in the spectral domain.

The description of elastic light scattering from particles approximated with a sphere may be divided into three main regimes depending on the size of the scattering object compared to the wavelength of the light. When the scattering particles are significantly smaller than the wavelength of the light (radius $<0.03\lambda$ [5]), which often is the case for atoms and molecules in optical spectroscopy, Rayleigh theory [51] is sufficient to describe the scattering. The scattering is thus called Rayleigh scattering. When the scattering particles have approximately the same size as the wavelength of the light, the

more complex Mie theory has to be used to describe the scattering. Scattering from e.g. aerosols in the atmosphere is thus often described by Mie scattering. The often non-spherical particles are then approximated as spheres. Finally, if the scattering objects become much greater than the wavelength, the scattering can, to a large extent, be described by geometric optics, using e.g. the laws of reflection and refraction. Mie scattering theory, which is quite complex, will not be discussed further in this thesis, but the interested reader may find a description relating to atmospheric Lidar in e.g. [5]. There are also more complex computational models describing elastic scattering from non-spherical particles, see e.g. [52].

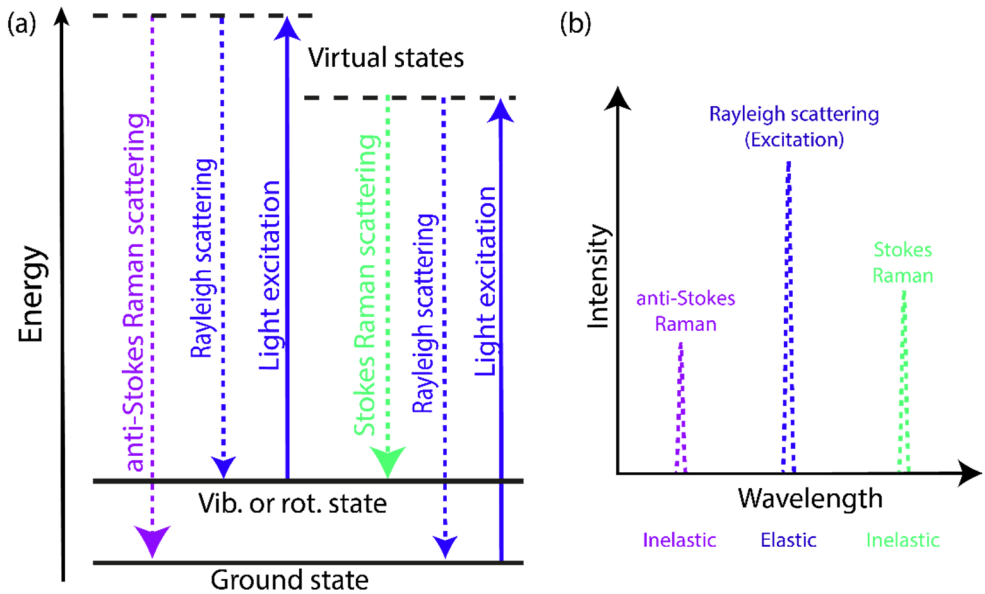

Figure 2.1. a) Schematic energy level diagram displaying the difference between elastic Rayleigh scattering, and inelastic Raman scattering. Panel b) shows the difference in spectral properties for the different types of scattering.

2.1.3.1 Rayleigh scattering

Rayleigh scattering from e.g. molecules may be defined as the emittance of light when the molecules instantaneously fall back into the ground state after being excited into a virtual upper energy state, as shown in Fig. 2.1. This process is classically described as induced dipole scattering. The oscillating electric-field component of an electromagnetic wave will act on the charges of the atoms or molecules in the medium through which the wave is propagating, and cause them to oscillate along its direction and with its frequency. The particles thus become radiating dipoles, sending out light with the same wavelength as the impinging light. The scattering process will result in density fluctuations in the medium, causing the scattered light from the radiating

dipoles to be out of phase. The intensities of Rayleigh scattering from each molecule may therefore be added to attain the total Rayleigh scattering intensity. The Rayleigh signal is thus proportional to the number density, as well as the Rayleigh cross section of the species in question

The differential Rayleigh scattering cross section [3], i.e. scattering cross section, σ_R, per solid angle, Ω, is dependent on the polarization angle of the electric field component of the light, ϕ_{pol} (see Fig. 2.2(a)), the difference between the observation angle and the propagation direction of the incident light in the scattering plane (*z-y* plane), θ_{obs}, the refractive index of the medium, n, the wavelength of the incident light, λ, and the number density of molecules in the medium, N, according to:

$$\frac{d\sigma_R(\theta_{obs},\phi_{pol})}{d\Omega} = \frac{\pi(n^2-1)^2}{N^2\lambda^4}\left(cos^2\,\phi_{pol}\,cos^2\,\theta_{obs} + sin^2\,\phi_{pol}\right). \tag{2.2}$$

Rayleigh scattering is thus heavily dependent on the wavelength, diminishing with a factor $1/\lambda^4$ with increasing λ. Equation 2.2 also shows that the observation direction in relation to the polarization of the incident light is of great importance when detecting Rayleigh scattering; e.g. no light will be scattered along the polarization direction of the incident light. The intensity of Rayleigh backscattering ($\theta_{obs}= 180^0$) is identical to the intensity of Rayleigh forward scattering ($\theta_{obs} = 0$). This holds true both for polarized and unpolarized light. When particles increase in size, resulting in Mie scattering, the forward scattering becomes more and more dominant. See illustration in Fig. 2.2(b).

The proportionality of the Rayleigh scattering intensity to the cross section and number density is utilized in Rayleigh scattering thermometry to extract temperature in a gas. Using the ideal gas law together with the assumption that the pressure, p, and volume, V, are constant, it is easily shown that the intensity of the Rayleigh signal is inversely proportional to the temperature:

$$I \propto \frac{d\sigma_R}{d\Omega}\cdot N \propto \frac{d\sigma_R}{d\Omega}\cdot\frac{1}{T} \tag{2.3}$$

If a reference Rayleigh signal, I_2, is detected in a known environment with a known temperature, T_2, a Rayleigh signal from another environment, I_1, e.g. a flame, may be converted to temperature, T_1:

$$T_1 \propto \frac{I_2}{I_1}\cdot T_2 \cdot \frac{d\sigma_{R1}/d\Omega}{d\sigma_{R2}/d\Omega} \tag{2.4}$$

When identical experimental setups are used to acquire both I_1 and I_2, the proportionality sign in Eq. 2.4 becomes an equal sign, a fact that is used in paper V.

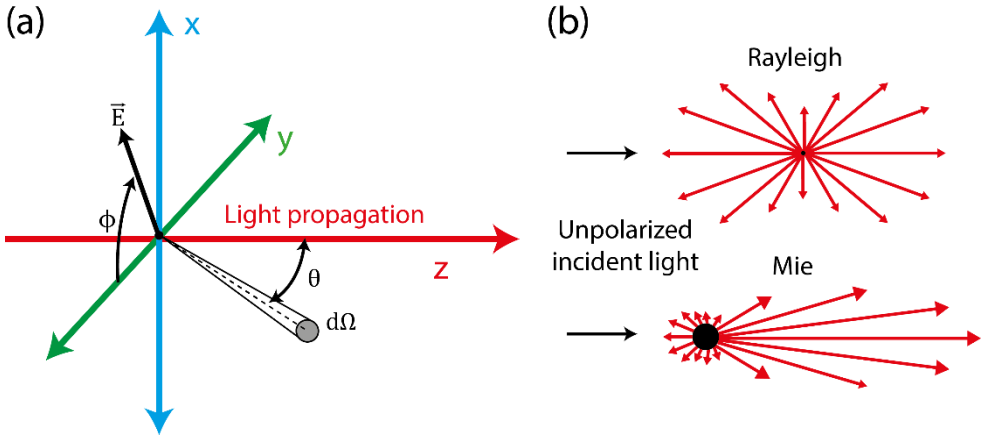

Figure 2.2. (a) The polarization angle, ϕ_{pol}, and observation angle, θ_{obs}, are defined in relation to the propagation direction of light. An induced dipole will oscillate along the electric field component ($\vec{E}$) and emit Rayleigh scattering. Equation 2.2 gives the differential Rayleigh cross section per solid angle $d\Omega$. (b) The scattering distribution of Rayleigh and Mie scattering for unpolarized light. The backscattered and forward scattered intensities are the same in the Rayleigh regime, while forward scattering is dominant for Mie scattering, and becomes more so with increasing particle size.

2.1.3.2 Raman scattering

When molecules are acted on by the oscillating electric field of light propagating through a medium, vibrations and rotations may perturb the oscillation of the dipoles, changing their oscillation frequency somewhat. This will cause a small fraction of the emitted radiation to have another wavelength than the original light. This type of inelastic scattering is called Raman scattering. Raman scattering has two different components called the Stokes and anti-Stokes components. In Stokes Raman scattering, the perturbation results in a loss of energy and the emitted light has a longer wavelength, i.e. lower energy, than the incident light. In the energy diagram in Fig. 2.1, this corresponds to excitation from the ground state to a virtual state, but relaxation occurs into a higher vibrational or rotational energy state. Anti-Stokes Raman scattering takes place when the perturbation of the dipole, by rotations or vibrations, adds energy to the oscillation. The wavelength of the scattered light is then shorter than the incident light. In Fig. 2.1, this corresponds to excitation to a virtual state from the excited rotational or vibrational energy state and relaxation down to the ground state. The anti-Stokes component is often much weaker than the Stokes component since the population of the upper resonant state is often lower than in the ground state. This difference in population is strongly temperature dependent, in accordance with the Boltzmann equation, a fact that is exploited to carry out temperature measurements with Raman based techniques. The shift in energy of the Raman scattered light always

corresponds to the difference between the resonant energy states. Raman scattering is discussed further in e.g. [53].

2.1.4 Absorption

Light absorption may occur when the wavelength of the incident light matches an energy transition in an atom or molecule, i.e. a resonance. The molecule will be excited to a higher energy level and after a certain lifetime the molecule will fall back to the ground state, either through non-radiative relaxation, i.e. collisions, resulting in heat, or by spontaneously emitting light, i.e. fluorescence. Figure 2.3 shows schematic energy diagrams and corresponding spectra describing light absorption. Figure 2.3(a) corresponds to a system in gas phase, while Fig. 2.3(b) shows a system in liquid or solid phase. In solid or liquid phase, the energy states in a molecule are not distinct as they are in gas phase. Interactions between the molecules result in the states overlapping, creating bands. The emitted light after absorption will thus not give narrow spectral peaks, corresponding to transitions between individual energy levels, as in the gas phase case, but rather a continuous spectrum.

2.1.4.1 Fluorescence

Fluorescence has often either the same wavelength as the incident light or it is shifted towards longer wavelength, due to rotational and vibrational relaxation in the excited state. In contrast to e.g. Raman scattering, which is a nearly instantaneous process, not requiring resonance, fluorescence always has a lifetime and it can only occur when the incident light matches a real energy transition in a molecule and is absorbed. The fluorescence lifetime is determined by the decay constant, which in turn is dependent on the intrinsic properties of the molecule, the concentration of molecules, and properties in its environment, such as temperature and pressure.

Due to its resonant nature, fluorescence is a very useful tool for performing species specific diagnostics. Laser induced fluorescence (LIF) techniques are used in many different fields, including combustion diagnostics [42,54], for e.g. species tracing, species concentrations mapping, and temperature measurements. A LIF signal is proportional to the population in the probed state (the state from which excitation occurs), which in turn is governed by the temperature-dependent Boltzmann distribution. By probing two or more energy levels, temperature information can be extracted. This fact is used in paper VI, where the two-line atomic fluorescence (TLAF) technique, see e.g. [55,56], is used to extract temperature in flames remotely. LIF is also used in Paper II to identify chlorophyll, as well as in Paper V.

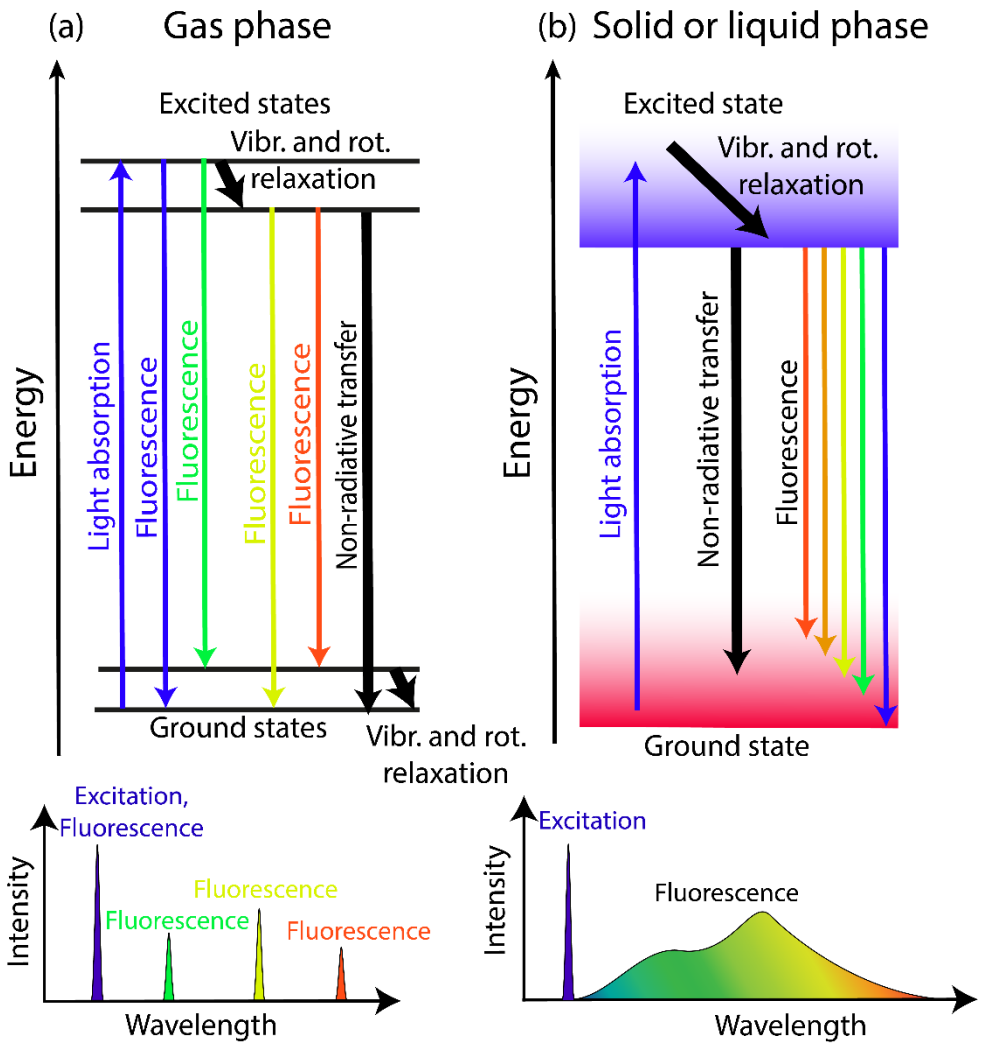

Figure 2.3. Schematic illustration of light absorption in (a) gas phase and (b) liquid or solid phase. Deexcitation after absorption may lead to fluoresence. In gas phase this gives narrow spectral bands while a continous spectrum is attained in liquid or solid phase due to the overlapping energy states.

2.1.5 Light transport

When a light wave travels from one medium to another some of the light will be reflected and some transmitted by the surface i.e. the interface where the refractive index changes. The amount of light that is reflected by or transmitted through the surface is determined by the incident angle, the polarization of the incident light and the refractive index of the two media, according to the Fresnel equations, see e.g. [57]. For light with a polarization parallel to the plane of incidence (p-polarized), there is an incident angle, called the Brewster angle, at which all light is perfectly transmitted through a material.

The law of reflection states that the angle of reflected light in relation to the surface normal will be the same as its incident angle (θ_{in}=θ_{refl} in Fig. 2.4). These kind of mirror-like reflections are called specular reflections. Light that undergo a specular reflection retains its original phase and polarization, i.e. it is co-polarized. It also "remembers" its original propagation direction, according to the law of reflection.

The light that is transmitted through the surface will be refracted, due to the change of refractive index, according to Snell's law, $n_1 \sin\theta_{in} = n_2 \sin\theta_{refr}$. The two main light matter interactions possible for transmitted light have been discussed above, namely scattering and absorption. The probability and the result of these processes will depend on the scattering and absorption coefficients of the medium.

If the light is not absorbed, multiple scattering inside the media will eventually result in some of the light leaving the media through the same interface it entered. This is called a diffuse reflection. In contrast to specular reflections, which are co-polarized and highly directional, diffuse reflections have lost both its directionally and polarization. An ideal diffuse reflection is governed by Lambert's cosine law; see [58], resulting in isotropic luminance. An observer will thus see the same apparent brightness regardless of observation angle.

The extinction of light when it travels through a homogenous medium is due to scattering and absorption. When multiple scattering is negligible the extinction is given by Beer-Lambert's law (see Fig. 2.5):

$$\frac{I(x,\lambda)}{I_0} = exp(-N\sigma_{ext}(\lambda)x)\,, \tag{2.5}$$

I_0 is the incident intensity, N is the number density, σ_{ext} is the extinction cross section and I is the intensity after the light has travelled a distance x, in the medium. For measurements in gas phase, scattering may be ignored and the extinction cross section may be set to the absorption cross section.

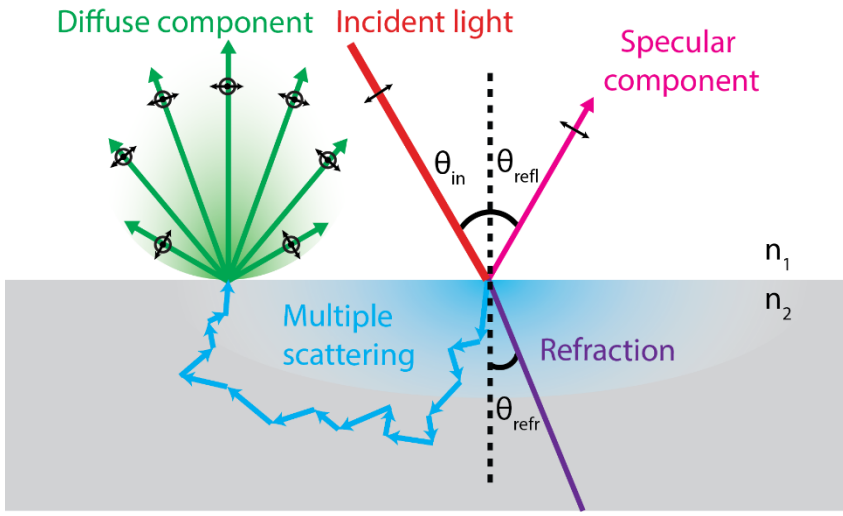

Figure 2.4. Interactions when light travels through an interface between two media. The light is reflected by or transmitted through the surface. The direct reflection at the surface gives a specular component while multiple scattering in the material results in diffuse reflection. Light transmitted through media will be refracted due to the change in refractive index.

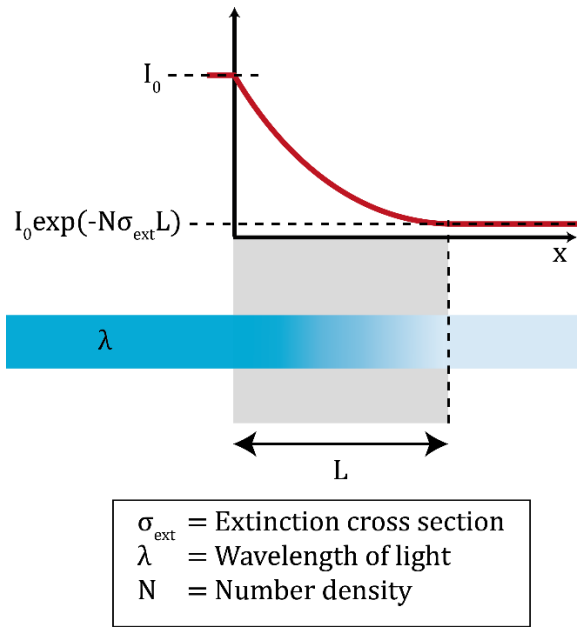

Figure 2.5. An illustration of Beer Lambert's Law. The intensity of light travelling in a material decreases exponentially with increasing distance.

2.2 Signals from insects

Information about insect properties such as size, velocity and wingbeat frequency can be extracted remotely from light scattering. These properties span a parameter space with a certain dimensionality, and a higher dimensionality increases the likelihood of successful classification of different species, sexes and age groups, see [59]. To be able to extract these kind of properties, the signals from insects have to be interpreted correctly. Knowledge about its physical and optical properties is then needed. In this section, the properties of a typical backscattering signal from an insect in flight will be described. In Fig. 2.6(a), the flying insect is exemplified with a mosquito. The signal components originating from different parts of the insect's anatomy are summarized in the table in Fig. 2.6(b), and examples of the components in the time domain, the temporal frequency domain and the spectral domain are shown in Fig 2.6(c)-(d), respectively. The table contains information about the coherency (diffuse or specular), polarization (co- or de-polarized), and temporal properties (modulated or continuous), of both the signal and the incident light. It also describes some of the frequency and spectral features, and their origin. The incident light in this example is coherent linearly polarized laser light from a CW laser beam with a wavelength, λ. This is a good representation of the light used in the ecological Lidar applications in this work. The data shown in Fig. 2.6(d) was collected with a hyperspectral camera using a white, non-collimated light source. It illustrates what happens to the signal if λ is changed.

2.2.1 Temporal and frequency properties

The backscattering signal from a flying insect consists of a non-oscillatory, DC contribution from the insect body during the transit time through the probe volume (Δt), and an oscillatory contribution resulting from its wingbeat cycle. The body and wing contributions can, in turn, be divided into a diffuse and a specular component [21,39]. The oscillating, diffuse component from the wings (blue component in Fig. 2.6) is obtained from their matte parts, e.g. veins and scales. When an insect is beating its wings, it appears alternately large and small in the FoV. Consequently, the projected cross section area which backscatters light changes and the detected signal is therefore modulated, see Fig. 2.6(c). This modulation is directly related to the wingbeat cycle and the fundamental wingbeat frequency, f_0. This results in a power spectrum showing a strong f_0 components and some higher harmonics, as seen in e.g. Fig. 2.6(d). The fundamental wingbeat frequency of atmospheric insects may vary between 10-1000 Hz [60].

Light impinging on the glossy parts of the wing membrane will result in specular reflection (green component in Fig. 2.6). This only occurs at certain times during the wingbeat cycle since the surface normal of the membrane must coincides with the

propagation direction of the laser light. These specular reflections show up as short but high peaks on the signal in the time domain, as seen in Fig 2.6(c), or as strong harmonics in the frequency domain; see Fig 2.6(d). The waveform of wingbeats may contain a large amount of higher harmonics due to specular reflexes. This means that a high sampling rate is required to resolve the detailed waveform from flying insects.

The backscattering from the matte parts of the body, such as scales and fur, results in a diffuse, non-oscillatory component; shown by the pink component in Fig. 2.6. The signal in the time domain reflects the shape of the beam profile along the flight trajectory of the insect, here referred to as the envelop, and a high DC component in the frequency domain. Glossy parts of the body (red component in Fig. 2.6) will give rise to a specular signal component, with a similar shape in the time and frequency domains as the diffuse body components, but with different signal strength.

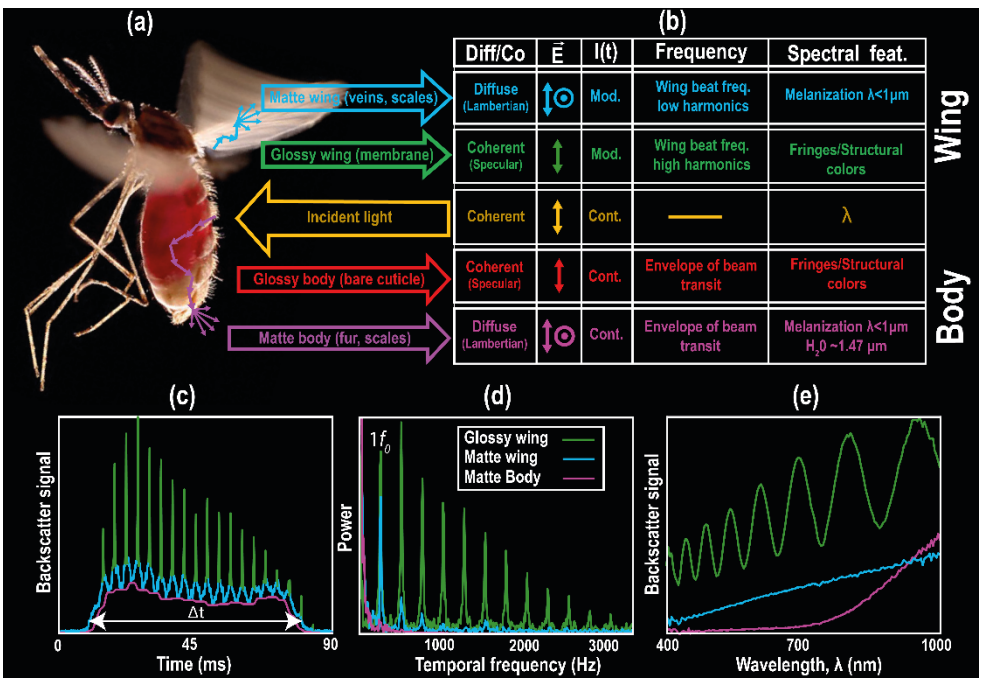

Figure 2.6. Summary of a typcial insect signal. In (a) a mosquito (*Anopheles stephensi*) is shown in flight (Photo credit to Hugh Sturrock). (b) Table summarizing the typical properties of the different signal components when the incident light is a linearly polarized CW laser beam with wavelength λ. The signal components from the glossy and matte parts of the wing, and the matte parts of the body are shown in the time domain in (c), in the frequency domain in (d) and in the spectral domain in (e). The specular body component is not shown in (c)-(e) since it is similar to the diffuse body component in both the time and frequency domains. The signals shown in (c) and (d) are from a flying fruit fly (*Drosophila melangaster*) and the spectra in (e) is from a type of snipe fly. The mosquito in (a) is blood feed, which would affect the diffuse body components through absorption (not discussed here).

2.2.2 Spectral properties

The spectral properties of insect reflections, are a result of their pigmentation, physical surface structures, or a combination of both, as well as the type of illumination. How such a reflection is spectrally perceived by an animal with a certain type of spectral receptors and neural processing, is described by the term color [61]. Figure 2.6(e) displays the spectral properties of the different signal components, showing generally increasing signal strength with increasing wavelength. The coherent component also shows very distinct spectral fringes. To better discuss the spectral properties, several push-broom hyperspectral images of insects, exhibiting different colors, are presented in Fig. 2.7. Spectra from different parts of the insects are displayed to exemplify the diverse spectral features.

When white light impinges on an insect, the physical structure of the surface may cause certain wavelengths to be reflected, e.g. through interference effects. This is referred to as structural colors [61,62]. A type of structural colors, which are straight forward to explain, is the colors created through interference in a transparent wing membrane. Most insect wings consist of the tough, translucent material, chitin, pressed into a membrane. The thickness can vary widely between species (~0.5 µm-1 mm) and within the same wing [63]. If the membrane is approximated as a thin-film reflector or a Fabry Pérot etalon (see Fig. 2.8), the impinging light wave will be partially reflected at the upper boundary layer and partially reflected at the lower boundary. The subsequent difference in optical path length of the light will result in optical interference. A limited set of wavelengths will be in phase and thus reinforced, and the coherent backscatter spectrum will contain interference fringes (see spectra in Fig. 2.6(e), Fig 2.7(a), Fig 2.8, Fig 2.9). The resulting structural color patterns can be observed on the wings in the image shown in Fig 2.7 and Fig. 2.9, but most of the specular reflections appear white because of saturation. These kind of iridescent (changing with observation angle) colors are also seen on the surface of soap bubbles or from oil on top of water. The colors pattern observed is directly related to the spectral separation between two adjacent fringes in the coherent backscatter spectrum, $\Delta\lambda$. This is, in turn, directly dependent on the thickness of the thin membrane, L, the incidence angle of the light, θ_{in}, the central wavelength of the nearest transmission peak, λ, and the refractive index, n:

$$\Delta\lambda \approx \frac{\lambda^2}{2nL\,cos(\theta_{in})}. \tag{2.6}$$

According to Eq. 2.6, the width of the fringes will increase with wavelength and a thicker membrane will give rise to narrower fringes. This can be seen in the two examples shown in Fig. 2.7(a), where fringes from a thick (yellow curve) and a thin (pink curve) part of the membrane are shown. The thickness of the wing membrane may thus be determined from specular reflections, and this information could in turn

be utilized in identification of insects and insect behavior since it has been found to be species specific [64] and may have evolved for sexual selection [65].

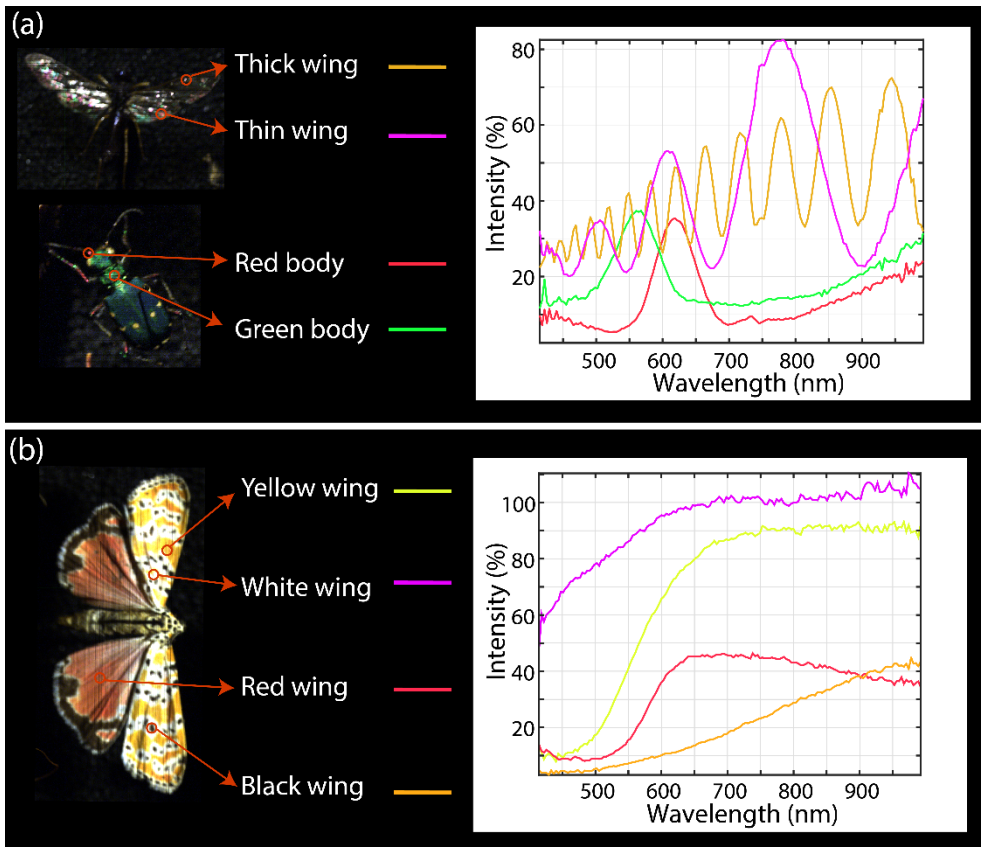

Figure 2.7. Examples of insect colors in the visible and near infrared aquired with a push broom hyperspectral camera. Panel (a) shows different examples of sharp spectral features from a type of fly and a green Tiger beetle. Specular reflection from the transparant wings give rise to interference fringes. The spectral width of the fringes is reciprocally related to the thickness of the memebrane. A thick membrane (yellow curve) gives narrow fringes while a thin membrane (pink curve) gives wide fringes. The plot also shows sharp, green and red spectral features from the body of the beetle. Panel (b) displays signals from a colorful butterfly, showing broader spectral features. The white color (pink curve), resulting from non-periodic scattering structures, lies, as excpected, around 100% reflection in the whole wavelength interval, while the black, melanized feature (orange curve) is very low but increase somewhat with wavelength. The red/orange and the yellow spot both show typical absorption features resulting from pigment absorption at short wavelengths.

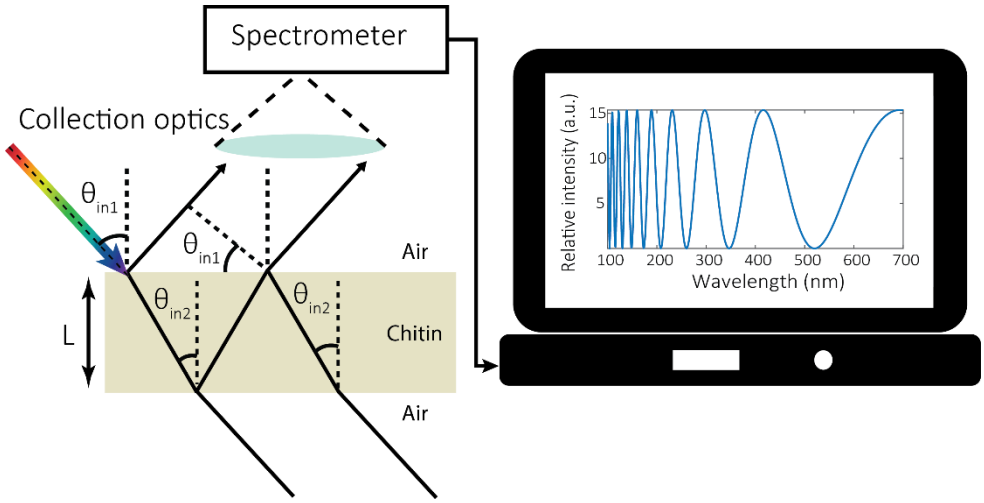

Figure 2.8. The principle of thin film interference in a thin membrane with refractive index, *n*, surrounded by air. Light is coherently reflected in the first and second interface of a thin layer causing constructive intereference for some wavelengths and destructive interference for others. The result is a spectrum with fringes which increase in width with wavelength, see Eq. 2.6.

There are many more complicated quasi-ordered biological matrices giving rise to structural colors. For example, the scales of the insect might consist of near-parallel structures, separated by air spaces, which form a series of reflecting surfaces, resulting in interference. Structures may also arise from differences in refractive index inside the cuticle of the insect. Some nanostructures are more complex creating e.g. helicoidal structures, that not only result in structural colors but also alters the polarization of the light into circular polarization [61–63]. The reflections from the colorful beetle in Fig 2.7(a) and the bright blue butterfly in Fig. 2.10(a), are examples of structural colors that are not a result of simple thin film interference. They display sharp spectral features at the specific wavelength that are reinforced during the specular reflection in the nanostructure in the surface.

The spectral content of a signal is affected by absorption by the bulk material of the body, often. chitin, or pigments therein. When pigments absorb certain wavelengths and give rise to a selection in reflected wavelengths, it is referred to as pigmentary colors [61]. These pigments may be produced by the insects themselves or come from the food they eat. Two important types of pigments are melanins and carotenoids. Carotenoids absorb in the lower parts of the visible spectrum, resulting in red, yellow or orange reflected colors. Melanin absorbs strongly in most of the visible wavelength range, and thus gives rise to black or dark colors in human vision. The effect of melanization is thus highly relevant when the wavelength is chosen for optical measurements. In Fig. 2.9 two hyperspectral images are shown, one at visible (VIS) and near infrared (NIR) wavelengths and one at short-wave infrared (SWIR) wavelengths.

Two spectra from the body, one from a dark melanized part and one from a yellow part are shown. One spectrum from a specular reflection from the wing is also displayed. In the visible, the dark melanized part of the insect has very low reflectivity, while the reflectivity increases substantially in the SWIR, making the whole insect appear bright. Signals at longer wavelengths thus give higher total signals, but also a more uniform signal level from different parts of the insect, facilitating e.g. optical size determination.

The fact that the degree of melanization is not the same for different groups of insect may complicate analysis of signals from an unknown insect. With this being said it, the degree of melanization could also be used for classification of insect due to this difference. By analyzing the ratio between signals at two different wavelengths, e.g. one in SWIR and one in near infrared (NIR), a measure of the melanization can be estimated and utilized for identification, see more in [66].

The spectral signal from an insect is usually not only structural colors or only pigmentary ones, but a combination of both. Nano-structures that reflect light are e.g. often combined with a layer of broad-band absorbing melanin, which absorbs the transmitted light. It is also possible for the structures that cause interference phenomena to be made up of pigments such as melanin, typically in the shape of granules [61]. The blue butterfly in Fig. 2.10(a) is a good example of how the colors of an insect is a combination of structural and pigmentary colors. In 2.10(b), a spectrum from the blue wing is seen. It shows a sharp spectral feature at blue wavelengths but also an increase in wavelength across the visible range propably due to pigment absorption at short wavelengths. Two images of the blue butterfly are shown in Fig. 2.10(c) and (d). The first image shows reflection of white light, i.e. the white light source is placed on the same side of the butterfly as the camera. In this configuration the butterfly's bright blue structural colors are seen. In the second image (d), light transmitted through the wings is detcted by the camera, i.e. the light source is now placed behind the butterfly. Now, no blue color is seen, only the black, yellow and brown colors caused by absorption when the light passes through the wings. In Fig. 2.10(e) and (f), the reflected light of the butterfly is shown, but here a linear polarization filter is placed in front of the camera and the light source. Next to the butterfly, the green beetle, also seen in Fig. 2.7, is shown. When the polarization direction of the light matches the direction of the filter in front of the camera, specularly reflected, co-polarized light is detected and the bright blue and green colors of the insects are visible. When the polarization directions do not match, the co-polarized light is removed, and much of the structural color disappears and the darker colors due to absorption are seen. The green beetle becomes almost black except for the yellow color which most likely is a result of pigment absorption. Another example, using a moth, is also shown. When the co-polarized light is detected the moth has a green irridescent color but when only the de-polarized light is detected, the moth's dull brown pigementary colors can be seen.

2.2.3 Other factors

The backscattering signals from insects are dependent on the optical and physical properties of the specific insect species, such as wingbeat frequency and body melanization, but also on the behavior and surroundings of the individual insect. Environmental factors, such as temperature and humidity, will e.g. affect the physical movements of a flying insect, resulting in a change in the oscillating part of the signal [60]. The optical properties of insects from the same species may differ depending on for instance age and sex, see e.g. [67,68]. A young individual may have glossier wings than an old one. Another factor that might affect the optical properties is the feeding status of the insect. For instance, a female mosquito that just had a blood meal may have different optical properties than one that did not, since the blood-filled body may absorb some of the light.

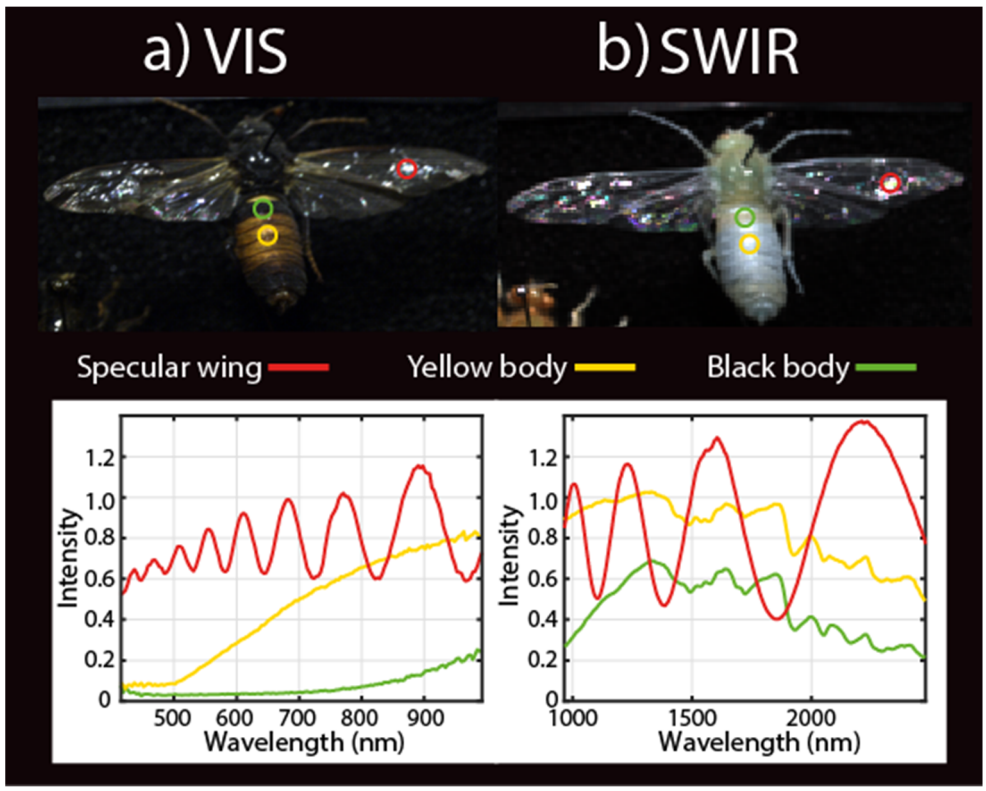

Figure 2.9. (a) A hyperspectral image of a type of snipe fly in the visible wavelength range. (b) A false color hyperspectral image of the same insect in the SWIR wavelength range. The spectrum from a black and yellow spot, as well as for a specular wing reflection is shown in both wavelength ranges.

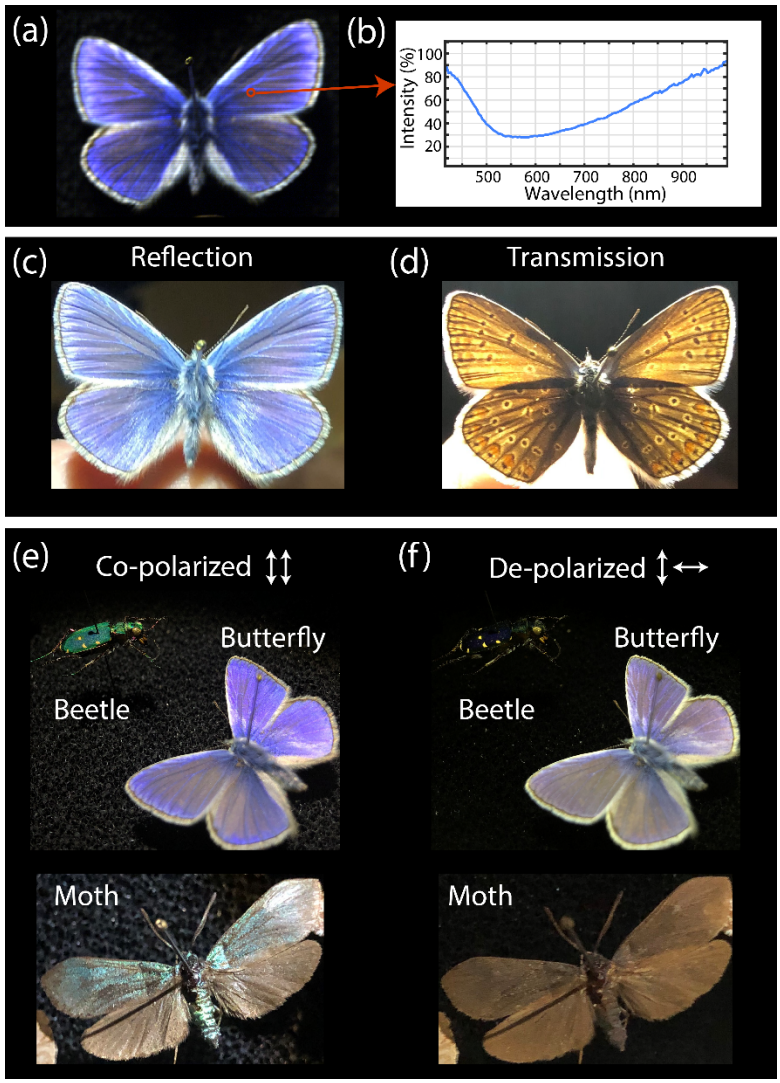

Figure 2.10. (a) A hyperspectral image of a bright blue butterfly. (b)The reflection spectrum from the butterfly has a sharp peak at blue wavelength due to structures in the surface of its wings. (c) Reflection and (d) transmission images of the same blue butterfly. In reflection mode, the butterfly looks blue, due to interference phenomena in the structure of its wings. When the transmission through the wings are detected, the blue structrural color is not seen, but only colors caused by pigments in the wings and the removal of the blue light due to reflection away from the camera. Linear polarization filters were placed in front of the white light source and the camera to only look at reflection of co-polarized (e) and de-polarize light (f). The light reflected off the blue butterfly, the green beetle, and a moth are shown. Since the blue (butterfly), green (beetle) and irridescent (moth) structural colors are a result of light that has kept its polarization, they are clearly visible for the co-polarized case but they diminish or disappear completely for the de-polarized case. De-polarized reflection gives diffuse colors due to absorption in the wings and body.

2.3 Signals from flames

2.3.1 Flames

Combustion commonly occurs as flames. Fundamentally, a flame consists of a flame front, or reaction zone, that propagates from the already combusted product gas towards the unburnt reactant gas. The propagation occurs through diffusion of species and heat. When the speed at which new reactants are added equals the velocity of the flame front (burning velocity) a stable flame is established, e.g. a candle.

The properties of a flame are determined by the type of fuel and oxidizer used, how and when they are mixed and the properties of their flows. In a diffusion flame, such as a candle, the combustion occurs where the oxidizer and fuel meet, while the fuel and oxidizer (typically air) is mixed before combustion in a premixed flame. The flow in a flame may be either laminar or turbulent. A flame with a turbulent flow has a higher burning velocity and less static flame structures, than the same flame with a laminar flow. The focus here will be on premixed, laminar flames since most of the flames used in this work have been of this type. The main advantage of a premixed flame is that the mixing ratio of fuel and oxidizer, or stoichiometry, may be well defined, which means that the composition of the resulting products is well known. A typical conical premixed hydrocarbon flame on a Bunsen type burner is shown in Fig. 2.11(a). The blue color of the flame is a result of chemiluminescence from the reacting species in the flame, and this constitutes the major background emission for this type of flame. More information about this background is found in the top row of the table in Fig 2.11(b) and in the plots in Fig. 2.11(c)-(e).

The inner part of the cone contains the cold, unburnt reactants gas (fuel and air), flowing out of the burner nozzle. The thin blue cone seen in the image is the hot, reaction zone where the combustion occurs. In between these zones is a thin zone where the reactants get heated before they are combusted, called the pre-heat zone. The combustion products are found on the outside of the flame front, in the so-called product zone. The temperature of the products decreases when they move away from the reaction zone. If the mixing ratio of fuel and oxidizer is larger than 1, i.e. all of the fuel cannot be consumed, it is possible to get a secondary flame front where the combustion products meet the oxygen in the surrounding air.

2.3.2 Optical flame diagnostics

Light passing through a flame interacts with the present gaseous species. The optical signal from each flame zone will be different since the temperature and the composition of species are not the same. The total backscattering signal is thus made up of several different components. The nature of these components will undoubtedly depend on

the type of flame, the properties of the incident light, and how the detection is carried out. Short laser pulses in combination with a time-gated camera is often used in combustion diagnostics as a way to suppress background signal and obtain high temporal resolution. The camera only detects signal during the very short, high intensity laser pulse, which means that the contribution from the continuous flame emission becomes virtually negligible. Figure 2.11 describes the backscattering signal from a laminar, premixed methane/air flame when a pulsed laser beam, with a wavelength of 355 nm, is transmitted through it. This example is meant to demonstrate three common signals used in laser-based combustion diagnostics. The components induced by the laser are described in the three last rows in the table in Fig. 2.11(b) and they are plotted in the temporal, spatial and spectral domains, in Fig 2.11(c)-(e), respectively.

The first signal is elastic Rayleigh scattering, which is obtained from all flame zones. The signal in the time domain will be determined by the duration of the laser pulse. As seen in Eq. 2.4, the signal strength will reflect the temperature and the Rayleigh cross section of the present species in each flame zone. The signal is thus high in the cold reactant zone but decreases rapidly in the high temperature reaction zone and product zone, as seen in Fig. 2.11(d).

The second type of signal is fluorescence. Due to its resonant nature, fluorescence can be used to identify the positions of specific species in the flame as well as their concentration, temperature, and lifetime. In the example in Fig. 2.11, where a laser at wavelength 355 nm is used, fluorescence from formaldehyde (CH_2O) is attained giving a spectrum containing many peaks in the approximate range 390-450 nm. Formaldehyde is mostly present in the pre-heat zone, with a rapidly decreasing concentration in the reaction zone. If a laser at e.g. 281 nm were to be used also, fluorescence from OH would be detected. The OH concentration is high in the reaction zone and the product zone, resulting in a high fluorescence signal there. The signal then gradually decreases in the product zone. Simultaneously acquired formaldehyde and OH fluorescence signals can, among other things, be used to identify the position of the reaction zone [69,70]. Fluorescence from the radical CH is also often used for this purpose [71]. In contrast to the scattering signal, which is instantaneous, the fluorescence signal has a lifetime resulting in the decay curve seen in Fig. 2.11(c).

The final kind of signal is Raman scattering, which is utilized in combustion diagnostics for major species identification and for temperature measurements. Just like the Rayleigh scattering signal, the Raman signal from N_2, CH_4 and O_2 is instantaneous, and it will be high in the cold reactants and low in the high temperature zones. In the example shown here, a Raman signal is obtained from the cold unburnt gas, e.g. N_2, O_2, resulting in spectral peaks below 400 nm.

Certain fuels and/or high stoichiometry in flames result in the formation of large carbon-based species, such as soot. In the high temperature environment in the flame, soot emits Planck radiation, e.g. the yellow emission of a candle flame, increasing the

natural flame emission. Soot may also result in high laser-based signals, either through elastic scattering, or laser-induced incandescence which is emitted from soot particles that have been heated through absorption of laser light. More in depth information may be found in [72].

If a CW laser beam is utilized for diagnostics in a stable, laminar flame, instead of a pulsed laser, the signals will be continuous in the time domain. Removal of the background can then be done using a look-in method where the beam is modulated on and off in synchronization with the exposures of the detector (see more in Chap. 6-7).

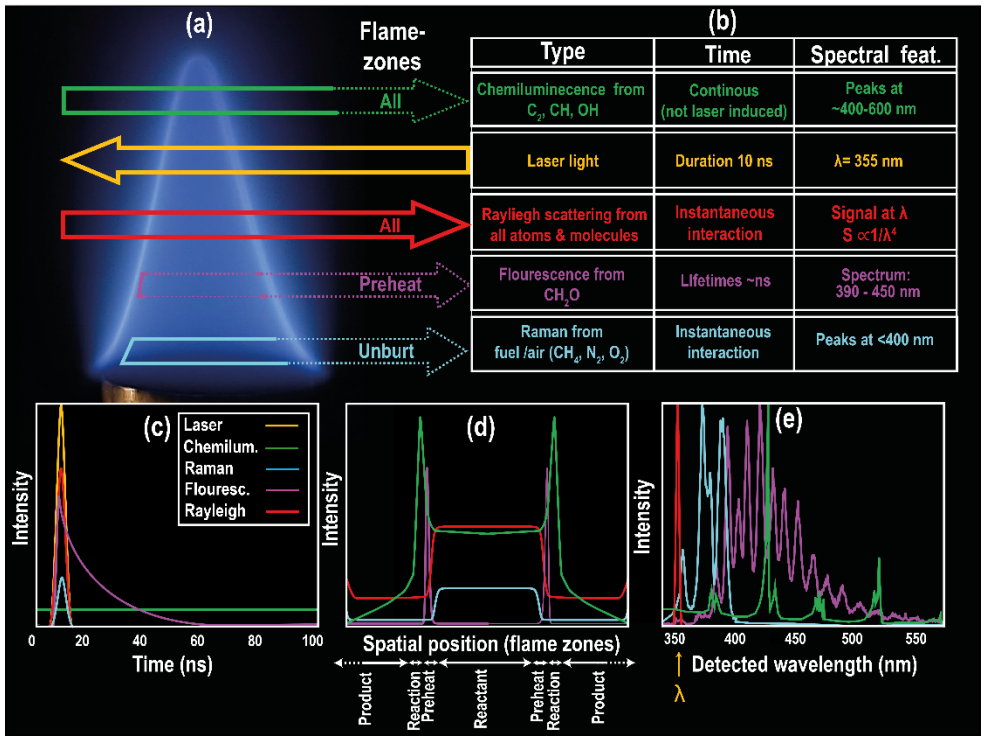

Figure 2.11. A summary of typcial optical signals from a premixed, laminar hydrocarbon flame. (a) A picture of a conical bunsen flame. A 10 ns laser pulse with a wavelength of 355 nm is transmitted through the flame (yellow arrow) resuling in several different signal components. Arrows mark from which flame zones each signal components originates. (b) A table summarizing the properties of the signals. The green signal is the flame emission or chemiluminescence and it is not a result of the impinging laser. Instead it is due to the chemical reaction taking place in the flame. The signal resulting from the impinging laser light are Rayleigh scattering (red), fluorescence (pink) and Raman scattering (blue). Descriptive plots of the signal components are shown in the time domain in (c), the spatial domain in (d), and in the spectral domain in (e). The curves in (d) show the signal from the same horizontal cross section in the burner. Since the width of the flame zones change with height in the Bunsen flame, the spatial scale is defined using the position of the flame zones and the units are thus arbitrary.

Chapter 3

Scheimpflug-Lidar

In this chapter, the theoretical background of S-Lidar is presented. The trigonometrical rules, on which S-Lidar is based, are described and the equations governing the attained range and range resolution of a S-Lidar system are presented

3.1 Scheimpflug and hinge rules

The Scheimpflug principle is an optical principle that defines how the focal plane of, e.g., a camera can be shifted by titling the lens in relation to the detector plane and thereby achieve a large focal depth or depth of field. Jules Carpentier first described this principle in his British patent in 1901 [73], and Theodor Scheimpflug, after whom the principle is named, later developed the concept for use in aerial photography. In his patent from 1904 [74,75], Scheimpflug introduced further trigonometrical constraints which ensures a unique solution to how a lens should be titled when focusing on a plane that is not parallel to the image plane. This constraint is referred to as the hinge rule in this work.

The concepts of the Scheimpflug and hinge rules are illustrated in Fig. 3.1 using an image of the author's dog moving along a garden path towards the camera. Photoshop has been used to illustrate what the image would look like if it was taken with a conventional camera, a pinhole camera, and a camera with a Scheimpflug objective. The effects are exaggerated to clarify the principles. Below each image, there is a schematic representation of the optical configuration, the resulting focal volume (pink area), and the movement of the dog during the time the image was taken. Figure 3.1(a) illustrates the case of a conventional camera, i.e., the front and back focal planes are parallel to the detector and lens planes, and it is strictly the volume in between these two focal planes that is in focus. Consequently, only a small part of the garden path leading away from the camera is in focus. The exposure time can be short, since the aperture on the camera is large, and the part of the dog that is inside the focal volume

is therefore not blurred due to his movement. One way to achieve a larger focal depth with the camera is to use a smaller aperture. If a pinhole is employed, the whole focal volume from the camera to infinity is in focus. This infinite focal depth is achieved at the expense of very low light collection efficiency and long exposure times are thus required, making the system subject to motion blur. This is illustrated in Fig. 3.1(b), where focus has been attained along the whole garden path, but the dog has been blurred due to his movement towards the camera. If a large aperture is employed instead and the lens is tilted in relation to the detector, according to the Scheimpflug principle and hinge rule, the plane of sharpest focus can coincide with the garden path. A large focal depth is thus obtained without reducing the efficiency of the light collection. This is illustrated in Fig. 3.1(c) where focus has been achieved along the whole garden path, and the moving dog does not suffer from motion blur. When the lens is tilted, the focal volume becomes a wedge with the plane of sharpest focus in the center. The width of the wedge is determined by the f-number, just like the depth of field of a conventional camera. Features protruding from this wedge, such as the tree tops and bushes in the background, will be out of focus. Due to the tilt of the lens the magnification decreases with increasing distance from the camera, resulting in the stretched shape of the image in Fig. 3.1(c).

For focus to be achieved along a specific object plane with a Scheimpflug setup, the collection lens and detector have to be aligned in such a way that their planes intersect the object plane along the same line. This intersection is called the Scheimpflug intersection. When the tilt of the lens in such a setup is changed, the position of the Scheimpflug intersection will move along the image plane, changing the position and tilt of the in-focus wedge, as seen in Fig. 3.2(a). However, the Scheimpflug rule by itself does not ensure focus along one specific plane, since the image plane and the lens plane together can be rotated around the Scheimpflug intersection, as shown in Fig. 3.2(b). The position of the object plane is further constrained by the hinge rule, which states that the front focal plane and the plane parallel with the detector that intersects the center of the lens must intersect the object plane. This line is called the hinge intersection. The reason for this name is that the plane of focus will *hinge* around the hinge intersection when the focus of the camera is changed, i.e. when the distance between the detector and the lens planes is shifted; see Fig 3.2(c).

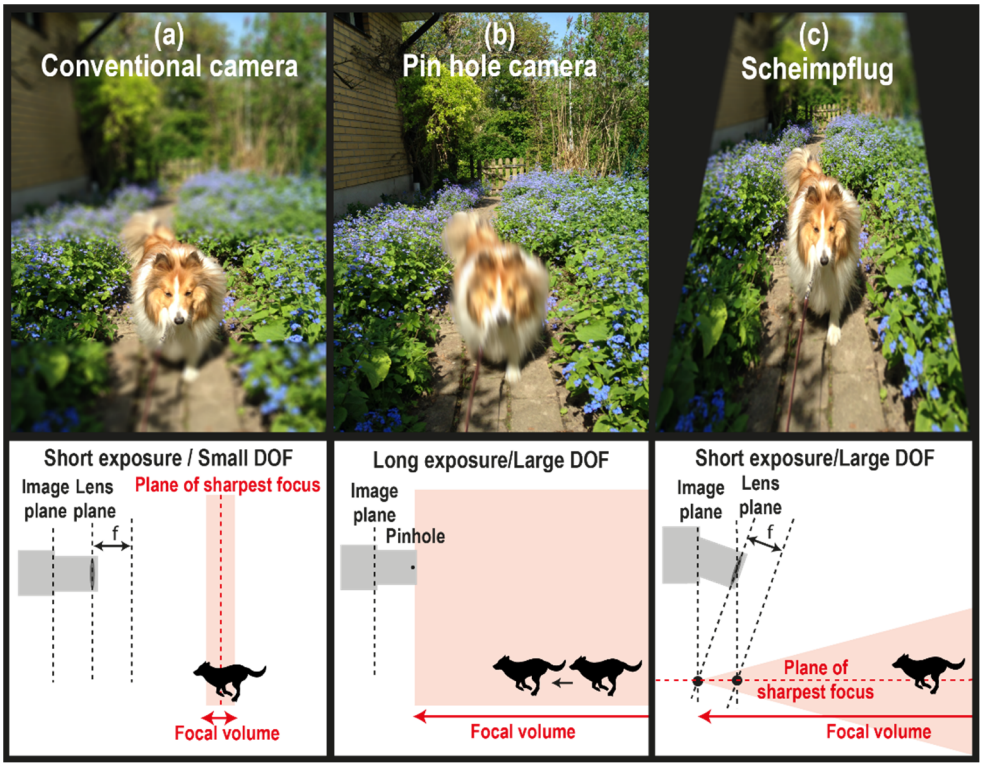

Figure 3.1. An illustration of the Schiempflug principle using three photoshoped versions of the same image of the author's dog running along a garden path towards the camera. A schematic figure describing each case is seen below the images. The image in panel (a) represents the case of a conventional camera where the focal depth is limited. Panel (b) shows the same image taken with a very small aperture. A large focal depth has been achieved but the long exposure time required for sufficient light collection results in motion blur of the moving dog. The image in panel (c) represents the case where a Scheimpflug configuration is used. The lens is titled in relation to the detector plane and the plane of focus stretches away from the camera. A large focal depth is achieved while still using a large aperture, and a short exposure time may be used. The whole garden path can be in focus and the moving dog is not blurred.

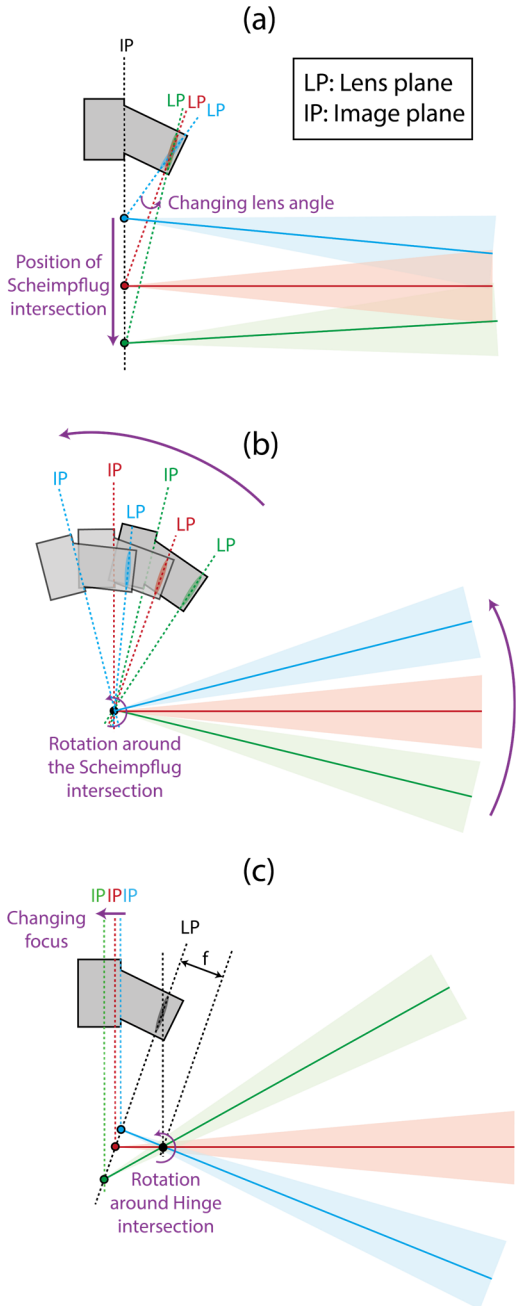

Figure 3.2. (a) The change in position of the Scheimpflug intersection when the tilt of the lens is altered. (b) The possible rotation of the whole system around the Scheimpflug intersection if the hinge rule does not constrain the system. (c) The rotation, or hinging, of the object plane around the hinge intersection when the focus of the system is changed.

3.2 Equations of S-Lidar

In S-Lidar, range resolution is attained by placing the transmitted laser beam along the in-focus object plane of the S-Lidar system. The backscattering from the beam can then be sharply imaged onto a detector placed along the image plane. The observed range (z_{pix}) of a pixel with pixel number, m, and position (p_{pix}) on the detector, is given by:

$$z_{pix} = D \cdot \frac{b + p_{pix}[sin(\alpha) - cos(\alpha) \cdot cot(\phi)]}{b \cdot cot(\phi) + p_{pix}[sin(\alpha) \cdot cot(\phi) + cos(\alpha)]} \tag{3.1}$$

$$D = \frac{b}{tan(\alpha)} * sin(\phi) \tag{3.2}$$

$$\phi = arctan\left(\frac{f_{rec}\, tan(\alpha)}{b - f_{rec}}\right) \tag{3.3}$$

$$p_{pix} = ml_{pix} - \frac{l_{det}}{2}. \tag{3.4}$$

The variables of Eq. 3.1-3.4 are defined in Table 3.1 and Fig. 3.3. The equations were derived by using the trigonometrical constraints given by the Scheimpflug and Hinge intersections (see Appendix A for the derivation). Equation 3.1 is the same equation as presented in paper V, but the variables are arranged in a different way to facilitate the calculation of the derivative further on.

Table 3.1. Variables used in the range and resolution equations for S-Lidar (Eq 3.1-3.9).

Variable	Definition
D	Perpendicular distance between the laser beam and the center of the lens (baseline)
z_{pix}	Range of pixel at position p_{pix}
dz_{pix}	Range resolution of pixel at position p_{pix}
p_{pix}	Pixel position with pixel number m
l_{det}	Length of detector
l_{pix}	Pixel width or pitch
ϕ	Angle between the lens plane and the laser beam plane
b	Distance between the center of the receiving lens and the center of the detector
α	Angle between the lens plane and the detector plane (detector tilt)
f_{rec}	Focal length of receiver
M	Pixel number
dp_{pix}	Change in pixel position (Equal to l_{pix})
X_{pix}	Factor resulting from the change in pixel position

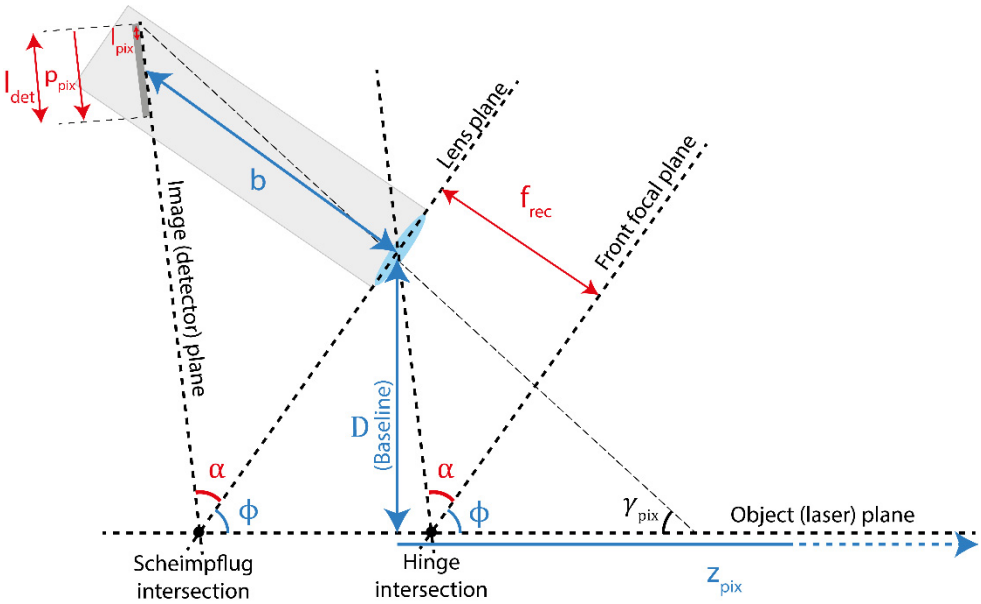

Figure 3.3. A schematic figure of a S-Lidar setup. All the necessary angles and distances needed for the calculation of range and resolution can be seen in the figure. The relevant planes are marked with dotted lines, and the distances are marked with arrows. The distances and angles given for a system (of specific design) are marked in red while the unknown properties are marked with blue. The Scheimpflug and hinge intersection are shown in the lower part of the figure. The distance D (also referred to as baseline) defines the perpendicular distance between the laser beam and the center of the lens. The sampling angle, γ_{pix}, i.e. the angle between the laser plane and the pixel footprint, is also marked in the figure.

For a designed S-Lidar system, there are two unknown variables in Eq. 3.1, namely z_{pix} and b. The distance b can be obtained by using the signal from a target at known distance, z_{ref}, which ends up in a pixel with pixel number m_{ref}. When b is known, z_{pix} may be calculated for all m. For a large system ($f_{rec} >> l_{det}$) which is focused on optical infinity, the range may be approximated by:

$$z_{pix} = D \cdot \frac{f_{rec} + p_{pix} sin(\alpha)}{p_{pix}\, cos(\alpha)}, \tag{3.5}$$

where:

$$p_{pix} = l_{det} - m l_{pix} \tag{3.6}$$

Equations 3.1-3.4 show that the theoretical range resolution of S-Lidar is constrained by the angles at which the pixels are observing the laser beam (govern by the Scheimpflug/hinge conditions) and by the width of the pixels. Due to the nature of the

triangulation used to obtain range information, i.e. an angle represents a specific range, the range scale of S-Lidar is non-linear. The pixels monitoring far ranges observe a more extended volume than the pixels monitoring near ranges. To illustrate the non-linearity of a S-Lidar system, an object, in this case a flame, was translated with constant speed towards the system. Figure 3.4 shows a time-range maps containing the fluorescence signal from the flame. In Fig. 3.4(a), where the non-range calibrated data is displayed, the non-linearity of the Scheimpflug setup cause the path of the moving flame to become an arc in the time-range map. The signal from the flame also takes up fewer pixels at far ranges than at short ranges due to the different resolution. Figure 3.4(b) shows the data after range calibration. The movement of the signal in time and range is now a straight line, making the constant speed of the flame clear. The width of the flame is also the same across the whole range.

The theoretical range resolutions dependence on range can be determined by taking the pixel position derivative of the range (Equation 3.1), dz_{pix}/dp_{pix}. This is described further in Appendix A. The resulting range resolution is:

$$dz_{pix} = \frac{z_{pix}^2 \mathrm{bcos}(\alpha)[1+\cot^2(\phi)]}{D^2\left[b + p_{pix}[sin(\alpha) - cos(\alpha)\cdot\cot(\phi)]\right]^2} dp_{pix} \rightarrow \tag{3.7}$$

$$\rightarrow\ dz_{pix} = \frac{z_{pix}^2 C}{X_{pix}} \tag{3.8}$$

where C is a range independent constant and:

$$X_{pix} = \left(b + p_{pix}[sin(\alpha) - cos(\alpha)\cdot cot(\phi)]\right)^2. \tag{3.9}$$

The property dp_{pix} would in this case be equal to the pixel pitch l_{pix}. The resolution is dependent on the square of the range, divided by a factor resulting from the position of the pixels along the detector. In cases where $b >> p_{pix}$ (or $f_{rec} >> l_{det}$), X_{pix} is approximately constant for all pixels, resulting in dz_{pix} being directly proportional to the square of z_{pix} Figure 3.5(a) shows an example of an analytical range for a small S-Lidar system (measuring over meters) using a detector with 2048 pixels. Figure 3.5(b) displays the corresponding resolution. The resolution as a function of range instead of pixels is shown in Fig. 3.5(c), exhibiting a z^2 behavior.

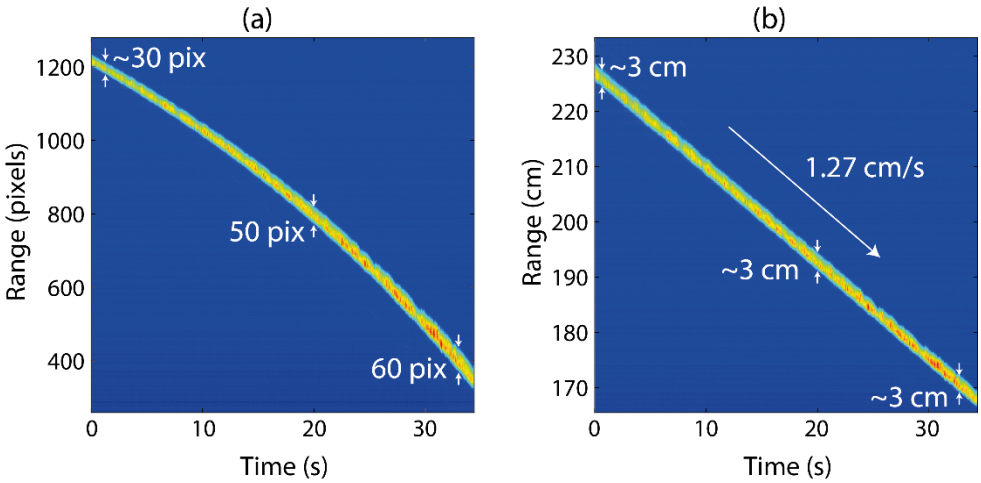

Figure 3.4. (a) Non-calibrated data from a target moving towards the S-Lidar system illustrating the non-linearity of the range scale. (b) The same data after range calibration showing the constant speed of the target.

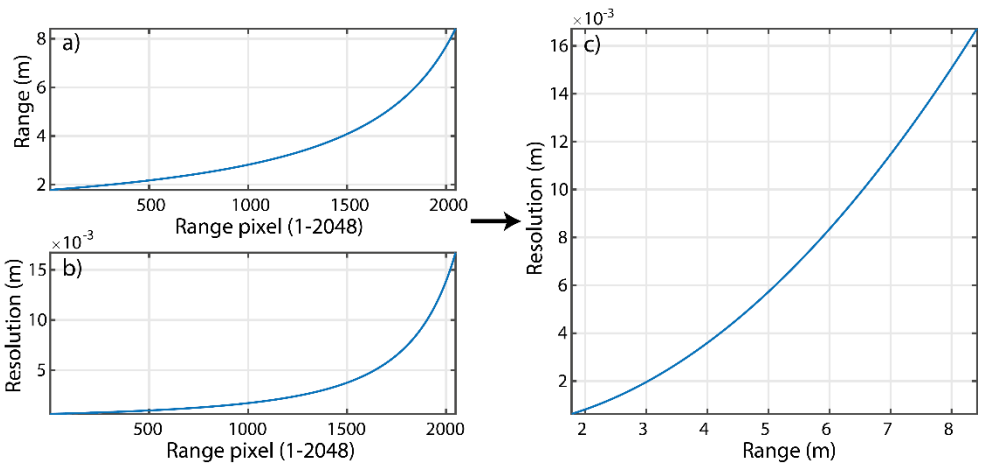

Figure 3.5. a) Example of an analytical range curve as a function of pixel number for a short range system (f_{rec}=0.2 m). b) The corresponding resolution curve. c) Resolution as a function of range.

Equations 3.1 and 3.7 describe what properties of an S-Lidar system that may be changed to adjust the covered range interval, and the attained range resolution. In the design phase, where the optics and detector configuration are chosen (the properties f_{rec}, α, l_{det}, and l_{pix}), the possible range intervals and corresponding resolution is determined. A longer detector enables a larger range interval, while a smaller pixel size, or pitch, results in higher resolution. The choice of focal length affects both the attained range

interval and resolution. A long focal length gives higher resolution, but the size of the system increases too, i.e. the baseline, D, have to be larger. The near-range limit of the system is also increased. This can be seen in Fig 3.6(a), which displays the resolution as a function of range for the same system as in Fig. 3.5 but with different f_{rec}. The focus of each system was chosen in such a way that the maximum range was the same (~8.4 m). The legend displays the resulting D and ϕ for each configuration.

The tilt of the detector, α, is another factor that changes the properties of the system. Increasing α, while keeping f_{rec} constant will give a smaller system (reduced D), but the resolution will decrease, see Fig. 3.6(b). Figure 3.7 displays plots corresponding to those in Fig. 3.6 for a larger S-Lidar system monitoring up to 2500 m. The far-range systems where focused on optical infinity (not seen in figure).

The static properties need to be chosen according to the purpose of the system in question, e.g. a system meant to monitor over hundreds or thousands of meters should have a larger f_{rec} than a system monitoring over tens of meters. If a small system is needed due to limited optical access for example, then a shorter f_{rec} or larger α, may be chosen, at the expense of range resolution. The selection of f_{rec} and α for different systems will be discussed further in chapter 6 and 7.

For a completed system, the monitored range interval may be adjusted by changing, the angle of the system in relation to the laser beam, ϕ, and adjusting the focus (distance b) and baseline accordingly. When the observed range interval is changed, the resolution of the system at a specific range will also be altered. For the larger systems used in this work, which are focused on optical infinity, the baseline is often permanently set according to Eq 3.5, since the small change in D when the focus is changed is negligible.

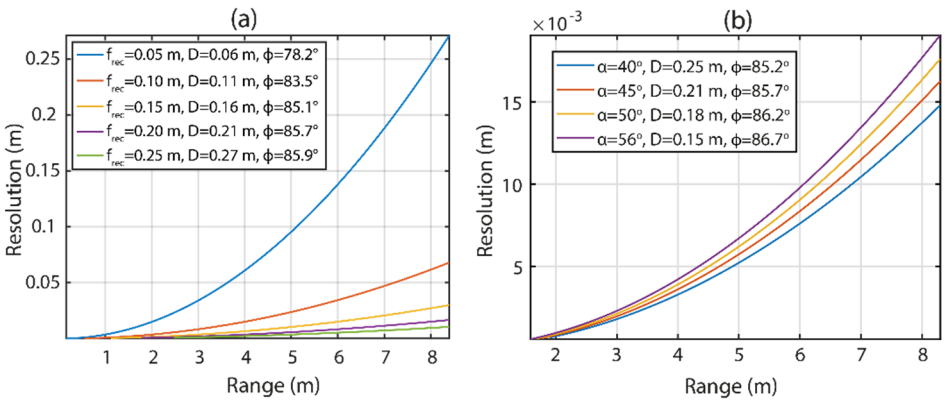

Figure 3.6. (a) Resolution as a function of range for different f_{rec} used in a small S-Lidar system. The maximum range was set to 8.4 m for all configurations.(b) Resolution as a function of range for different tilt of the detector with constant f_{rec} (0.2 m). The angle of the system in relation to the laser, ϕ, is diplayed for each curve.

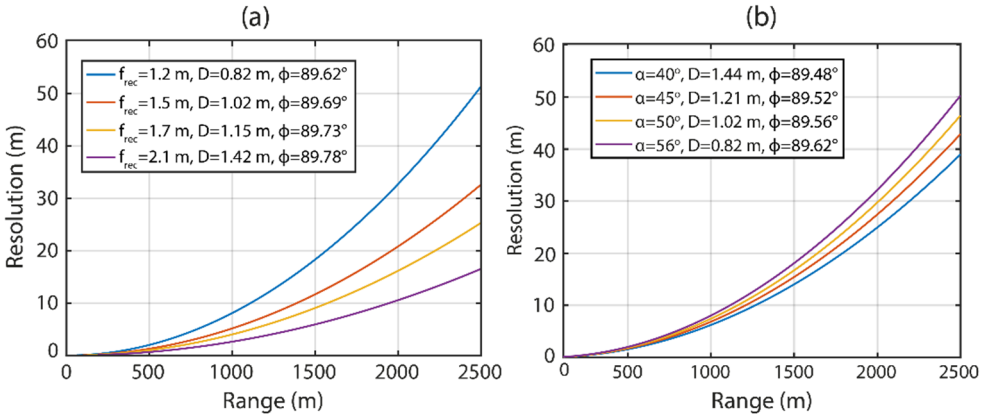

Figure 3.7. (a) Resolution as a function of range for different f_{rec} used in a larger S-Lidar system. The system is focused on infinity (not seen in plot) and the maximum range shown is 2500 m for all configurations. (b) Resolution as a function of range for different tilt of the detector with constant f_{rec} (1.2 m). The angle of the system in relation to the laser, ϕ, is diplayed for each curve.

Chapter 4

Lidar signals

In this chapter, the established equation, describing the signal from a conventional ToF Lidar is presented, followed by a description of how this equation relates to S-Lidar. Finally, the way the width and shape of the beam affect the signal is discussed.

4.1 Conventional Lidar equation

The Lidar equation is a well-established equation describing the properties of a ToF-Lidar signal. In this section, an overview of the important terms in the equation is presented. The equation described here will only take scattering into account, and not describe e.g. fluorescence. The interested reader may find a more in-depth description of the conventional Lidar equation in e.g. [3,5].

The properties of a signal detected by a pulsed Lidar system are determined by the pulse duration and power of the transmitted laser pulse at wavelength, λ_T, the geometrical overlap volume of the laser beam and collection optics, the extinction and scattering properties of the species present in this overlap at λ_T, and scattered wavelength, λ_S. The efficiency of the collection system, the noise and background signal also affect the signal. The detected Lidar signal as a function of distance, z, is described by the Lidar equation. The Lidar equation for a system based on a ToF approach can be seen Fig 4.1. Each part of the equation is described in more detail below. Two assumptions are made in the derivation of this equation. Firstly, the scattering processes are assumed to be independent, i.e. the scattered radiation from many particles has no phase relation, and the total scattered intensity is the sum of all individual intensities. Secondly, we assume that multiple scattering is negligible, and each photon is thus only scattered once.

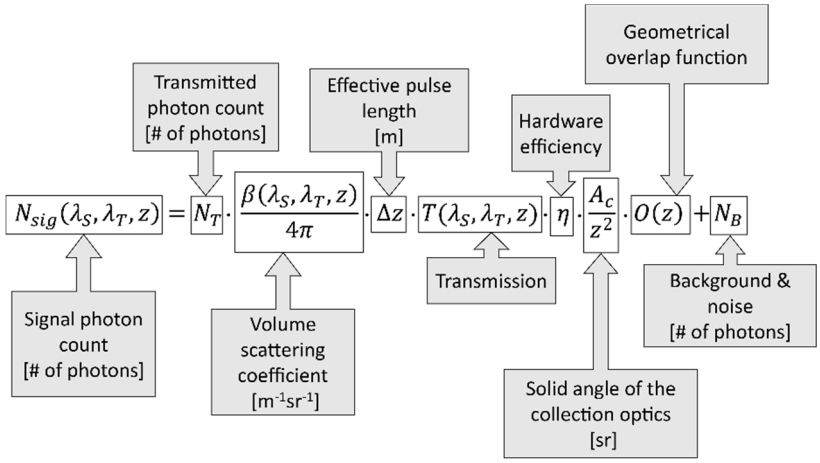

Figure 4.1. The Lidar equation with labels describing the different terms. Here the signal will be described in terms of photon count.

At a specific time, *t*, the detector receives a signal from distance, $z = ct/2$, where c is the speed of light. For a light pulse with duration, τ, the backscattered front part of the pulse will meet the trailing edge of the pulse when it has propagated a distance:

$$\Delta z = \frac{c\tau}{2}. \tag{4.1}$$

Δz is thus the effective pulse length and the system will receive signal from the whole geometrical distance Δz simultaneously. Consequently, Δz defines the spatial resolution of a Lidar system, as long as the detector is fast enough to resolve τ. While the laser pulse travels through the probe volume it will be absorbed and scattered by molecules and particles and its intensity will thus decrease. The transmission, *T*, of the transmitted wavelength, λ_T, and scattered wavelength, λ_S, is given by an integrated version of Beer-Lambert's law:

$$T(\lambda_S, \lambda_T, z) = exp\left(-\int_0^z \alpha_{ext}(\lambda_T, x)dx - \int_0^z \alpha_{ext}(\lambda_S, x)dx\right), \tag{4.2}$$

where α_{ext} is the extinction coefficient. The extinction coefficient at wavelength, λ, and distance, *z*, for species, *i*, is the product of the extinction cross section $\sigma_{i,ext}$ and the number density, n_i. The total extinction coefficient is the sum of the extinction coefficients of all species in the probe volume:

$$\alpha_{ext}(\lambda, z) = \sum_i \sigma_{i,ext}(\lambda) n_i(z)\,. \tag{4.3}$$

The volume scattering coefficient defines the probability that laser light is scattered into λ_S per unit distance travelled. The volume scattering coefficient of a species, i, is given by the product of the full-solid angle scattering cross section, $\sigma_{i,S}$, the number density, n_i, and the probability, p_i, of the scattered photons to have wavelength, λ_S. The total scattering coefficient, β is the sum of the coefficients of the species contained in the probe volume:

$$\beta(\lambda_S, \lambda_T, z) = \sum_i \sigma_{i,S}(\lambda_T) n_i(z)\, p_i(\lambda_S). \tag{4.4}$$

β gives the probability for light to be scattered in any direction per unit distance, but the Lidar signal only consists of light which has been backscattered into the solid angle subtended by the aperture of the receiving optics,

$$\Omega_c \approx \frac{A_c}{4\pi z^2} 4\pi = \frac{A_c}{z^2}, \tag{4.5}$$

where A_C is the area of the collection optics. To relate β to Ω_C, the expression should be divided by 4π. Equations. 4.2, 4.3, 4.4, and 4.5 can be combined with the number of transmitted photons, N_T, to express the number of photons collected by the collection optics, N_C, per scattering length unit:

$$N_C(\lambda_S, \lambda_T, z) = N_T \cdot \frac{\beta(\lambda_S, \lambda_T, z)}{4\pi} \cdot \Omega_c \cdot \Delta z \cdot T(\lambda_S, \lambda_T, z). \tag{4.6}$$

To obtain the number of photons that actually reaches the detector, N_{sig}, the signal has to be multiplied by the system efficiency. The system efficiency consists of two terms. The first is the losses due to the hardware in the system such as mirrors, lenses and filters, called the hardware optical efficiency, η. The second term is the geometrical overlap function $O(z)$ which describes the overlap of the laser beam and the FoV of the receiver optics as a function of distance. Incomplete overlap, i.e. $O(z)<1$ occurs in the beginning of the range, where part of the beam may be obscured from the receiver optics. The overlap between the FoV and the laser beam may also have an offset due to a biaxial configuration of the laser beam and the detection system. The overlap function can be estimated using both theoretical and experimental methods. Analytical overlap functions require very detailed knowledge of the system parameters and experimental conditions to make them accurate enough. The most straight forward way to experimentally determine the overlap function is to extract it from measurements carried out in a clear atmosphere with homogeneous conditions. However, for e.g. vertical atmospheric system this homogeneous assumption does not hold. Experimental methods that overcome this problem use some kind of a reference signal. For Lidars equipped with a Raman channel, the elastic signal may be divided by the molecular N_2

or O_2 Raman signal to obtain the overlap [76]. Other methods compare the signal with data from a ceilometer [77] or are based on comparing signal from different elevation angles [78]. Although the existence of incomplete overlap can cause problems, it may also be used to suppress the difference in signal strength due to the $1/z^2$ dependence, and thus decrease the dynamic range of the signal [5].

Finally, the photon count will contain a contribution from noise and background, N_B. Examples are detector noise, background noise, shot noise etc. The final Lidar equation is:

$$N_{sig}(\lambda_S, \lambda_T, z) = N_T \cdot \frac{\beta(\lambda_S, \lambda_T, z)}{4\pi} \cdot \Delta z \cdot \frac{A_c}{z^2} \cdot T(\lambda_S, \lambda_T, z) \cdot \eta \cdot O(z) + N_B(z) \qquad (4.7)$$

4.2 Lidar equation for S-Lidar

Although the exact nature of system efficiency and geometry might be different in S-Lidar, most of the terms in the Lidar equation can be treated in a similar way as in ToF-Lidar. The range resolution term is the main difference between the techniques. Range resolution in ToF-Lidar is constant across range, while it changes in S-Lidar. The previously introduced Eq. 3.7 shows that the range resolution of S-Lidar is proportional to the square of the range divided by a factor X_{pix}. This factor is dependent on the position of the pixels on the detector, p_{pix}. When the analytical expression for range resolution have been substituted into the Lidar equation (Eq. 4.7), the S-Lidar equation is obtained:

$$N_{sig}(\lambda_S, \lambda_T, z_{pix}) = N_T \cdot \beta(\lambda_S, \lambda_T, z_{pix}) \cdot T(\lambda_S, \lambda_T, z_{pix}) \cdot \frac{C}{X_{pix}} \cdot O(z_{pix}) + N_B(z_{pix}) \qquad (4.8)$$

C is a system function which includes A_C and η (assumed to be constant for all pixels). The main consequence of this substitution is that the analytical signal loses its $1/z^2$ dependence. To put it another way, the fact that less light reaches the detector from far ranges is compensated for by the increase of monitoring volume with increasing range. This concept is illustrated in Fig. 4.2, which displays simple calculated Lidar signal for one of the typical S-Lidar setups used in this work (red) and for a ToF-Lidar (blue). These normalized curve are meant to be illustrative of the difference in signal strength over range. They are simulated assuming signal from a homogenously distributed gas across the whole range, i.e. the number density is assumed to be constant, leading to constant scattering and extinction coefficients. Complete overlap is also assumed, i.e. $O(z) = 1$, and N_B is set to zero. The resolution for the ToF signal is set to 1 m. Despite the small change in signal strength across the range (~3%), it is clear from the figure that the S-Lidar does not have a $1/z^2$ dependence and may be considered flat, especially

in comparison to the fast decaying ToF-signal. This points to an advantage of the non-linear range scale of S-Lidar, which may otherwise be considered a drawback, namely the fact that it delivers signals with a small dynamic range. It is important to point out that although the signal intensity in each pixel is approximately the same in S-Lidar, less signal is still collected from far distances than from short; see clarification in Fig. 4.3.

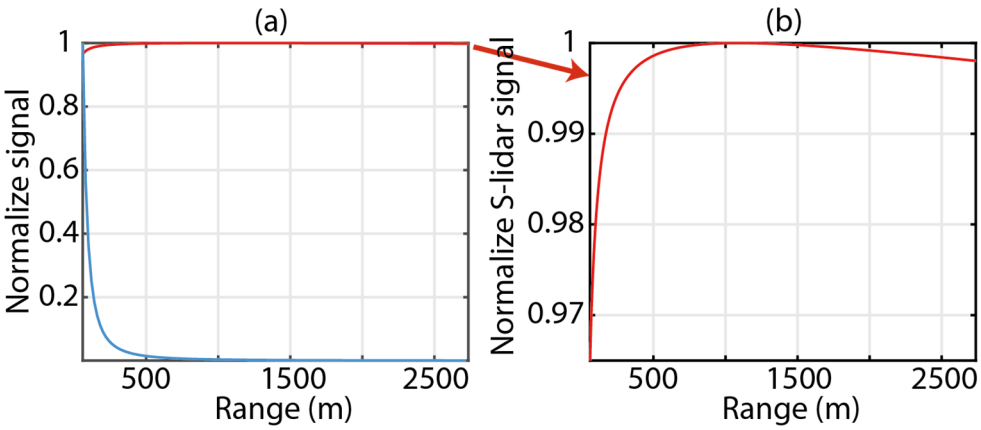

Figure 4.2. (a) Simulated Lidar signals for a S-Lidar setup (red) and a ToF setup (blue). Both curves are normalized.The S-Lidar curve is almost flat across the range while the ToF curve is very high at short ranges and low at far ranges.(b) Closer view of the S-Lidar signal.

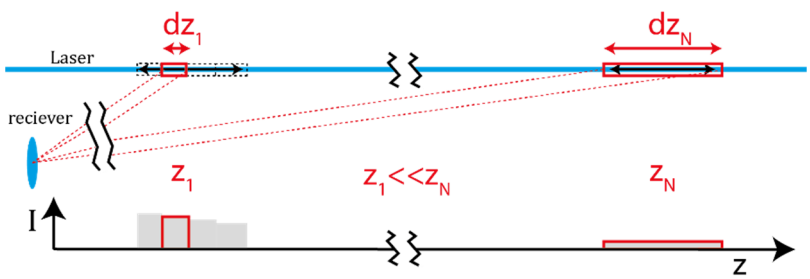

Figure 4.3. Two identical homogenous objects (marked by the black arrows) are placed at different ranges, z_1 and z_N. The collected signal from the whole object at range z_N will be less than the signal collected from range z_1, accordig to $1/z^2$ dependence of backscattering. This may be seen in the histogram in the lower part of the figure. The total grey area is larger at the short range than at the far range. However, the signal collected by an individual pixel, (marked red in histogram) are approximately the same at the two ranges due to the non-linear range scale of the S-Lidar ($dz \propto z^2$). The larger range interval of pixel z_N means that it collects all the signal from the object while pixel z_1 only collects part of it. This gives a flat signal across pixels.

The small change in S-Lidar signal seen in Fig. 4.2 is caused by the range dependence, or more accurately the pixel position dependence, of the factor X_{pix} in Eq 4.8. In cases where $p_{pix} \ll b$ ($l_{det} \ll f$), the factor X_{pix} is approximately constant for all pixel positions resulting in a signal whose shape across range can only be affected by the scattering coefficient, $\beta(z)$, the transmission, $T(z)$, and the overlap function, $O(z)$. The effect of constant extinction across the range is indeed seen as a small dip in signal at far ranges for the S-Lidar signal in Fig. 4.2(b).

4.2.1 Shape and width of the beam

This far, the width of the laser beam has not been taken into account when discussing the signal and resolution of S-Lidar. For an infinitely narrow beam the resolution, dz, of S-Lidar is only constrained by the trigonometrical principles of the Scheimpflug and hinge intersections (assuming high image quality of the receiver optics), and Eq. 3.1-3.9 hold true. For a beam with a finite width, the footprint of a pixel will overlap in range with the footprints of adjacent pixels. The range resolution will thus degrade substantially compared to dz (see Fig. 4.4). This is comparable to how temporal properties such as bandwidth and detector rise time limit the range resolution in ToF Lidar (see more in Appendix B). The decrease in resolution of S-Lidar will be determined by the sampling angle γ, i.e. the angle between the laser plane and the pixel footprint, and the width of the beam, $w(z)$. The distance over which the full width of a pixel footprint samples the beam is here called the effective range resolution, dz_{eff}. For a collimated beam it can be approximated with (if $dz \ll dz_{eff}$):

$$dz_{eff} \approx \frac{w(z)}{\gamma(z)} \approx z\,\frac{w(z)}{D}\,, \tag{4.9}$$

where D is the baseline defined in Fig. 3.3 [12]. The effective range resolution is thus proportional to the width of the beam, indicating the importance of beam shape when designing a S-Lidar system.

Although the range dependence of the resolution changes when the laser beam has a finite width, the S-Lidar equation (Eq. 4.8) still holds true, assuming a collimated beam and a uniform distribution of light intensity along the width of the beam. The reason for this is that the area sample by a pixel along dz_{full} (the pink area in Fig. 4.4(a)) is equivalent to the area sampled along dz if the beam was fully sampled across its whole width (the green area in Fig. 4.4(a)). The pixel will detect the same signal intensity as it would if it only observed signal in the range interval dz. The Lidar signal will thus not change shape. This does not hold true if the beam is not collimated (see Fig. 4.4(b)), since the distance (dz_{eq}) needed to generate an equivalent sampling area as the one sampled along dz_{full} is not equal to dz anymore. The Lidar curve would in this case be distorted but could in principle but be corrected with a factor dz/dz_{eq}. However, this is

difficult to achieve in practice since dz_{eq} is hard to determine. More details on this may be found in [12].

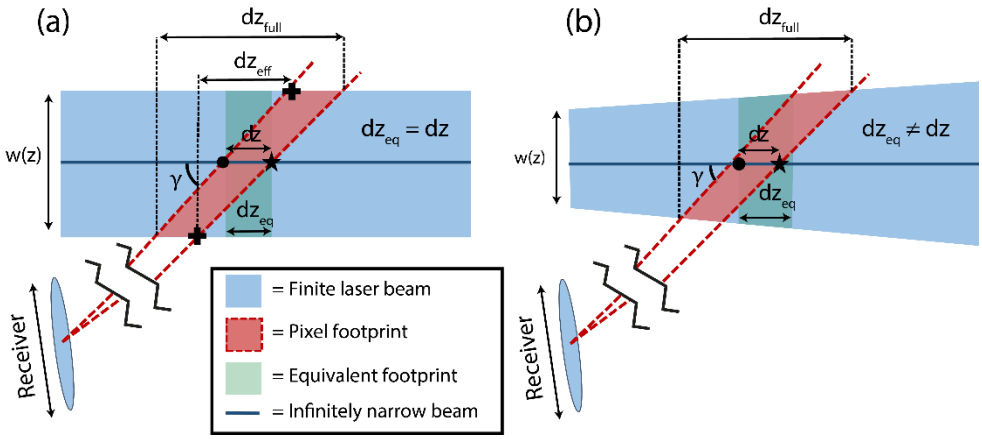

Figure 4.4. Schematic illustration of how the width of the beam affects the range resolution. The pixel footprint collects signal from a larger range interval compared to the case with an infinitely narrow beam (dark blue line). (a) The case with a collimated beam where $dz = dz_{eq.}$ (b) The case with a non-collimated beam, where. $dz \neq dz_{eq}$.

4.2.2 Raytracing

Equation 4.9 is a rather simplified view of the effect of the beam width on the resolution, where e.g. the geometrical overlap between adjacent pixel footprints, the possible divergence or convergence of the beam, and the intensity profile across the beam are not taken into account. A ray tracing program that takes these considerations into account has been developed. The program is presented more thoroughly in paper III. In this program a 3D beam with a Gaussian cross section is created and divided into volumes cubes, or voxels, represented by dots in Fig. 4.5. The full width half max, (FWHM) of the beam cross section is set to half of the transmitter aperture. The overlap between the sampling angles of the pixels (γ) and the volume cubes is used to attain a sensitivity profile over range, illustrated in the lower part of Fig 4.5. The histogram shows the number of cubes at each range overlapped by the pixel footprint. This corresponds to the range sensitivity curve of the pixel and the FWHM of this distribution gives the range uncertainty, Δz. The cubes at the edge of the beam are weighted less than those in the center according to the Gaussian beam profile. Due to potential beating between the discretized pixels and volume cubes, random noise must be added to the spatial coordinates of the volume cubes.

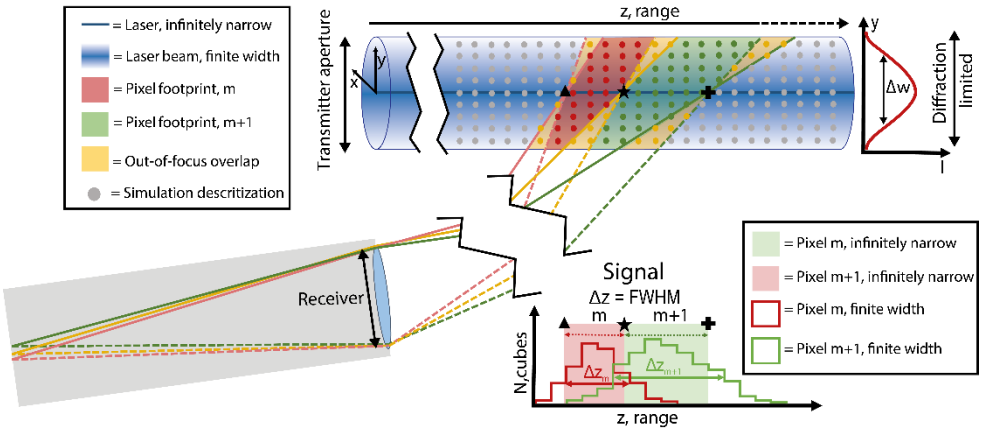

Figure 4.5. An illustration of the principles of the Scheimpflug Lidar raytracing program, which among other things calculates range for beams of different widths and shapes. The laser beam (blue area) is divided into discrete volume cubes represented by dots. The observed volumes of two adjecent pixels (*m* and *m*+1) are shown as a green and red area. Their out-of-focus overlap inside the beam is marked with yellow. The plots in the lower part of the figure show the number of volume cubes each pixel footprint overlap at each range. The FWHM of this distribution defines the resolution for the corresponding pixel and its area corresponds to it signal strength. If the laser beam was infinitely narrow, represented here by the dark blue center line, the two pixel footprints do not overlap in range inside the laser beam, as shown by the red and green shaded boxes in the lower plot. The spread of the signal in range, for this case, is only determined by the Scheimpflug principle and hinge rule, as well as by the image quality of the reciever.

Figure 4.6 displays the resolution of simulated S-Lidar signals for different transmitter aperture sizes and therefore also different shapes of the beam. In this case the focal length of the transmitter is changed with the aperture so all the cases have a f-number of 5. The focus of the beam is placed at the termination where the size of the beam in the y-direction is diffraction limited (see more about this in Chapter 6). This example illustrates how the degradation of the range resolution with increasing range may be compensated for by shape of the beam. A small transmitter aperture (yellow curve) will result in a narrow beam at short ranges but a large beam size at far ranges, exasperating the problem of resolution degradation with range. A large aperture on the other hand, will result in a wide beam at short ranges, degrading the resolution there, but a sharp focus at far ranges giving a higher resolution. For the case shown by the blue curve in Fig. 4.6, the resolution is in fact higher at far ranges than at short ranges. Finally, the red curve displays a case where the beam shape is approximately compensating for the degradation of resolution due to the trigonometrical constraint. The resolution then degrades almost linearly with range.

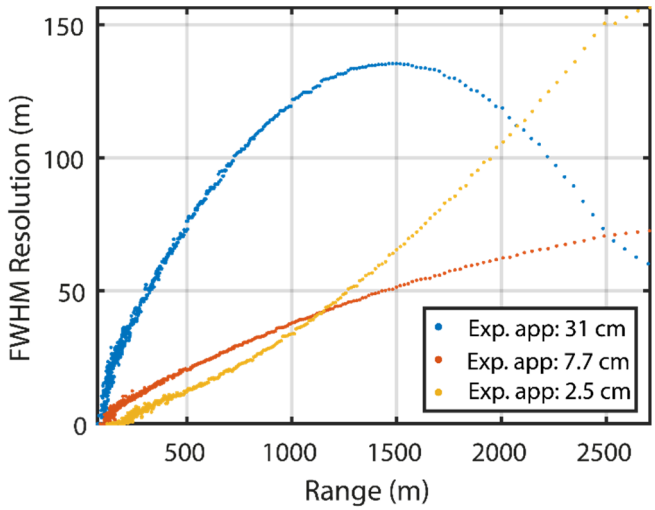

Figure 4.6. Simulated resolution curves from a Scheimpflug system with different beam size. The size of the transmitter aperture is not the same for the different curves, resulting in an altered beam shape which,in turn, leads to a difference in resolution. The resolution curves for a infinitely narrow beam for the same system (f_{rec}=1.2) are shown in Fig. 3.7.

4.2.2.1 Geometrical overlap

The full height of the beam may not fit within the pixel footprints at short ranges. This incomplete overlap result in only part of the beam being imaged onto the detector. The nature of the overlap depends on the aperture size of the expander (transmitter) telescope, d_{exp}, and how the divergence of the beam matches the divergence of the FoV. The divergence of the of the FoV is determined by the height of the pixels h_{pix}, and the focal length of the receiver telescope, f_{rec}, while the divergence of the beam is determined by the width of the LD chip, l_{LD}, and the focal length of the expander telescope, f_{exp}. Figure 4.7 shows four illustrative examples where different combinations of f_{exp} and d_{exp} are used in a system with a fixed l_{LD} , h_{pix}, and f_{rec}. If the expander aperture is large, and the beam divergence is larger than the divergence of the FoV, complete overlap is never achieved. For a S-Lidar system focused on infinity, with a beam divergence less than the divergence of the FoV, the range at which complete geometrical overlap occurs is approximately given by:

$$z_{comp} = \frac{d_{exp}}{\frac{h_{pix}}{f_{rec}} - \frac{l_{LD}}{f_{exp}} + \frac{d_{exp}}{z_{term}}}. \tag{4.10}$$

Here z_{term} is the termination range. The expression is obtained by using the thin lens formula to estimate the size of the pixel footprint (FoV) and the laser beam at each range.

As discussed briefly in section 4.1, to extract the full overlap function is a rather complex problem. For most practical applications in this thesis work it has been possible to use the atmospheric echo from the clear atmosphere to calibrate the signal. Most of the measurements, both in the field and in the lab have been carried out using horizontal laser transect.

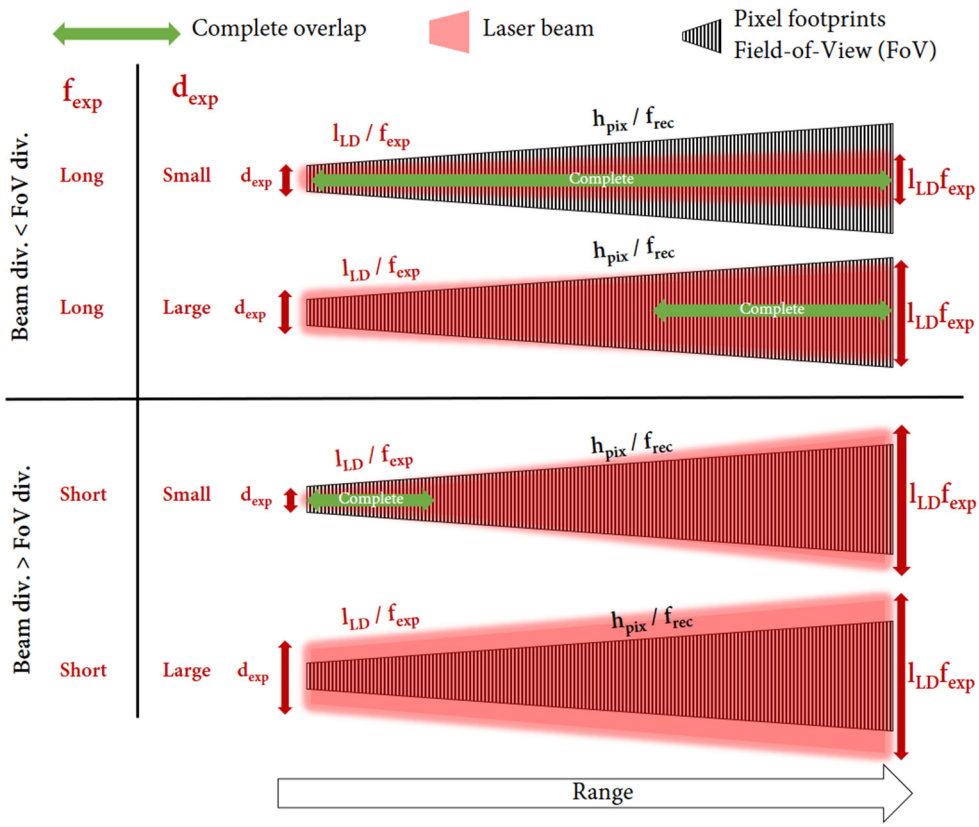

Figure 4.7. An illustration of geometrical overlap between the laser beam and the FoV. The upper part of the figure shows two cases where the beam divergence is less than the divergence of the FoV, while the opposite is true for the cases in the lower part.

Chapter 5

Experimental equipment

5.1 Lasers

Lasers are devices which emit light though optical amplification of stimulated emission. Population inversion is created in a gain medium through pumping, and an optical resonator placed around the medium creates phase matched optical feedback. The light emitted by a laser is thus spatially and temporally coherent, often monochromatic and has a high photon flux. The properties of the light, such as wavelength, spectral band width, pulse duration and divergence can often be customized for the specific application. This makes the laser an invaluable optical tool in many research fields and practical areas, including remote sensing.

There are many different types of lasers, with widely varying size, output power and wavelength. The type of laser utilized in this thesis work is mainly CW laser diodes, but a pulsed Nd:YAG (neodymium-doped yttrium aluminum garnet) laser has also been used. The principles of both types of lasers are described in this section, the Nd:YAG laser somewhat briefly, while the LD and its properties is described in more detail. More detailed descriptions of lasers may be found in e.g. [57,79,80]

5.1.1 Nd:YAG lasers

Nowadays, the Nd:YAG laser is a very common type of laser, since its properties make it favorable for short pulse, high power lasing, and thereby, laser diagnostics requiring high time resolution and high pulse energies. The active medium in an Nd:YAG laser, is trivalent neodymium ions, Nd^{3+}, housed in a Yttrium Aluminum garnet crystalline host material ($Y_3Al_5O_{12}$). It is a four-level laser pumped by e.g. flash lamps. Pulsed Nd:YAG lasers often use Q-switching, where an optical switch in the laser cavity allows the population inversion to reach it maximum before light is emitted. The most commonly used lasing transition gives radiation with a wavelength of 1064 nm. This

light can then be frequency doubled, tripled or quadrupled with non-linear crystals to obtain the second (532 nm), third (355 nm) and fourth harmonic (266 nm). The laser used in this work was a pulsed Nd:YAG (Quantel, Brilliant b) with a repetition rate of 10 Hz and a pulse length of 5 ns. The wavelength utilized was 355 nm, i.e. the 2nd and 3rd harmonic generators were thus employed. The laser pulse energy of the laser was roughly 60 mJ at 355 nm.

5.1.2 Laser diodes

The design of a LD is often more simple, robust and compact than high-power pulsed laser systems. In the last decade, the efficiency of LDs has increased significantly, resulting in output powers of several Watts from devices smaller than a centimeter. These small devices may be mass produced, which means that they are less expensive than many other high power laser sources.
A LD is a semiconductor laser in which gain is achieved by placing a forward bias voltage on a heavily-doped p-n junction, see Fig. 5.1(a). Electrons from the n-type side will recombine with holes from the p-type side at the active region of the p-n junction. In terms of energy, this process corresponds to electrons in a conduction energy band decreasing their energy down to a valence band and emitting light, as shown in Fig. 5.1(b). The wavelength of the emitted light depends on the bandgap of the semiconductor material in question, i.e. the energy difference between its conduction and valence band. Materials used for laser diodes have direct bandgaps, meaning that direct radiative transitions are allowed. Laser diodes emitting blue light often use GaN (galium nitride) or GaAs (gallium arsenide). Figure 5.1 shows the simplest and very inefficient version of a LD, where only p-doped and n-doped material are sandwiched together. Modern LDs use a double heterostructure, (p-i-n structure), where a thin layer of a semiconductor material with a narrow bandgap is sandwiched between the p-type and n-type layers. This results in a very thin active region, where electron-hole pairs exist simultaneously and contribute to the amplification. This layer acts as a waveguide for the light. Most LDs are emitted parallel to the laser resonator (edge emitting), as shown in the Fig. 5.1, but there are also types where the laser light is emitted perpendicular to the crystal layers (surface emitting).

The recombination process in a diode may happen spontaneously, resulting in a light emitting diode (LED), or, as in the case of the LD, be stimulated by incident photons, creating optical amplification. Through optical feedback, often implemented by cleaving the semiconductor crystal along its planes and using the cleaved surfaces as reflectors, a laser resonator is established. For lasing to occur, the current injected into the LD has to be high enough to achieve a gain that is larger than the losses. This means that below a certain threshold current, I_{th}, a LD functions like a LED emitting small amounts of spontaneous emission which is spectrally broad and have high divergence. This concept is illustrated in Fig. 5.2(a). The threshold current of a LD is shifted when

the temperature is changed due to a change in the gain, as can be seen in Fig. 5.2(b). The threshold current is described by:

$$I_{th} = I_0 \exp\left(\frac{T}{T_0}\right) \tag{5.1}$$

where I_0 and T_0 are constant for a specific diode.

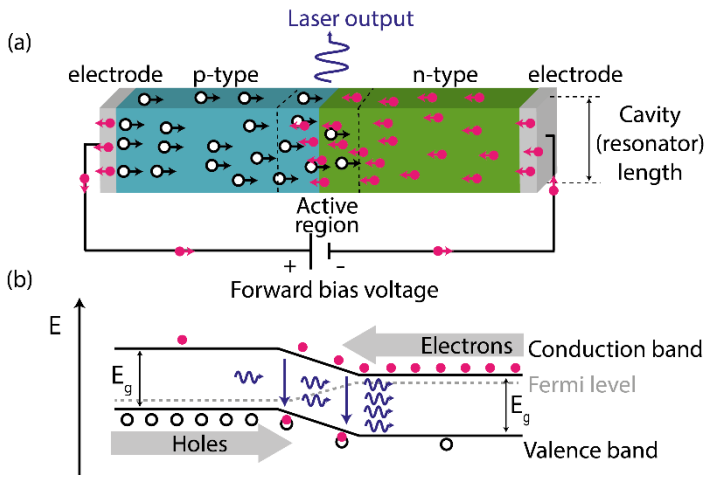

Figure 5.1. (a) Schematic of a simple forward bias p-n junction used in a LD, where electrons and holes recombine in the active region. (b) The corresponding energy diagram showing the recombination across the bandgap, E_g.

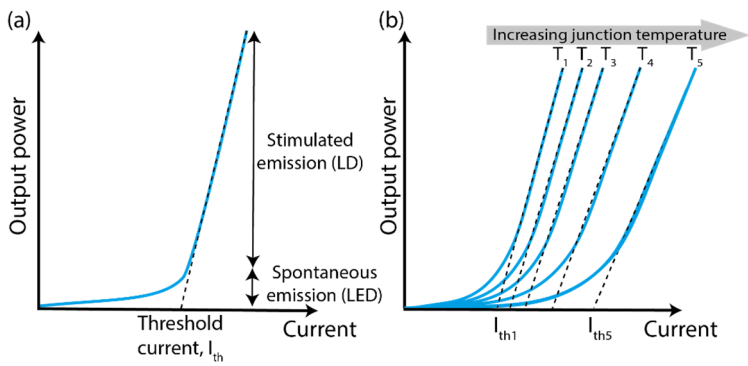

Figure 5.2. Power-current characteristics for a LD. (a) A certain threshold current must be reached before the LD starts lasing. Before the threshold current is reached the LD emits spontaneous emission like a LED. The light is then incoherent and spectrally broad. (b) The position and slope of the curve will change depending on the temperature of the LD. Increasing temperature will move the curve towards higher currents.

Figure 5.3 shows the current-voltage characteristics of a 405 nm LD for different temperatures. In an LD, substantial current only flows above a critical voltage, U_0, a property which is related to the bandgap and temperature of the semiconductor material. With increasing temperature, the bandgap decreases and therefore also U_0, resulting in a shift of the curve towards lower U. Higher temperature also means higher conduction, resulting in a steeper slope of the curve. This is the reason why LDs should not be operated with a constant voltage source, since this may lead to a run-away effect with increasing temperatures and currents. Figure 5.3 shows that the same voltage results in different currents for different temperatures.

The output power, P, is described by:

$$P = \eta(I_{LD} - I_{th})U_0 \rightarrow \eta_{in}\eta_{em}(I_{LD} - I_{th}) \cdot \frac{hc}{\lambda e}, \tag{5.2}$$

where η is the total quantum efficiency, η_{in} is the internal quantum efficiency and η_{em} is the emission efficiency of the LD, h is Planck's constant, c is the speed of light, λ is the emitted wavelength, I_{LD} is the operating current, and e is the elementary charge. A higher quantum efficiency will result in a steeper slope of the U-I curve which means less heat losses.

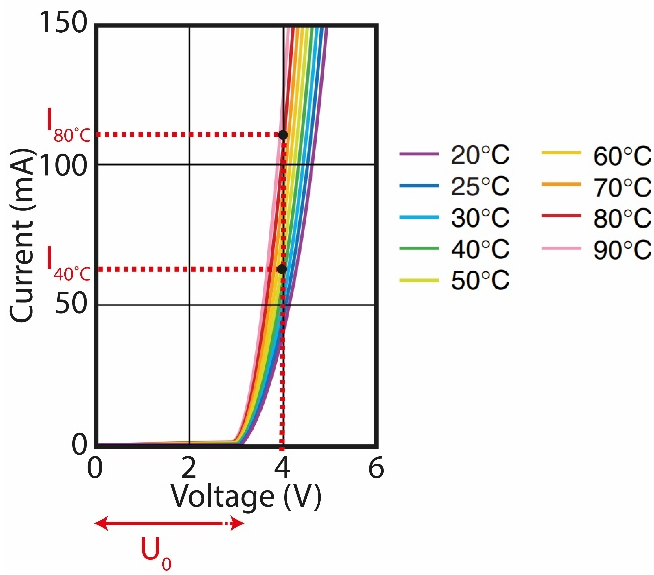

Figure 5.3. Current-voltage characteristics of a typical LD at different temperatures. When the voltage is kept constant the current can change drastically with temperature. The currents at 4V at two different temperatures are marked in the figure, illustrating why you should not run a laser diode on a constant voltage source.

There are two parameters that cause the emission wavelength of an LD to change, namely temperature and injection current. A change in temperature shifts the wavelength since it changes the bandgap of the semiconductor material. How large this wavelength shift is, depends on the wavelength of the LD. The shift is larger for long wavelengths than for short, but it is usually of an order of magnitude of one or a couple of tenths of nm per Kelvin. An alternative way to tune the wavelength is by changing the driving current of the LD, since this will change the refractive index of the semiconductor material in the junction. The effective length of the resonator will thus change, resulting in a shift in wavelength. The change in current will also lead to a change in temperature, which will enhance this effect even further.

Most of the diode lasers utilized in this thesis work, such as those reported in paper I-V, are simple multimode lasers with a bandwidth on the scale of nm. The emission wavelengths of these LDs are 405, 445, and 808 nm, with an output power in CW operation of 0.5-5 W. The sizes of the laser chips are either 1x100 µm (NIR) or 1x20 µm (blue).

The diode lasers utilized in the work presented in paper VI are external cavity diode lasers (ECDL) which are tunable, single-mode lasers [81]. In ECDLs, the laser diode is aligned with a diffraction grating in such a way that the 0^{th} order diffracted light becomes the output beam and the first order diffracted light is reflected back into the laser cavity where it will dominate the feedback mechanics, forcing emission at only one longitudinal mode. The generated wavelength will thus not be governed by the bandwidth of the LD but by the grating. The wavelength can be tuned by tilting the grating using piezo actuators. The emission wavelengths of these tunable lasers are around 410 nm and 451 nm and their linewidth is less than 1 MHz (~1 fm at a wavelength of 450 nm). The output power is approximately 5 mW.

5.2 Detectors

Two types of optical detectors, both semiconductor based, have been utilized in this work, namely CCD (Charge Coupled Devices) and CMOS (Complementary Metal Oxide Semiconductors) detectors. Both types of detectors consist of arrays of pixels which converts light into electrons through the photoelectric effect, which in turn are converted into an electrical signal. The main difference between the two detector types is how the charge in each pixel is converted into voltage. The charge collected in each pixel on a CCD chip is shifted along the pixel rows to the edge of the chip where it is amplified and converted into voltage [42]. In contrast, each pixel on a CMOS chip has its own charge-to-voltage conversion, and amplification. CMOS detectors often provide a faster readout than CCD detectors, but their image uniformity is lower.

Line-array detectors have been used in most of the S-Lidar applications in this work. A line-array detector can provide a large chip on which the beam can be imaged,

covering an extended range interval in S-Lidar applications, and still allow high sampling rate. The high sampling rate is necessary to provide high temporal resolution. The line array camera utilized in most of the work presented in the papers is of CMOS type and has a maximum sampling rate of 4 kHz. The data presented in Paper I, were acquired using a CCD line array camera. More information about the cameras is given in Table 5.1.

For some of the measurements carried out in flames, e.g. those discussed in Paper VI, a 2D intensified CCD (ICCD) camera was utilized. An ICCD camera has an image intensifier mounted in front of the CCD chip. It amplifies the collected light before it impinges on the CCD chip. The light is converted into electrons when it strikes a photocathode. The electrons are then accelerated towards a higher-voltage microchannel plate (MCP), where they cause multiple electrons to be released. These multiplied electrons are then converted back into light when they hit a phosphor screen. Besides amplification, the image intensifier also enables very fast time gating by controlling the voltage across the MCP. The details of the ICCD camera utilized may be found in Table 5.1.

5.3 Burners

Two types of burners have been utilized in the measurements reported in this thesis. The first type of burner is a standard-type Bunsen burner. This burner consists of a simple pipe through which the fuel/oxidizer mix flows. The resulting flame has a conical shape, as shown previously in Fig. 2.11. A horizontal laser beam transmitted through the flame will thus cross all the different flame zones twice.

The second type of burner is a porous-plug burner. It is made of a sintered metal plug through which the fuel and oxidizer flows. It is one of the most commonly used burners in basic combustion research since it delivers a stable, well-defined, one dimensional flame. In contrast to the Bunsen burner, the progression of this type of flat flame only depends on the height above the burner (HAB) surface, resulting in the same flame environment, i.e. temperature and species concentrations, across the whole flame at a specific height.

Table 5.1. Detector details.

Manufacturer	Synertronic Design	Princeton Instruments	DALSA Teledyne
Model	Glas-Z	PI-MAX 4	Spyder3
Sensor type	CMOS	ICCD	CCD
Chip elements(pixels)	1x2048	1024x1024	2x2048
Pixel size (μm)	200x14	13x13	14x14
Spectral sensitivity (nm)	280-1000	350-950	280-1000
Max readout rate (Hz)	4000	7.7*	18000
Dynamic resolution	6-bit	16-bit	12-bit

*Refers to a configuration using all pixels and no binning.

Chapter 6

Aerial fauna monitoring

The larger Lidar systems described in this thesis have typically been used for measurements from around 30 m to between 0.5-2 km. The measurements have mainly been focused on monitoring flying insects but other aerial fauna, such as bats, have also been reported on. In this section the S-Lidar system is described, including some experimental considerations. The different field campaigns aimed at aerial fauna monitoring, carried out during this work are briefly described, and typical data are presented. The method used for data analysis is described and examples of the final data product are shown.

6.1 Instrumentation and design considerations

Figure 6.1 displays a typical S-Lidar system utilized for aerial fauna monitoring. The whole setup is placed along an aluminum bar, mounted on an equatorial mount. The output from either one or two LDs has been used during this work. A system with two lasers is described here. If e.g. spectroscopic or polarimetric information is desired, the two lasers may have different wavelengths or different polarizations, respectively. The output beams from the laser diodes are overlapped using a beam splitter cube, after which they are expanded and transmitted into the atmosphere by a refractor telescope (typically d_{exp} ~0.10 m, f_{exp}=0.5 m). A Johnson counter is used to alternately trigger the different laser drivers in synchronization with the camera exposures. Every third exposure will not trigger any laser, yielding a background signal, and enabling online background subtraction. This is described in more detail in [12]. The backscattering from the beam is collected by a Newton telescope. (typically f_{rec} = 0.8 or 1.2 m), and detected by a CMOS line-array detector, placed in Scheimpflug configuration with the laser beam. The system is focused in such a way that the pixels observing the ranges farthest away are focused on optical infinity. A bandpass filter, with a FWHM of ~3-10 nm, a longpass filter, and a linear polarization filter are placed in front of the detector

to remove background signal. This is especially important during daytime measurements. The beam and beam termination are monitored by a CCD-camera, through a second refraction telescope placed in between the expander and the transmitter telescopes. A longpass filter is placed in front of the monitor camera to be able to see the beam during daytime. Appendix C contains a description of how a typical system is assembled and aligned. Figure 6.2 shows pictures of two S-Lidar systems deployed in the field during measurement campaigns in Ivory Coast and Tanzania.

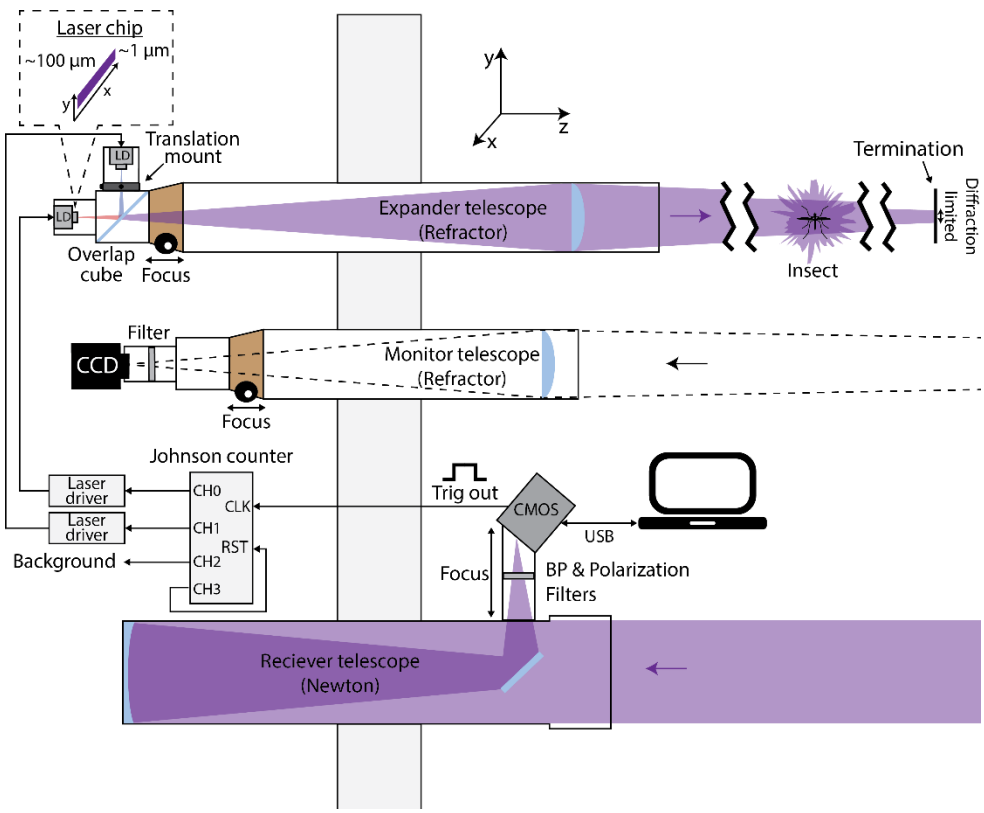

Figure 6.1. Schematic drawing of a S-Lidar setup used for aerial fauna monitoring. This version of the setup has two lasers with different properties. Their output beams are overlapped and transmitted into the atmosphere by a refractor telescope and the signal is collected with a Newton telescope and imaged onto a line-array detector. The output of the lasers are alternately triggered by the exposure of the detector, using a counter. Every third exposure gives a background signal. Another refector telescope and CCD camera are used to minitor the beam and the termination.

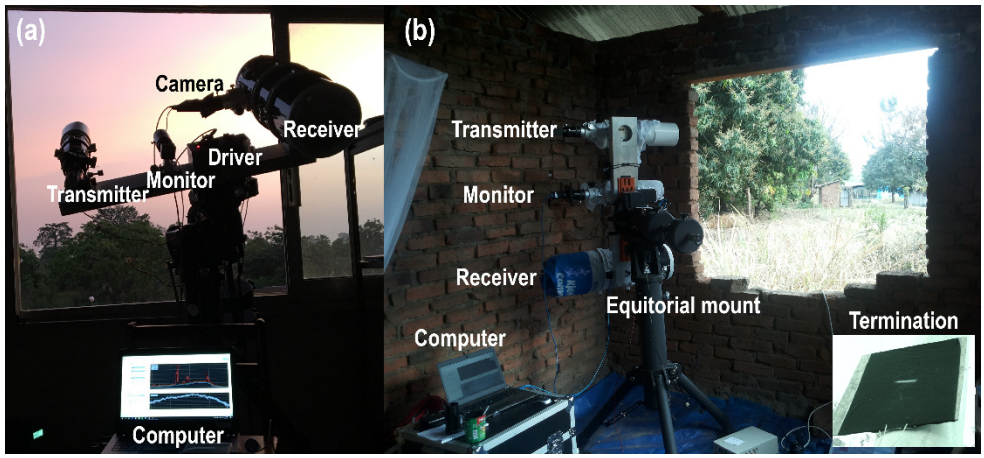

Figure 6.2. Pictures of S-Lidar systems deployed in the field during field campaigns in (a) Ivory Coast and (b) Tanzania. A NIR image of the laser termination may be seen in the inset at the bottom right corner.

To ensure the optimum range resolution, the laser beam should be as narrow as possible in the direction parallel to the baseline of the system (y-direction in Fig. 6.1). At the focus range (often at the laser termination), the laser spot will be an image of the LD chip according to the principles of conventional imaging with a lens. The LDs are thus positioned in such a way that the narrow part of their chips lies parallel to the y-direction, giving the sharpest focus in this direction. The narrow part of the laser chip is smaller than the diffraction limit, meaning that the actual size of the beam at the focus is diffraction limited. Depending on the wavelength and dimensions of the chip, this may also be the case for the beam size in the perpendicular direction. In general, the beam transmitted from this kind of system is shaped like a typical toothpaste tube. The original beam emitted at the output of the telescope has a circular shape due to the circular telescope aperture, while at the laser termination i.e. at the focus, the beam spot is an enlarge image of the rectangular laser chip. A NIR picture of the termination spot is shown in the inset of Fig. 6.2(b).

The lasers used for aerial fauna monitoring have an emission wavelength of 808 nm, and a typical power of 2-3W. Using NIR wavelengths instead of visible wavelengths for fauna monitoring have several advantages. It is preferable when eye safety is considered but also because pigment absorption in the body and wings of insects, especially by melanin, interferes less with the signal. As discussed in Chapter 2, this means that longer wavelengths give higher total signals from insects and more uniform signal level from different parts of the body and wings. This makes e.g. optical size determination easier. It might be even more advantageous to use wavelengths in the SWIR region, since they have been shown to be rather insensitive to melanization. This has been tested in the laboratory using the common SWIR wavelength 1550 nm [66], and

during preliminary measurements on atmospheric insects [82]. Another advantage of using wavelengths in NIR or SWIR is that insect vision is not sensitive in this wavelength range [83,84]. This means that the laser light will not visually disorient the flying insects, resulting in less perturbing measurements. This is further discussed in section 6.2.3. The difficulty of using 1550 nm in atmospheric applications is partly because the optical alignment is more complicated. The beam cannot be observed with the monitoring CCD camera, and the line-array camera required to detect these wavelengths is more expensive. Scattering from the atmosphere is also weaker at longer wavelengths which can cause problems, for e.g. calibration with the air signal.

As described in Eq. 5.1 and Eq. 5.2 the output wavelength of the laser changes with temperature. If the temperature of the laser diode is altered, either due to heat generated by the diode itself or changes in the surrounding temperature, the wavelength of the laser light may drift outside the transmission wavelength window of the filter in front of the detector. The detected signal strength will then decrease, or even vanish. Changes in wavelength due to altered temperature has been an issue during some measurements campaigns, especially since the center wavelength of the utilized laser diodes may differ from the specified wavelength. If this is indeed the case, the laser wavelength may not lie in the center of the filter transmission window to begin with. The main problem during this work has been the modulation of the laser. The temperature of the laser will decrease if it is run on a 50% or 33% duty cycle and the wavelength will drift accordingly (more for long wavelengths than short). By tilting the filter, it is possible to shift the transmission window of the filter and thus compensate for the wavelength change due to the decrease in temperature. However, it would be beneficial to implement some type of temperature control of the lasers to deal with the issue of drifting wavelength, whether it is due to the duty cycle of the laser or substantial temperature differences in the environment.

The emission of the lasers is linearly polarized. This fact may be utilized to perform polarimetric measurements, as it is in the study presented in Paper IV and [22]. The output of two identically linearly polarized lasers are overlapped using a polarizing beam-splitter cube. The polarization of one of the lasers is turned 90 degrees before the laser outputs are overlapped, using a half-wave plate. One of the lasers is p-polarized in relation to the sensor. A linear polarization filter aligned with the polarization of this laser is then placed in front of the detector. When the laser outputs are alternated, one exposure will contain only co-polarized light, one only de-polarized light, and one the background. The co-and de-polarized signal components from e.g. an insect can then be used to attain its depolarization ratio, or DoLP (see section 2.1.2).

As mentioned previously, the tilt of the detector affects the size of the system as well as the achievable range interval and resolution. This should be taken into consideration when choosing the detector tilt. A larger angle gives a smaller baseline (see Fig 3.3), but the near limit of a system with focus at infinity, given by

$$z_{near} \approx D \frac{f_{rec} + l_{det} sin(\alpha)}{l_{det} cos(\alpha)} \quad (6.1)$$

will increase. The detector tilt for most measurements presented in this thesis has been either 40 or 45 degrees. More recently, an angle of 56 degrees has been used since this matches the Brewster angle of the glass in front of the detector (see section 2.1.5). Light that is p-polarized should then be perfectly transmitted. A linear polarization filter, which rejects light with polarization perpendicular to the plane of incidence (s-polarization), is then placed in front of the detector. This filter thus removes stray light and prevents artifacts on the signal resulting from multiple reflections in the thin glass window.

The sampling rates used for the work presented here have been 1.8-4 kHz. For a system with only one laser this will result in an effective sampling rate of ~1-2 kHz after background subtraction, while the effective sampling rate of a system with two lasers would be 0.6-1.3 kHz. Ideally, the highest available sampling rate would be used, since this will better resolve the wingbeats of insects, but in practice the desired sensitivity of the system has to be considered. A higher sampling rate results in a shorter exposure time and thus a worse detection limit, since read out noise will dominate over dark noise. This is discussed further below.

6.2 Fauna monitoring

S-Lidar is able to continuously monitor aerial fauna activity along the laser transect. Insects that transit the beam are observed by the system as sparse backscattering signals in time and space. These observations can later be counted and their different properties can be extracted. The data may then be used to analyze movement or behavior of aerial fauna. In this section, some important considerations and concepts for aerial fauna monitoring using S-Lidar are described and discussed. This is followed by an account of the different field campaigns.

6.2.1 Optical cross section

The quantity optical cross section (OCS) is used to calibrate the insect size in this work; see Paper I and IV. This quantity is related to radar cross section (RCS), described in [33], although the collimated nature of the laser beam used in Lidar means that OCS is less dependent on range than RCS. Optical cross-section is the product of the cross section area of the organism, from the observation aspect of the Lidar, and its optical reflectivity.

The OCS, σ is related to detected intensity, I, at range, z, as:

$$\sigma(z) \propto I(z)z^2. \tag{6.2}$$

To calibrate signal intensity for an unknown object, I_{obs}, to OCS, σ_{obs}, the signal intensity, I_{ref}, from an object with a known OCS, σ_{ref}, and range, z_{ref}, must be recorded. The ratio of σ_{obs}, to σ_{ref} is:

$$\frac{\sigma_{obs}(z)}{\sigma_{ref}} = \frac{I_{obs}(z)/I_{st}(z)}{I_{ref}/I_{st}(z_{ref})}\frac{z^2}{z_{ref}^2}, \tag{6.3}$$

I_{st} is the static air signal from a homogenous atmosphere defined by the median signal over e.g. a 10-s time window. I_{obs} is the signal intensity above the static signal ($I_{obs} = I - I_{st}$). The signals are divided by the static air signal to compensate for difference in signal over range. When the laser termination is used as a reference; the signal intensity is equal to the static signal at the termination resulting in:

$$\sigma_{obs}(z) = \frac{\sigma_{term}}{z_{term}^2}\frac{z^2}{I_{st}(z)}\, I_{obs}(z). \tag{6.4}$$

It is important to point out that it is mainly the diffuse backscattering from an insect that will reflect its actual projected size, since the object used for reference is assumed to be diffuse. If the actual size of an insect is to be estimated, the diffuse and specular scattering should be separated, e.g. based on polarization properties. Since the OCS of an insect reflects its projected size, it will be different depending on the observation aspect (direction it is facing relative to the beam). This issue is discussed with respect to entomological Radar in e.g. [33,85] and more specific for Lidar in [21,86].

In the work described in this thesis, e.g. paper I and IV, the laser termination is used as reference [87]. In fact, this might not always be an ideal solution since the optical properties of the termination might change, for example when it gets wet. It is also difficult to determine what exact laser spot size that should be used for a correct calibration. Previously, white spheres and sticks with known optical properties have been dropped or put though the beam to enable size calibration. This method is often hard to use in practical settings since the horizontal beam is often located several meters above the ground, due to eye safety concerns. For vertical measurements it is even more complicated to do this.

6.2.2 System sensitivity

The sensitivity of an entomological Lidar system, i.e. the size of the smallest insect target that it is capable of detecting reliably, decreases with increasing range, owing to

the decline in collected signal from far distances. Small organisms, such as mosquitoes, are thus more likely to be detected at short ranges than at far ranges, and large organism are thus more readily detectable than small [87]; see illustration in Fig 6.3. The same kind of bias is seen in e.g. entomological radar measurements [33,88]. The bias affects the absolute number of detected insects at each time, but not the relative number over time at a specific range. If the activity at different ranges are to be compared this bias must be considered or compensated for. This could, for instance, be done by only considering observations with a size that is detectable at all ranges.

The other factor that affects the sensitivity is the optical background. Higher optical background level leads to a higher noise level and, as a result, lower sensitivity of the system. This means that smaller objects can be detected during the night than during the day, resulting in a change in the detected activity distribution over time. This must be taken into account when, for instance, the activity during day and night is compared.

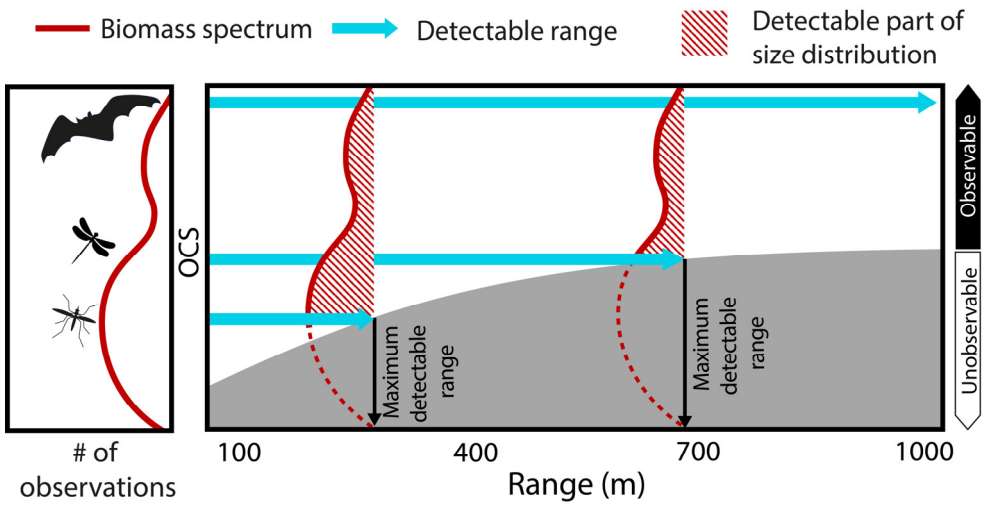

Figure 6.3. An illustration of how the lower detection limit of a S-Lidar system increases with increasing range. At short ranges, the activity of organisms of most sizes may be monitored but less and less of the biomass spectrum (organism size distribution) is detectable when the range increases.

6.2.3 Non-intrusive measurements

An important question to ask, when using S-Lidar for fauna monitoring, is whether the laser beam affects the behavior of the insects in some way, i.e. how non-intrusive is the technique? The primary concern would be if the light from the beam visually attracts or affects the animals. This is mainly an issue during night. Meanwhile, during the day, the radiation from the beam would be swamped by the high solar irradiance. However, even during low light conditions, insects should not be visually attracted to the beam

since the wavelength utilized, i.e. 808 nm, lies beyond the spectral range of their vision. Although many insects have a vision that covers a greater wavelength range than humans, it tends to extend into the UV wavelength range and not cover NIR or SWIR wavelengths [83,84].

Another possible way insects could be affected by the beam is that they experience the modulation frequency of the laser when the dark parts of their bodies absorb light. The reason for this is that an acoustic wave might be created during absorption, and this could conceivably be felt by an insect. Any real indication of insects systematically staying or turning around in the beam has not been observed. Most insects tend to transect fairly straight through the beam, indicating that they do not notice it, although there are exceptions. This fact could perhaps be investigated more systematically by analyzing the trajectory of a large amount of observations and see if there are indications of insects reacting to the beam.

An additional concern is whether the beam may harm the eyes of the insects. Most fauna pass through the beam very rapidly, typically within milliseconds, which limits the possible exposure time, and thus the risk of eye damage. The second argument against this is that the transmitted beam is eye safe, or almost eye safe, for humans. Since the compound eyes of insects have much smaller "pupils", i.e. apertures, than human eyes, much less power would be focused on their retinas and the risk of damage would be significantly smaller. The effect on flying vertebrates, such as bats or birds, is less clear, but to some extent the same logic could be applied since the animals pass through the beam very quickly, and many flying vertebrates, for example bats, have smaller eyes and worse light collection ability than humans [89]. Among both bats and bird there are exceptions to this though, and eye safety of animals is an important issue that should always be considered. Especially, if the laser power used in the Lidar system were to be increased or other wavelengths would be used.

6.2.4 Field campaigns

Several field campaigns aimed at *in situ* aerial fauna monitoring have been carried out during this work. They were carried out in Sweden, during summer time, and in tropical and subtropical places in Africa and Asia. Figure 6.4 displays an overview of the locations of these campaigns. Most of the campaigns took place during several consecutive days during which the system measured continuously. A horizontal laser transect has been used in most of the campaigns. exceptions being Östra Herrestad and part of the campaign in Yamoussoukro. An overview showing typical transects is presented in Fig. 6.5. These are the transects used during the field campaign in Guangzhou, where measurements above rice fields at different maturity level were carried out. Data from this campaign were used in the works presented in paper IV and in [22].

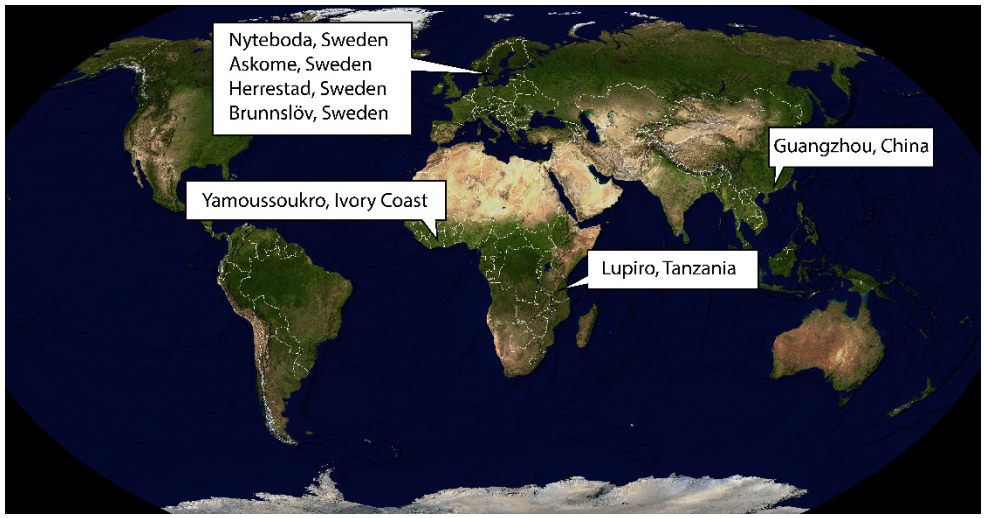

Figure 6.4. An overview of the different field campaigns for aerial fauna monitoring carried out during this PhD project.

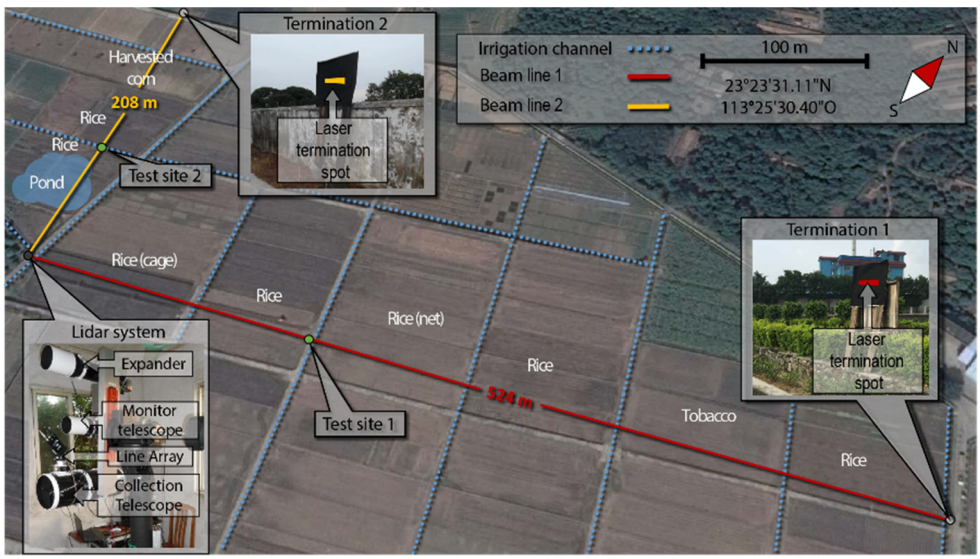

Figure 6.5. Horizontal beam transects during the measurement campaign in Guangzhou, China.

An overall goal of all the campaigns, especially the early ones, has been to test and evaluate the performance of the measurement system, but most of the campaigns also had more specific aims. During the Nyteboda campaign, a S-Lidar system was used to study the insect activity above a lake. Investigations of forest pests were also planned, but due to bad weather this aim was not reached. The goal of the campaign in Tanzania was to monitor malaria mosquitoes close to a village, with a high malaria incident rate. During the measurement campaign in China a polarimetric Lidar for entomological studies was employed [22]. Unfortunately, the overlap of the laser beams became misaligned and the polarimetric information could not reliably be matched on an individual level. Although, the measurements were primarily focused on rice pests, the interaction between insects, bats and birds (paper IV) was also investigated, since there was an abundance of these predators at the site. The field campaign in Yamoussoukro was part of a project to build and employ a S-Lidar system together with local PhD students, but the aim was also to study insects, particularly mosquitoes, in tropical regions.

The aim of the campaign in Askome and Östra Herrestad was to monitor insect activity around wind turbines to investigate possible reasons why the turbines kill bats. It has been shown that the deaths tend to occur at certain times of the year and during specific weather conditions (e.g. low wind); see [90,91]. One hypothesis why this occurs is that some types of insect that bats feed on gather around wind turbines at these weather conditions and the bats fly close to the turbines to forage. Some initial data from the field campaign carried out in Östra Herrestad, Sweden during August and September, 2018, are shown in Figure 6.6(a) as an example of the type of data that can be obtained with the system. The histogram shows the insect activity around the turbine over time from one of the warm evenings during this campaign (23 August, 2018) at different height intervals. The bat activity obtained from a sonar detector placed at the foot of the wind turbine is also shown in the figure. The temperature at the height of the turbine and the optical background is shown in Fig. 6.6(b), while a schematic of the position of laser transect and the Lidar system is shown in Fig.6.6(c). During this campaign, the measurement platform LUMBO (Lund University Mobile Biosphere Observatory) was used which, among other things, was built for S-Lidar monitoring of fauna [92]. By comparing the insect activity in time and space from nights displaying the specific weather conditions with nights that do not, possible pattern could be found [93].These patterns could help verify or falsify the theory that bats are attracted to wind turbines during certain weather conditions due to the insect activity around them at those times. The method at which observations are identified, extracted and analyzed to obtain e.g. this kind of activity plot is presented in the next section.

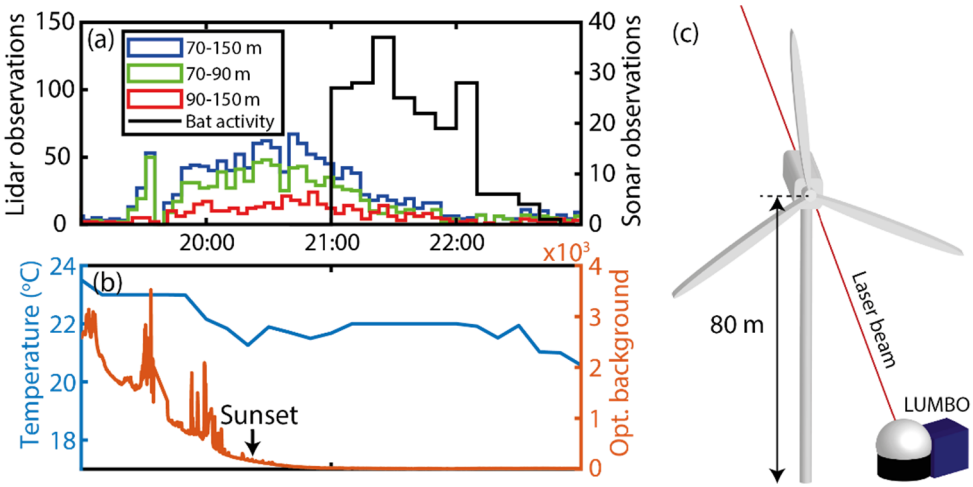

Figure 6.6. (a) Histogram of fauna activity at different height intervals nearby a wind turbine in Östra Herrestad, 23 Aug, 2018. The black curve connected to the right axis indicates the bat activity registered by a sonar detector placed at the foot of the wind turbine. (b) Temperature measured by a thermometer place on the turbine and optical background during the measurements. (c) A schematic of the laser transect during the measurements. The laser beam was placed behind the turbine to avoid the rotating blades.

6.3 Data analysis

A large amount of raw Lidar data (several terabytes) is collected during a measurement campaign over a couple of days when a kHz-sampling rate is used. To reduce the size of the data, the relevant sparse insect observations must be identified, extracted, and relevant parameters of each observation should be found. In this section, Lidar data acquired during a field campaign in Yamoussoukro, Ivory Coast in 2017 is used to exemplify the type of data obtained and to illustrate the main points of the data analysis. A flowchart illustrating these main points is shown in Fig. 6.7. A more detailed description of the evaluation may be found in Paper I.

6.3.1 Observation extraction

The data product obtained during a campaign consists of time-range files covering a typical time window of 10-20s. The data from one individual time-range file, recorded in Ivory Coast, is shown in a time-range map in Fig. 6.8(a) with an inset showing a closer view of a region with many sparse insect observations. The individual insect observations are identified and extracted using adaptive thresholding. The threshold at each range is set by using statistics over the time window in each file. This means, for

example, that if the background levels change over time the threshold will adapt to this. In the description of the evaluation method found in Paper I, it says that to set the threshold, the difference between the minimum and median values at each range, multiplied by the desired signal-to-noise ratio (SNR), should be added to the median signal level. Since then, our group has found that using the interquartile range, IQR, instead of the difference between the median and minimum gives a more robust threshold since it is less affected by outliers in the minimum value. IQR is a measure of variability, and is defined as the different between the first and third quartile of a distribution. The resulting threshold, as well as the maximum, median, and minimum signal for the file in Fig. 6.8(a), are shown in Fig. 6.8(b). The high activity level is revealed by the many peaks in the blue curve, i.e. the maximum signal curve.

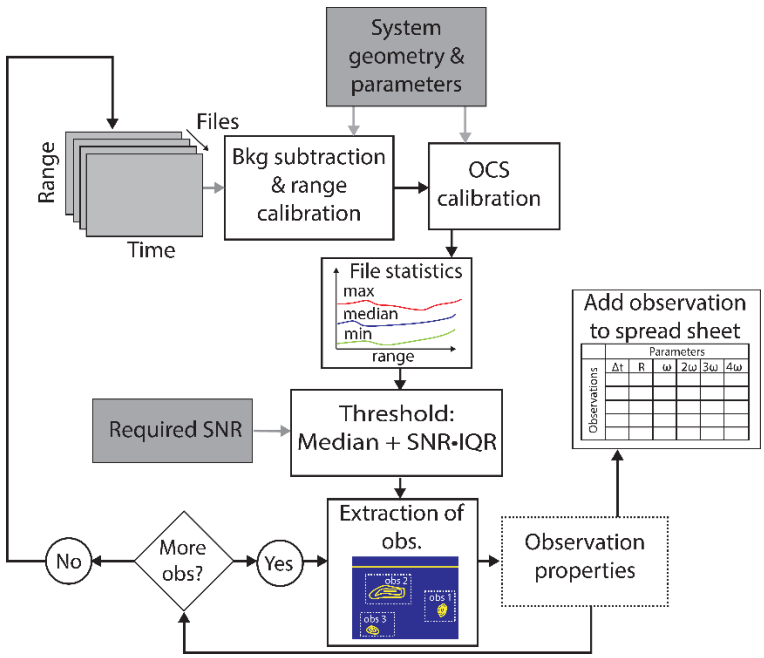

Figure 6.7. Flow chart of the data analysis. A time-range file is read and the background signal is subtracted. The signal is then calibrated to OCS. A threshold is set for each range using statistical data over the time-window of the file, and each observations with a signal above the threshold is extracted. Depending on the application, different properties are extracted from the observations, which then may be saved in a spreadsheet. When all observations have been extracted from the file, the next time-range file is read.

All adjacent pixels above the threshold are identified as an observation. Morphological image processing is used on the resulting binary map to ensure that adjacent pixels are linked and seen as one observation. The signal from each individual observation in a file is extracted and saved. When all observations in all files have been extracted, plots

of the general flight activity can be made. Figure 6.9(a) shows a histogram of the number of extracted observations over time for the data acquired in Ivory Coast in 2017. Figure 6.9(b) shows a 2D histogram of the peak activity at dusk. This type of plots gives an indication of the flight activity of organisms in time and space, e.g. it shows typical increase in activity at dawn and dusk. This activity should not be confused with population size or number of individuals since one individual organism may fly through the beam several times and thus give rise to more than one observation. Also, many individuals present do not cross the probe volume. The varying sensitivity of the system over range and time, discussed in section 6.2.2, will also affect the detected activity. Bias caused by the fact that the system has higher sensitivity at short ranges can be seen in the 2D histogram in Fig. 6.9(b), where the activity clearly peaks at short ranges.

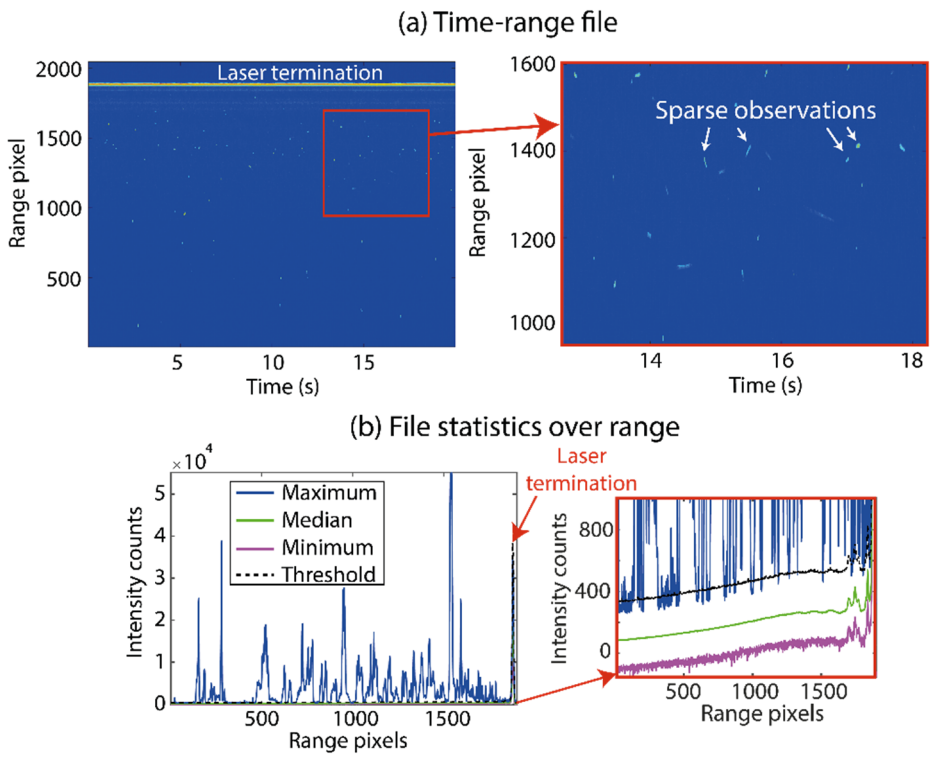

Figure 6.8. (a) A time-range map aquired at 18:07, 15 April 2017, in Yamoussoukro, Ivory Coast. A closer view of part of the map can be seen in the inset which clearly shows distinct sparse observations. The sampling rate was 875 Hz. (b) The corresponding maximum, median, and minimum for each range for the time window in (a), which are used to obtain the extraction threshold for the specific file. This threshold is also shown.

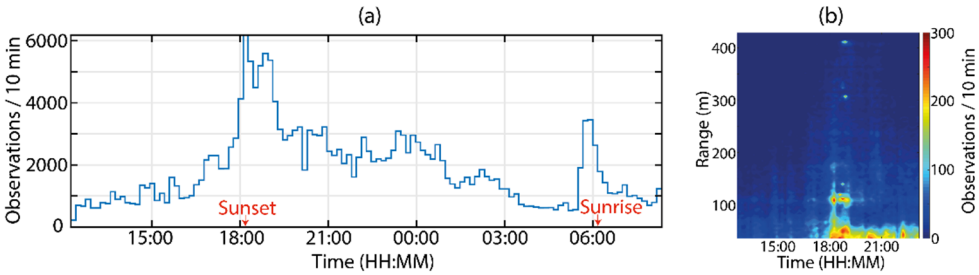

Figure 6.9. (a) Histogram of the number of extracted observations per 10 minutes from a part of the field campaign in Yamoussoukro, Ivory Coast, in 2017. The histogram shows data recorded between 12:20 on 15 April to 08:20 on 16 April. The typical increase in activity around dusk and dawn is clearly seen. (b) 2D histogram showing number of observation in time and space during the peak activity at dusk. The histogram shows clear peaks at certain ranges.

6.3.2 Parameterization

When an observation has been identified and extracted, different parameters specific to the observation may be found. The time-range maps of two extracted observations are shown in Fig 6.10(a) and Fig. 6.10(b). The observation shown Fig. 6.10(a) is from the Ivory Coast campaign and these data have not been calibrated to OCS, while the observation in Fig. 6.10(b), which is from a field campaign in Skåne, Sweden in 2013, has been calibrated. Which parameters that can be extracted from an observation depend on the properties of the Lidar system. A time series may be created by binning the signal across range, and from this time series, properties, such as body size and wing size, may be found. The frequency content of the wingbeats can also be ascertained if the sampling rate of the system is high enough to resolve it. The harmonic modulation spectrum of an insect has been proven valuable for classification and/or separation of insects of different species and sex [59,94–96]. Figure. 6.10(c)-(f) shows the resulting time series, as well as power spectra for the observations in Fig. 6.10(a) and Fig. 6.10(b).

If data are acquired with a polarimetric Lidar system, DoLP could be extracted, which gives information about the specular and diffuse properties of the signal. Furthermore, measurements with a system using multiple wavelengths could provide information about the degree of melanization. Information about these kind of properties could significantly improve the specificity of entomological Lidar measurements and enable separation of species that has similar wingbeat frequency, see e.g. [59].

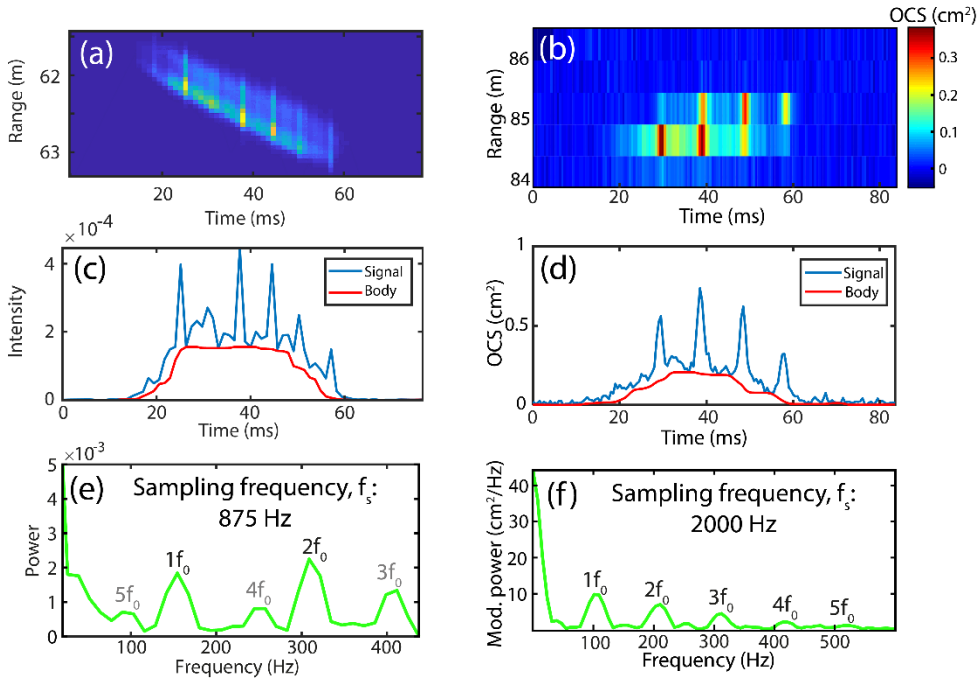

Figure 6.10. Time-range maps of an observation from the measurement campaign in (a) Yamoussoukro, Ivory Coast in 2017 and (b) Brunnslöv, Sweden, in 2013. (c)-(d), The time series obtained from the time-range maps. The blue plot shows the total signal and the red curve displays the non-oscillating body contribution. (e)-(f) The power spectra of the time series shown above. The different harmonics ($1f_0$, $2f_0$ etc) of the wing beats are marked in the power spectra. Due to the relatively low sampling frequency, the power spectrum in (e) display a frequency folding, i.e. frequency higher than half the sampling frequncy is folded back into the spectrum. The observation from the Brunnslöv data has been calibrated into OCS while the data from Yamoussoukro has not.

6.3.2.1 Harmonic frequency content

The frequency content of a signal from an insect contains information on properties such as wing size, body size, fundamental wingbeat frequency, and glossiness. To extract much of this information, the frequency content of the recorded signal has to be correctly identified. As discussed in Section 2.2.1, the backscattering time signal from an insect consists of a body component, $I_{body}(t)$, and an oscillating wing components, $I_{wing}(t)$, see time series in Fig. 6.10(c) and (d). These time signals may be separated in post processing using a sliding minimum filter. The length of the filter should correspond approximately to the period of the wingbeat oscillations. A filter length that is too short results in a time series for the body contribution that also contains wing oscillations, while a filter that is too long cannot resolve the flanks of the

body contribution properly. When the signals have been separated, the oscillating time signal from an insect may be described using a set of harmonic basis functions:

$$\psi_{even}(t,k) = cos(2\pi k f_0 t), \qquad k = 0,1,2,\ldots \tag{6.5}$$

$$\psi_{odd}(t,k) = sin(2\pi k f_0 t), \qquad k = 0,1,2,\ldots \tag{6.6}$$

Where f_0 is the fundamental frequency and t is time. These are then used to form a trigonometric Fourier series that estimates I_{wing}, using harmonics up to the Nyquist limit ($f_s/2$):

$$\hat{I}_{wing}(t) = \hat{I}(t)_{body}\left(a(0) + \sum_{k=1}^{<f_s/2f_0} a(k)\psi_{even}(t,k) + b(k)\psi_{odd}(t,k)\right). \tag{6.7}$$

Here, f_s is the sampling frequency. The harmonics describing the signal from the wings is weighted with the body contribution since there are no wings present if the body is not in the beam. This weighting separates observation artifacts from intrinsic insect properties. It excludes DC and harmonic side-lobes and cancels out artifacts from the shape of the beam profile. The coefficients, $a(k)$ and $b(k)$, correspond to the absolute strength and phase of the harmonics in $\hat{I}_{wing}(t)$. These are found by solving a system of linear equations with a least-squares estimation:

$$a(k) = \left(\psi_{even}^T(t,k)\psi_{even}(t,k)\right)^{-1}\psi_{even}^T(t,k)I_{wing}, \tag{6.8}$$

$$b(k) = \left(\psi_{odd}^T(t,k)\psi_{odd}(t,k)\right)^{-1}\psi_{odd}^T(t,k)I_{wing}. \tag{6.9}$$

The total backscattering signal may then be reconstructed:

$$I_{tot}(t) = \hat{I}(t)_{body} + \hat{I}(t)_{wings}. \tag{6.10}$$

In paper I, this parameterization method was used in combination with a sum-of-squares residual fit to determine fundamental frequency. This method requires a good initial guess of the fundamental frequency, f_0, which is not a trivial problem. Artifacts, such as side lobes, caused by the top-hat profile of the beam, make it hard to identify the fundamental frequency in a continuous power spectrum. Using the strength of the harmonics is not a reliable method either, since the fundamental frequency is not necessarily the strongest harmonic, as can be seen in Fig. 6.10(e). Using the spacing between harmonics in a power spectrum may therefore be a more robust way to guess the fundamental frequency, than just using the strengths of the harmonics. Although, this method also has its problems since the exact positions of the harmonics are sometimes hard to identify.

An alternative to guessing the fundamental tone is to include the whole possible frequency interval in the residual sum-of-squares fit. The problem with this method is that it leads to overfitting. Low frequencies will result in many degrees of freedom (DoF) and they would thus always be chosen over higher frequencies since an increase in the number of parameters in a model always improve the goodness of the fit. In fact, if the DoF becomes the same as the number of data points the model will become a transform and have perfect goodness of fit. There are methods, such as Akaike information criterion [97], that punishes a model for overfitting. The issue with using such an estimator is that the method used to extract the harmonic content is not merely a sum-of-square fit. The test frequencies are not only used to create the harmonic functions describing the wingbeats, but also to define the filter size used when the body contribution is estimated. In this estimation, high frequency will result in a small window size, and a smaller window size means that the body contribution will describe more of the total signal. If the window gets small enough the body contribution will describe the total signal, including the oscillating parts. This results in a strong bias towards high frequencies.

A method which is attempting to deal with both these issues simultaneously has been developed in our group [98]. It performs a residual sum-of-squares fit on the wingbeat signal which is then divided by an analytical curve meant to compensate for the increasing DoF in the regressor (Eq. 6.7). This curve is attained by using observation properties such as transit time. The fit is then divided by a sum-of-squares residual fit of only the body contribution, as a way to deal with the filter size issue. This method has not yet been properly evaluated.

Another issue that further complicates the identification of the fundamental frequency is under-sampling. Harmonics which fall above the Nyquist frequency ($f_S/2$) will be folded back into the power spectrum resulting in peaks at incorrect frequency positions. This phenomenon can be seen in the power spectrum in Fig. 6.10(e) since the sampling rate used when these data were collected was relatively low, i.e. 875 Hz. The 3rd, 4th and 5th harmonics have been folded into the power spectrum. The observation in Fig. 6.10(f) does not exhibit this problem, even though the fundamental tone is not that different. This is due to the higher sampling rate used during these measurements (2000 Hz).

6.4 Dark field spectroscopy and Passive Lidar

Dark-field spectroscopy is a simple, yet powerful, method for optical monitoring of insects [99] which has also been used during this PhD project. It utilizes the natural sunlight, instead of laser light, which results in a much lower experimental complexity. A schematic view of a dark-field setup is displayed in Fig 6.11. A telescope is directed towards a distant black cavity and when an insect crosses the FoV of the telescope, the

sunlight backscattered off the insects is detected with close to zero background. A simple photodiode, allowing kHz sampling rates, may be utilized as detector in this technique. If a quadrant photodiode is used, information about the flight direction of the insect may be obtain; see Fig. 6.12. Multispectral information about the backscattering is also readily extracted by replacing the photodiode with e.g. a spectrograph equipped with a fast detector system, a sandwiched photodiode [100] or several different photodiodes sensitive in different wavelength regions [66]

One of the main drawbacks with the method is that it can only be used during daytime when there is direct sunshine. Range resolution is not directly obtained with this method either, although work has been done to develop a data analysis method to extract range information. This method has been called "Passive Lidar" [101]. The method is based on the fact that the overlaps of the FoVs of the quadrants is not the same at different ranges. At close ranges the overlap is substantial, while they are fully separated at the black cavity, where the focus of the quadrant photodiode is located. The signal of an insect transecting the FoVs will reflect this and range information can thus be extracted.

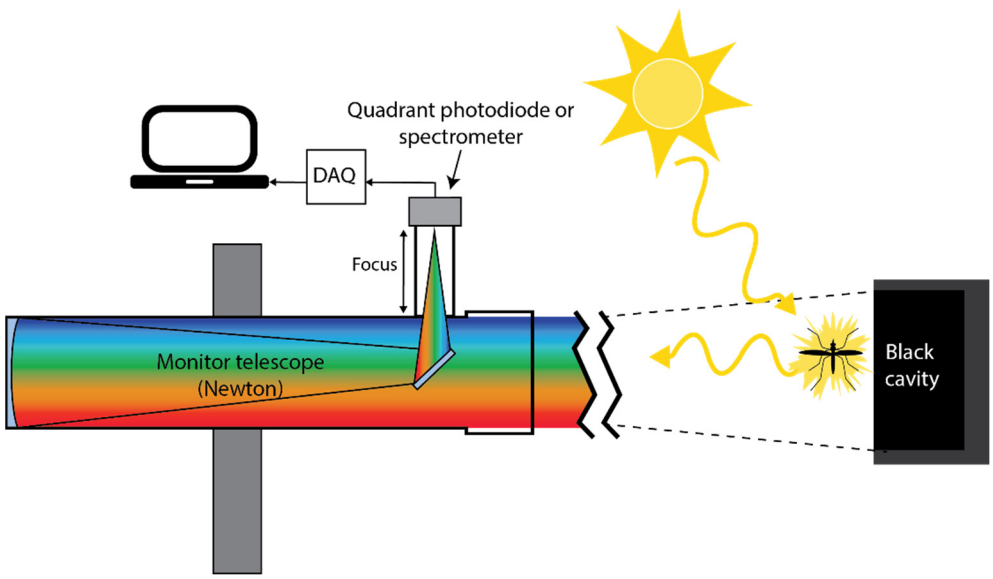

Figure 6.11. A schematic illustration of the dark field spectroscopy concept. The sunlight scattered off insects are collected on a dark background using a telescope. The signal is detected by a quadrant photodiode. Due to the broad spectral content of the scattered sunlight, it is possible to obtain spectral information about the insects if the signal is dispersed using e.g. a spectrometer

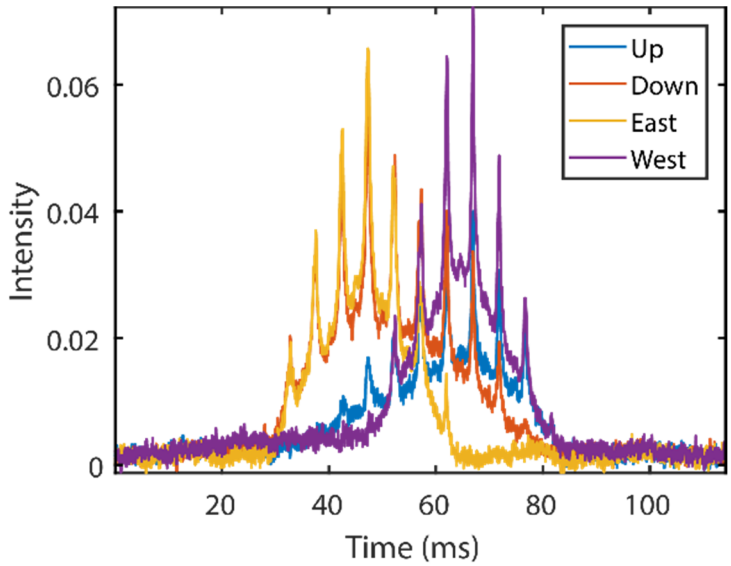

Figure 6.12. Signal from an insect flying through the FoV during a darkfield measurement at Stensoffa field station in Sweden.The signal from the insect is first visible in the quadrants covering the east and lower parts of the FoV, and later in the quadrants monitoring the western and upper part. This means that the insect trajectory is east-west, down-up. The nature of the overlaps between the quandrants are utilized in the method called Passive Lidar. The evaluated range for this observation is 68 m.

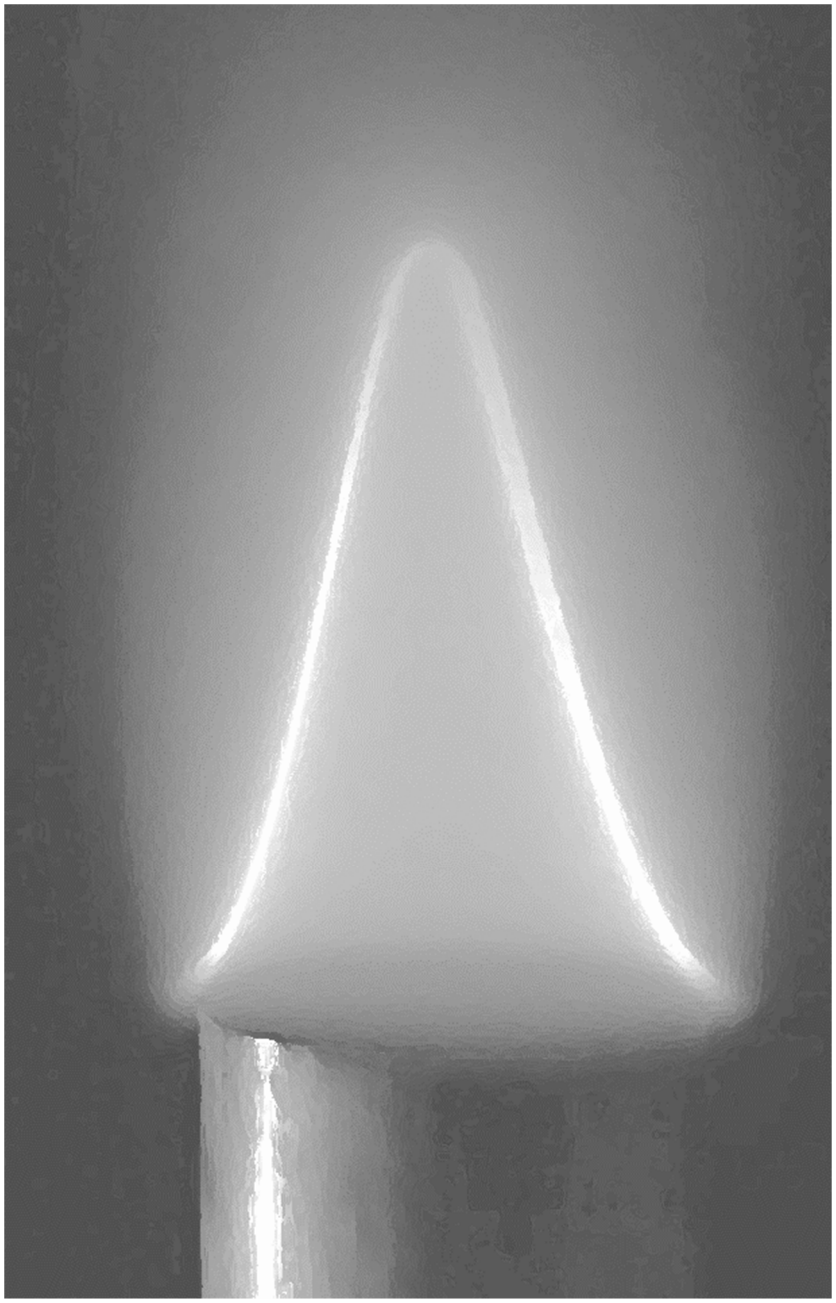

Chapter 7

Combustion diagnostics

The S-Lidar systems used over short ranges are described in this section as well as some of their applications. Most of the work has been focused on developing methods for combustion diagnostics (see Paper V, VI and parts of Paper III) over several meters, but an application for aquatic Lidar is also described at the end.

7.1 Flame studies

In principle, three different experimental configurations have been used for combustion diagnostics. A general schematic figure of the short range system is shown in Fig. 7.1(a) and the three different versions of the system are displayed in Fig. 7.1 (b)-(d). The main differences between the setups are the type of laser and detector used in each case. The perpendicular distance between the laser beam and detector (baseline) is around 20-22 cm for all cases.

7.1.1 Elastic measurements

The first configuration, seen in Fig. 7.1(b) is more or less a down-scaled version of the setup used for aerial fauna monitoring. It uses a multimode LD with a linewidth on the order of nanometers. The beam is expanded and transmitted by a lens or an objective. The laser output is modulated in synchronization with the exposure of the line-array detector using a counter. During one exposure the laser is on and during the next it is off, giving alternately the signal of interested and a background signal. A bandpass filter is placed in front of the line-array detector to suppress background light. The lasers have output powers ranging from 0.5 to 3 W and an emission wavelength of approximately 405 nm or 445 nm. A photograph of the system is shown in Fig. 7.2.

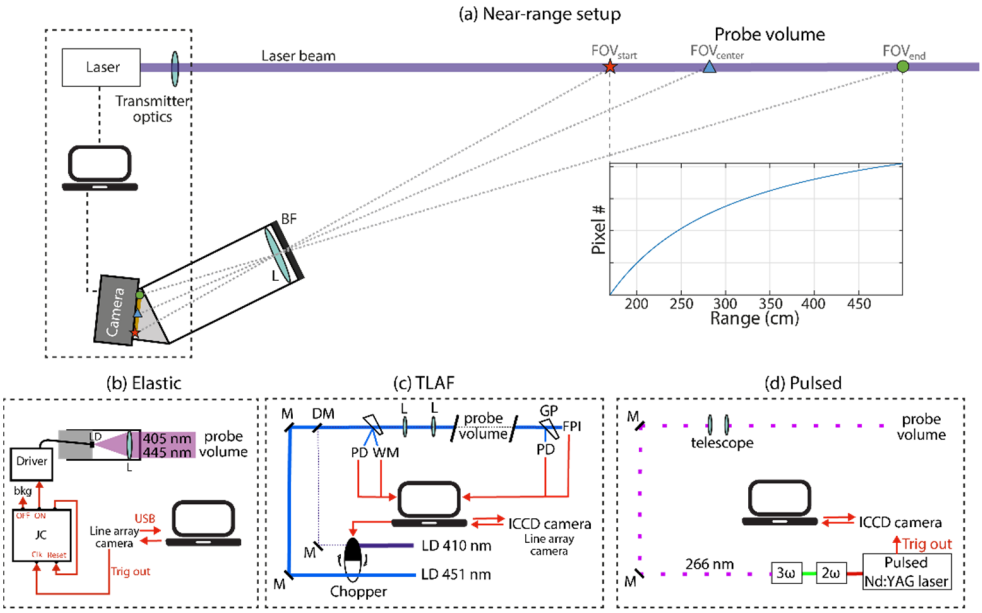

Figure 7.1. (a) Overview of the short-range setup used for combustion diagnostics. The setup has been used in three main configurations. The first one, seen in panel (b), is similar to the far-range systems presented previously. It uses a multimode diode laser beam modulated using a counter and a line-array camera. The second configuration, (c), uses two single-mode diode lasers. The laser output is modulated using a chopper and both a line-array camera and an ICCD camera is used to detect the signal. This configuration was used for TLAF thermometry. In the configuration in (d), a pulsed Nd:YAG laser and an ICCD camera are used.

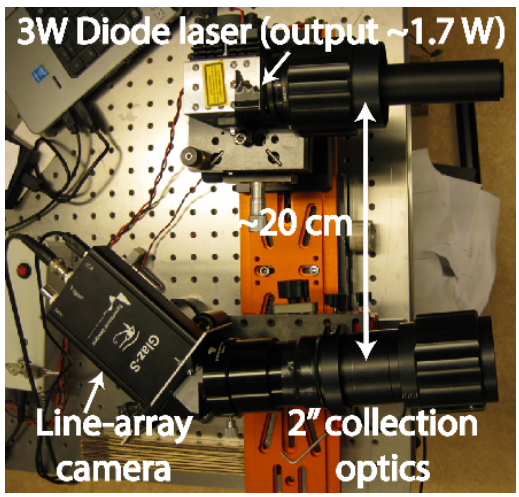

Figure 7.2. Picture of the initial small-scale system used for elastic measurments in flames.

The setup was used to perform initial elastic measurements on smoke and in highly scattering flames to demonstrate the ability of the method to provide temporally and spatially resolved measurements over a couple of meters. Exemplifying results from such measurements are is shown in Fig. 7.3(a) and 7.3(b). This system was also used to perform Rayleigh thermometry in a flat methane/air flame. Since the recorded signal are proportional to the molecular number density, it is possible to determine temperature using Eq. 2.4. Figure 7.3(c) shows Rayleigh signals as well as the corresponding evaluated temperatures. The temperatures are somewhat under-predicted. The reason for this is stray light interference which all Rayleigh-scattering thermometry diagnostics is inherently sensitive to [102]. The stray light may be a result of dust particles in the laser transect as well as light scattered off surrounding objects. The latter problem is often a result of diffraction due to the transmitter optics and aperture. This issue was hard to mitigate for the laser diodes utilized in this setup, especially if the beam size had to be kept small.

During the early tests performed with this setup the importance of keeping the beam narrow was discovered. A rather large aperture size of 2-3 cm was used initially, resulting in a wide beam. This resulted in quite a large degradation of the spatial resolution. Thus, the beam had to be focused at the point of interest if high resolution was needed. It was concluded that a narrower beam would be more suitable for the intended applications. This conclusion was later confirmed by the raytracing simulations (see section 4.2.2).

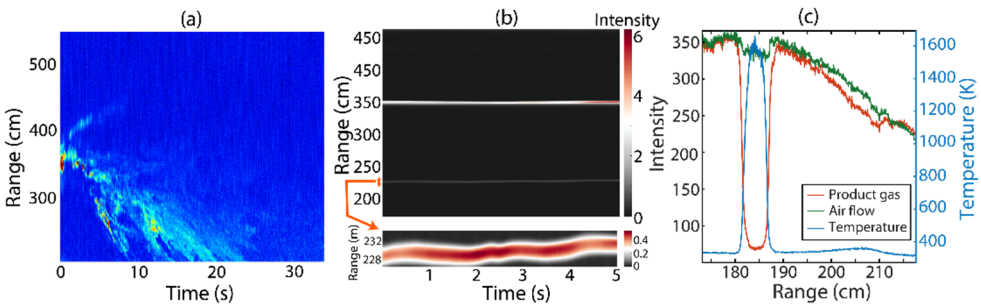

Figure 7.3. Elastic measurements. (a) Time range map of smoke dispersing along the laser beam. The effective sampling rate was 100 Hz (b) Signals from two sooty flames placed in the laser transect at different ranges. The inset at the bottom shows flickering of one of the flames. The effective sampling rate was 2000 Hz. (c) Rayleigh scattering signal from air and with a flat methane/air flame placed in the laser transect. The ratio of the signals are used to extract Rayleigh temperatures (right axis).

7.1.2 TLAF

Laser-induced fluorescence is an important tool in combustion diagnostics, since it is a very sensitive and highly species-specific method. One of the main reasons why the S-Lidar concept has been investigated for combustion diagnostics is that it is difficult to obtain adequate spatial resolution with LIF in conventional ToF-Lidar [48]. The first demonstration of LIF measurements in a flame with S-Lidar was done in a flat flame seeded with indium atoms, see Fig. 7.4(a). Indium atoms give rise to intense fluorescence, thus making this atomic species ideal for an initial demonstration

After range-resolved fluorescence detection had been demonstrated, the S-Lidar technique was combined with the TLAF thermometric method to measure flame temperatures, see paper VI. In TLAF thermometry [55,56], temperature is extracted from the ratio between the fluorescence signals resulting upon excitation with two different wavelengths. The setup used may be seen in Fig. 7.1(c). The beams from two single-mode diode lasers, emitting at 410 nm and 451 nm, respectively, were spatially overlapped using a dichroic mirror, and transmitted towards the flame using a telescope. The laser outputs were alternated using a mechanical chopper, synchronized with the camera exposures. Two photodiodes and a wavemeter were used to continuously track the laser power and wavelength, in order to calibrate the recorded data. Flame measurements were performed both with a line-array camera and an ICCD camera. An example of recorded fluorescence signals is shown in Fig. 7.4(b) and the temperature profile evaluated from the ratio of the two signals is shown in Fig. 7.4(c). Average temperatures in the center of the flame at different heights above the burner (HAB) are shown in Fig. 7.5, for four different measurement series.

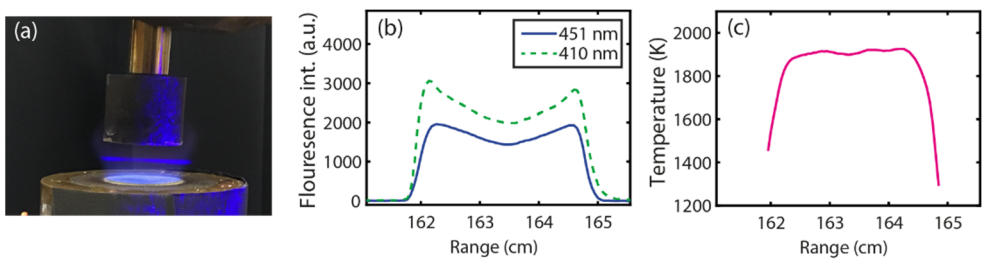

Figure 7.4. (a) Photograph of a flat flame on a porous plug burner seeded with indum salt solution. The blue line across the flame is the laser-induced indium fluorescence. (b) Indium fluorescence signals emitted at 451 nm, with excitation wavelegnth 410 nm (green, dotted line) and 451 nm (blue, solid line). (c) Temperatures evaluated from the ratio of the two signals in (b).

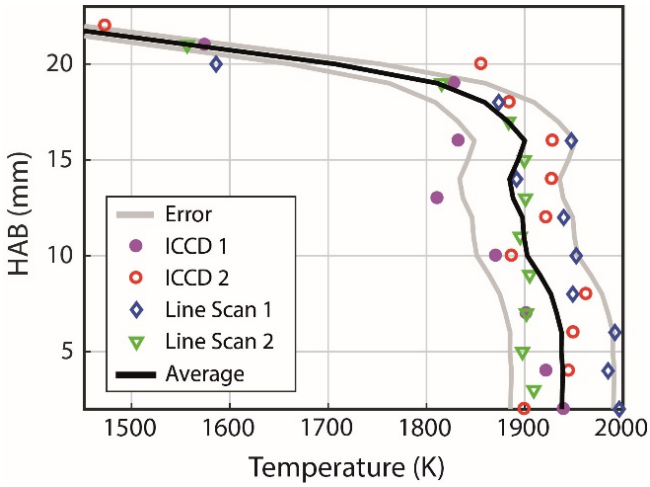

Figure 7.5. Temperatures at different HAB for four different measurement series. Two different detectors were used (ICCD and line scan). The gray lines show the estimated measurement error of 2.7% of the TLAF technique at flame temperatures A linear interpolation between the different HABs was performed for each series of measurements, and the solid black line displays the average of these interpolations.

7.1.3 Pulsed S-Lidar

The S-Lidar concept is not restricted to CW-lasers, but it can equally well be based on pulsed lasers. In fact, a pulsed laser source together with a gated ICCD camera might be the best setup for many combustion experiments, particularly when strong background radiation is anticipated. The main aim of these initial measurements was to test the feasibility of S-Lidar based on pulsed lasers. The third harmonic (355 nm) emission of a pulsed Nd:YAG laser was used to obtain Rayleigh scattering signal as well as LIF signals from a naturally occurring flame species, namely formaldehyde (CH2O). A gated ICCD camera was used to detect the signal. A bandpass filter with a center wavelength of 355 nm was used in front of the camera during the Rayleigh scattering measurements, while a notch filter, with a maximum rejection (OD4) at 355 nm, was used to remove the scattered laser light in the formaldehyde fluorescence measurements. The setup is schematically depicted in Fig. 7.1(d). A conical Bunsen flame with a width of ~1 cm was placed in the laser transect. The focus of the laser beam was placed in the center of the flame giving high resolution there. The recorded Rayleigh scattering profile is shown in Fig. 7.6(a), while the formaldehyde fluorescence signal from the same flame is shown in Fig. 7.6(b). The resolution was high enough to discern the two distinct fluorescence peaks originating from the pre-heat zone of the conical Bunsen flame. Figure 7.6(c) shows formaldehyde fluorescence signal recorded with a collimated beam transecting two Bunsen flames placed at different positions along the laser transect.

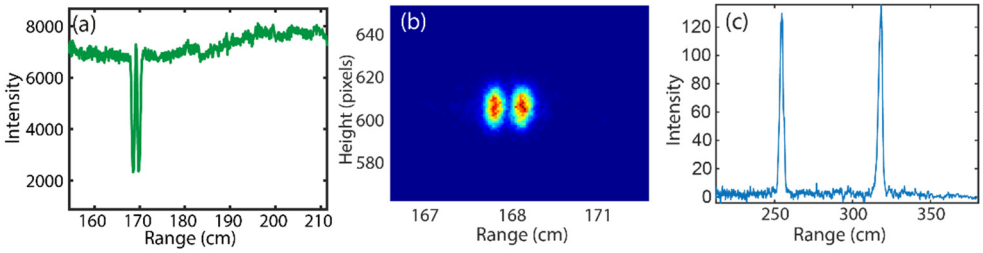

Figure 7.6. (a) Rayleigh scattering signal recorded using a pulsed laser with a Bunsen flame placed at a range of 168 cm. (b) 2D image of formaldehyde fluorescence from the same flame. The resolution was high enough with this configuration to observe the two distinct fluorescence peaks originating from the pre-heat zone of the conical bunsen flame. (c) Fluorescence signal from two Bunsen flames placed at different positions along the laser transect.

7.1.4 Optical access and spatial resolution

Combustion diagnostics in industrial facilities is often limited by the location and size of the optical access. An important factor to consider when using S-Lidar in such applications is thus the actual distance between the laser transmitter and the receiver (the baseline shown in Fig. 7.1 as well as Fig 7.2), since this determines the required size of the optical access. This distance is, in turn, dependent on the focal length of the receiver as well as the detector tilt. A longer f_{rec} will result in a higher range resolution, but also a longer baseline and vice versa. A larger detector tilt will give a shorter baseline, but the resolution will then decrease. The intended measurement task and the extent of the measurement object should thus be considered when choosing f_{rec}. To cover a large range interval with high resolution, a large focal length, and therefore also a large optical access, is needed. If the optical access is small, a shorter focal length may be used at the expense of either covered range interval or resolution.

To make the required optical access smaller it is also possible to place the system at a distance from the optical access, for instance at the same distance as the minimum detectable range. The size of the detector chip as well as the size of the pixels may also be altered to change the resolution and the covered range interval.

7.2 Multispectral system

A short-range system providing spectral resolution has also been built. It has the same scale as those used for combustion diagnostics. The system used to investigate the potential of multi- or hyperspectral monitoring of aquatic fauna, as discussed in Paper II, although other potential applications could be e.g. combustion diagnostics. The setup is shown in Fig. 7.7.

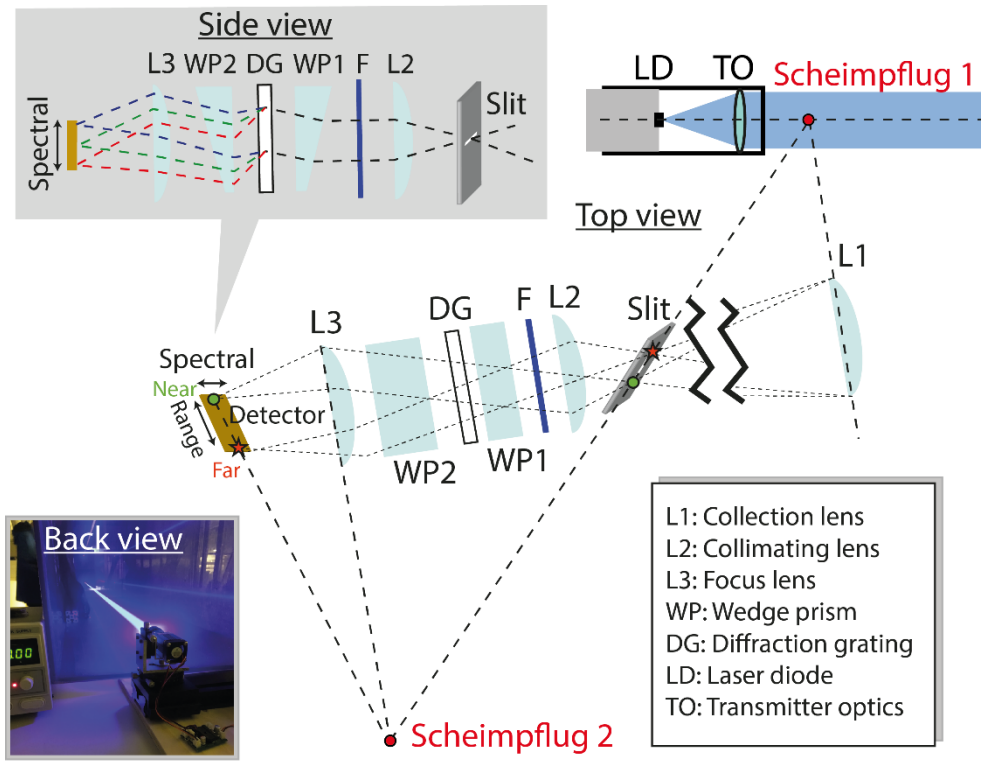

Figure 7.7. A multispectral, short range S-lidar system. Spectral resolution is gained by imaging the backscattered laser light onto a slit placed in Scheimpflug configuration, and then using a PGP configuration to disperse the light. The dispersed light is then imaged onto a 2D detector placed in another Scheimpflug configuration with the slit and the focusing lens. Spatial information is thus attain along one direction on the 2D chip, while spectral information is attained along the other, perpendicular direction. An image of the laser beam transmitted into a 5-meter long water tank is shown in the lower left corner.

Just like in the previously described S-Lidar setup, the laser beam and the receiver are placed in a Scheimpflug configuration, but the line-array detector chip is now replaced by a 100 µm wide slit. The light is thus sharply imaged onto the slit. To gain spectral information, the light is dispersed perpendicular to the length of the slit by a prism-grating-prism (PGP) configuration [103], consisting of a transmission grating with 300 grooves per mm in between two wedge prisms. To sharply image the dispersed light onto a 2D detector, a second lens is placed in an additional Scheimpflug configuration with the slit and the detector. Range resolution is thus attained along the direction parallel to the slit, according to the Scheimpflug and hinge conditions, while spectral resolution, over the spectral range 430-700 nm, is provided along the perpendicular direction. More details about the system are found in Paper II. Multispectral systems inspired by this have recently built for vegetation monitoring from a drone and oil spill monitoring [104,105].

The system was used in a 5-meter long water tank, detecting elastic and Raman scattering signals from water, as well as elastic scattering and fluorescence from chlorophyll in algae and zooplankton (*Daphnias magna*) labelled with fluorescent dye.

Chapter 8

Discussion, conclusions and outlook

This chapter is divided into two main sections; fauna monitoring and combustion applications. Each part presents and discusses the major conclusions and accomplishments resulting from the project, as well as future outlooks.

8.1 Aerial fauna monitoring

During this PhD project, the Scheimpflug-Lidar method has been developed and applied for practical aerial fauna monitoring in the field. A large part of the project has also been to use and improve the evaluation method for Lidar data. In recent years, our research group has built and employed several different S-Lidar systems. These systems have been utilized in different field campaigns around the world and from the acquired data, hundreds of thousands of insect observations have been identified and extracted. One of the main conclusions drawn from this project is that S-Lidar has the ability to efficiently monitor insect activity along a laser transect. The equipment is small and robust enough to be transported to and assembled at remote field sites, such as the Tanzanian countryside. Its ability to detect tens of thousands of insect observations per hour per cubic meter with range resolution, *in situ*, makes it a tool that can provide biologists and ecologists with data they could never attain from traps or sweep nets.

Most of the data presented in this thesis were obtained using an S-Lidar system with one laser source but the ability to obtain polarimetric insect data from a system using two laser sources delivering light with different polarizations has also been demonstrated. The method has been used in collaboration with biologists to investigate biological phenomena. Using data acquired in Guangzhou, China, the interaction between insects, bats and birds above rice fields have been investigated. As discussed in Paper IV, the obtained activity data show that the temporal peaks of observations with large optical size and observations with small optical size occur with an off-set during twilight, possibly indicating a prey-predator avoidance behavior. The method has also

recently been used to monitor insect activity close to a wind turbine. This project aims at finding a possible reason why wind turbines kill bats during certain times of the year, under specific weather conditions. There are also ongoing projects meant to investigate the behavior and movement of malaria mosquitoes close to a Tanzanian village. Such knowledge could hopefully aid the ongoing efforts to limit the spread of Malaria and thus help save many lives.

Since the investigation of prey-predator interaction, carried out in China was an initial study, it would be very interesting to return to the same field site or a similar site in a tropical region and record data during a larger amount of days. A more stringent manual inventory of birds and their activity could then be done and bat detectors e.g. based on sonar detection, could be used. This data could then be correlated with the Lidar measurements and it would also enable species determination of the bats. To improve the accuracy of the size discrimination, a more systematic size calibration could be performed, e.g. by placing targets with well-known optical size at different ranges in the beam.

Another interesting study would be to perform entomological S-Lidar measurements and entomological radar measurements simultaneously. The techniques could then be properly compared and their advantages and disadvantages could be shown experimentally. This might possibly lead to insights about how the two techniques can complement each other to gain more information about flying fauna.

Sometimes it has been hard for our research group to develop, adapt and apply the S-Lidar method to real biological questions, since the group currently consists of physicists and engineers, none of which are experts on biology or ecology. We have been fortunate to collaborate with people who do have this knowledge, but in the future it would be very advantageous to have PhD students or post graduates with biology backgrounds working in or very closely with the group. Individuals with this background, who also have knowledge of the equipment, would be a great resource for the development and implementation of the technique in different biological fields. In particular, they could facilitate the planning and execution of field experiments and thus improve the chance of retrieving relevant biological data.

The S-Lidar technique is able to detect and monitor most of the living constituents of the atmosphere, but the real challenge for the technique lies in discriminating between different groups of insects. Extracting the correct parameters from the data and using those parameters to separate different insects are not trivial tasks. Many properties are affected by circumstantial and environmental factors such as observation direction, temperature, and humidity. The ability to confidently separate between e.g. species of insects, would greatly increase the method's impact, both for biological research and possible commercial applications.

One way of increasing the specificity of Lidar measurements could be to increase the number of parameters that can be extracted from the data. A possible approach is to use multispectral or polarimetric Lidar systems [22]. The data obtained may then provide information about depolarization ratio or melanization [59,66], which report

on glossiness and microstructures in body or wings. Dual or multiband S-Lidar has been demonstrated in Lund previously for particle detection [25,26,106] and similar systems could be implemented for fauna monitoring. The main drawback of using several laser outputs is, beside increased complexity, that the effective sampling rate will decrease somewhat. However, this can easily be solved by using a faster detector, and possibly higher laser power.

Another alternative is to use a laser source that transmits light with a broad spectrum, e.g. a supercontinuum laser, and a fast detection system able to spectrally resolve the signal. For instance, a PGP setup similar to the hyperspectral Lidar presented in section 7.2 could be used. This kind of setup may deliver spectral information from the insects transecting the beam, revealing their colors and surface structures. With a multi-or hyper spectral system, the spectral fringes contained in one specular reflection of white light off insect wings may be resolved and the thickness of the wing membrane could be extracted. Due to their highly directional nature, specular reflections also do not suffer from the $1/z^2$ dependence of the signal intensity, like diffuse scattering do. This means that they can be detected at further distances than diffuse reflections. One of the main advantages of spectral information is that it is much less dependent on transit time than e.g. information about wingbeat frequency. Wingbeat frequency and properties related to this can only extracted from a signal if the insect stays in the beam long enough to beat its wing several times. This is not the case for spectral data, which could give a unique spectral signature to each observations, including very short ones. If the transit time becomes less important it would also be possible to make the beam smaller and thus increasing the power density of the beam.

Using a detector able to spectrally resolve the signal could also enable measurements where some insects have been tagged with e.g. fluorescent dye [99,107]. A signal from the tagged insects will always be identifiable since the fluorescence signal will be spectrally separated from the elastic signals from untagged insects. This data could simply be used to study the behavior of the tagged insects, or be used to identify non-tagged individuals of the same species. It could also be utilized to correct data for multiple observations caused by the same individual. If, for instance, 100 individuals are released, and 300 observations are detected during a day of measurements, all the activity data could be divided by 3 to better relate it to population size.

One possible way to improve the identification and separation of signals from different groups of insects, is to use a machine learning approach. Parameters extracted from insect signals, or simply the entire signals, could be used as input for an algorithm that learns how to divide them into different groups. This could be done by the algorithm either by referencing and generalizing available classified training data (supervised), or by just finding structures in the data and grouping observations accordingly (unsupervised). A supervised machine learning method is often able to provide more detailed results than an unsupervised one but the tricky part is to procure training data for the algorithm. It is not certain that signals recorded in the laboratory

are directly applicable to signals acquired in the field, and obtaining enough data in a field environment, e.g. through control releases, is difficult.

8.2 Combustion diagnostics

Several versions of a short range Lidar system have been built in this work. These have been used to evaluate and demonstrate applications of the S-Lidar technique in combustion diagnostics.

One of the main conclusions drawn from this work is that S-Lidar is a tool able to provide remote range-resolved information about combustion environments in a laboratory environment, indicating that it would be a versatile tool for diagnostics in large-scale combustion facilities. The fact that a S-Lidar system does not have to rely on large, high-power pulsed lasers means that the system can be made small and portable, which is ideal for industrial applications. Since the technique collects signal in the backward direction it only requires one optical access. The required size of this optical access would depend on the configuration and optics of the system. In general, a larger optical access allows a system that provides higher resolution over longer range intervals, while the opposite is true for a small optical access. In general, the design of the S-Lidar system should be chosen according to the specific application. This is especially true for the shape and width of the laser beam since it affects the resolution.

In the work presented in this thesis, range-resolved elastic measurements in highly scattering environments, such as smoke and candle flames, have been demonstrated qualitatively. Rayleigh scattering in flames have been investigated and quantitative temperatures have been extracted. The technique has also been demonstrated for qualitative detection of fluorescence in combustion applications using a flame seeded with indium atoms, and quantitative remote thermometry has been carried out in the same flame using TLAF. S-Lidar using pulsed lasers has also been tested and qualitative scattering measurements and detection of fluorescence from formaldehyde, a naturally occurring flame radical, have also been demonstrated.

It is difficult to create an extended combustion environment in a normal laboratory due to safety concerns, and it is especially difficult if the properties of the combustion environment are to be well-known. Therefore, the combustion applications have instead been demonstrated by placing individual flames at different positions in the laser beam. This kind of approach often leads to a discussion about the techniques' ability, or inability, to provide the same resolution of the flame zones as conventional diagnostic techniques do. This discussion indicates that measuring on individual flames does not fully highlight the strength of the Lidar technique, namely the fact that it may provide range resolved measurements over much longer distances than conventional techniques. The technique is not meant to compete with conventional diagnostics, but it is rather a tool that should be used when conventional methods are not applicable.

To show this, and evaluate the strength of the method, measurements should be carried out in a larger combustion facility, where a controlled continuous combustion environment can be established. This should then be followed by measurement campaigns at real industrial sites.

Though the detection of particle distribution has only been demonstrated here and not fully investigated, the application is well-suited for the technique. The typically high elastic scattering signals from particles enables the use of high sampling rates and the technique would provide temporally and spatially resolved information about particle distributions. Information like this could not only be useful in combustion studies, but also at non-combustion based industrial sites. An example is industries where the production results in suspended particles, which could constitute a health problem for employees.

If two, or several, displaced beams are used in an S-Lidar setup, both the particle distribution and its movement may be determined. The displaced laser beam would be alternated between in synchronization with the fast camera exposures. By time correlating the signals in the different time slots, corresponding to different spatial positions, it would thus be possible to determine the direction of the movement and thus get flow data. This is similar to how the dark-field signals shown in Fig. 6.12 gives information about flight direction, except that the displacement in space is made with the laser beams and not on the detector side.

S-Lidar based on pulsed lasers might lose some of its advantages of using small and portable lasers equipment but it gains the ability to use fast time gating. This is a huge advantage in environments with very strong background emission, since the combination of a short laser pulse and a short camera gate allows very efficient background suppression. One of the initial aims of the pulsed measurements, presented in section 7.1.3, was to use time-gating to remove interfering signal from a strong termination echo, which would be inevitable for industrial applications. This termination echo is especially a problem in Lidar since the detection occurs in the backward direction and the detector is often directly facing the laser termination. If a measurement target is placed close to the termination and the time gate is placed correctly, the echo from the termination could be removed. It will be the length of the laser pulse that determines how close one can place the target and still remove the termination echo. The reason for this is that, at some point, the scattering resulting from the leading edge of the laser pulse hitting the termination will interfere with the signal from the target. Initially, a laser with a pulse duration of 170 ps was to be used, giving a 5 cm pulse length. This would mean that one could place the flame within a decimeter from the termination and still be able to remove the interfering echo. Unfortunately, the ps-laser envisioned for these measurements was not working properly and a laser delivering ns pulses was used instead. This means that the pulse length was approximately 1.5 m instead of 5 cm and the demonstration thus became less illustrative. The time gating was instead used only to suppress flame emission,

which could be removed. In the future, it these kind of measurements should be performed with a laser generating picosecond pulses.

An interesting measurement concept would be to perform measurements with a pulsed ps-Lidar setup, described in e.g. [44], and simultaneously monitor the beam with a detector placed in a Scheimpflug configuration. In this way, the strength and weaknesses of the methods could be evaluated and compared, and possible ways to combine the techniques to extract more information about the measurement volume could be investigated. It would be especially interesting to study fluorescence, since it might be possible to use the two methods together to determine the fluorescence lifetimes, which degrades the range resolution for the ToF technique.

Another application in combustion research would be to use a type of detector system with spectral or temporal resolution. A hyperspectral system, as the one presented in section 7.2 could be used to gain spectral information. Another possibility would be to use a spectrometer. To be able to sharply image the signal dispersed by the spectrometer onto a detector, two Scheimpflug configurations would have to be used. The laser beam, collection optics and the slit on the spectrometer would have to be placed in a Scheimpflug configuration, as well as the slit, imaging optics in the spectrometer, and the camera detecting the dispersed signal. Just as in the system described in section 7.2, this would provide range resolution, according to the Scheimpflug and hinge rules, along one direction on the camera chip, and spectral information along the orthogonal direction.

A different way to gain spectral information would be to use multiple laser outputs, which was actually done using a mechanical chopper in the TLAF measurement described in section 7.1.2. It would be very interesting to carry out DIAL in a combustion environment using S-Lidar, in a similar way as presented in [26]. Range resolved concentration measurements of important flame species could possibly be carried out using two or more spectral bands, which corresponds to signals on and off an absorption line.

Yet another very exciting possible measurement would be to use a streak camera instead of the line-array detector when fluorescence is being detected. A streak camera [48] gives spatial information along one direction of the detector and temporal information along the other, orthogonal direction. Such measurements could thus potentially provide remote, spatially resolved fluorescence lifetimes over long distances, which would constitute unique and indeed valuable information for combustion researchers. The concept might not be entirely straight-forward to realize though since it could possibly be complex to incorporate the streak camera into the Scheimpflug geometry. The time delay, caused by the fact that we measure at different distances, would also distort the signal along the temporal direction on the detector. The impact of this distortion would depend on how the time scales of the camera streak and size of the probe volume relate to each other.

Acknowledgments

I would like to start by thanking all my current and past colleagues at the Division of Combustion Physics. It is privilege to work in a place where you, during a normal fika, can interact with people from 10-15 different countries. Thank you all for being awesome lunch companions, fellow fika enthusiasts, and interesting discussion partners. I am glad that you put up with my talkative nature and sometimes weird choice of discussion topics. I would mention you all by name but then this acknowledgement would never end.

Joakim Bood, I am very grateful to have you as my supervisor on this journey that started 6 years ago. You always take the time to listen, to answer questions or to help out in the lab, even when you have very little to spare. I am especially appreciative of all your great feedback on my writing. since it has improved my writing skills substantially. Also, your reveals of hilarious dangling modifiers (syftningsfel) are always a source of amusement. On a personal level, I have really enjoyed all our discussions about things unrelated to physics, whether the topic has been current affairs, literature or basketball. I feel like we are on the same wavelength (pun warning) when it comes to many issues which makes it easy to talk to you. Also, having a fellow basketball player at the division has been a great help when holding back the onslaught from football and handball enthusiasts.

Mikkel Brydegaard, thank you for giving me the opportunity to be involved in a truly "funky" research project which gave me the epithet "bug girl" at the biophotonic summer school at Ven. This project has allowed me travel to places, such as Ivory Coast and Tanzania, where I probably never would have gone otherwise. Your practical and technical skills can sometimes be a bit daunting, but I am very appreciative of how freely you share your knowledge. Your support and valuable feedback, as well as all your practical help during field campaigns have been of great help. I also very much appreciate your humor, your passion for music, and the fact that you dance with strange people on the sidewalk wherever you go.

Samuel Jansson, my fellow "bug boy", it has truly been a joy working with you during the last five years. Whether it is putting up with tropical heat, sleeping in uncomfortable places or working in a terrible manure smell, I feel like laughter is never far away when we work together. An exception is when we were in Ivory Coast, and we discovered that the system had been ruin by a thunderstorm during the night. Laughter felt like a very foreign concept in that moment (Hasa diga Ebowai, right?), but I am also very happy and proud that we manage to deal with that situation together.

Thanks to all my office mates. *Kajsa Larsson*, I think you already know most of the things I could write here. You were a rock and true friend during all the years we shared the office. I miss you EVERY day. *Haisol Kim,* thanks for those months we shared an office and for taking such a good care of mine and Kajsa's "grandchildren". I am super happy you stayed as a PhD student since you are such a cool, nice and thoughtful person to be around. I am also really grateful that you introduced me to the laser aligner. *Henrik Feuk,* you have had the tough job of sharing an office with me during the time I have been writing this thesis. I hope I have not affected you with any of my stress. I am very thankful for all the fika reminders and our discussions about random facts (I now know what "rolling coal" is for example).

I would like to give a special thanks to some fellow PhD students who were there from the very start. *Johan Simonsson*, I find it very impressive how you always know, or quickly find out, the answer to any question regardless of its nature, and I am very grateful to you for taking the time to help me with all my technical, graphical or IT problems. I am also glad to have found a fellow sci-fi enthusiast in you. *Jim Larsson*, thanks for being a friend even when I give you a hard time. It is lovely to discuss nerdy things with you even though we always disagree. I truly admire how genuinely engaged you are in things you find interesting or like, whether it is physics, podcasts, movies, dachshunds, or Kävlinge. I hope your hometown is appreciative of your fierce loyalty. *Jesper Borggren*, the real-life MacGyver, I am very grateful to you for taking time when you were writing your PhD thesis to stand in the dark basement lab and perform measurements with me. You made lab work seem fun again when I was feeling a bit tired of it. The measurements also resulted in quite a nice paper in the end. *Malin Jonsson*, I would like to thank you for being instrumental in me doing my master thesis at the division, which you also co-supervised. The project directly resulted in be doing my PhD at our division.

I would like to thank *Minna Ramkull*, *Cecilia Bille, Igor Buzuk* for all your administrative and technical support. *Minna*, you are truly the sunshine of the division. Whether it is by making gingerbread cookies, bringing a strange Finnish dessert, or just projecting your positive attitude, you make our place of work SO much better with your presence. Also, please thank *Lykke* for being her adorable dog self and for some strange reason reciprocating my intense love for her. *Cecilia*, thank you for being another positive and cheerful presence at the division even during periods when you have a huge workload. I am thankful to you for always answering my confused questions about how to pay for stuff.

There are also several senior researchers at the division who has directly or indirectly help and supported me over the years. *Christian Brackmann*, I am very grateful for all the help you have given me and everything you have taught me. Your willingness to discuss any problem and find a solution has been of great assistance to me many times. *Andreas Ehn*, besides your eagerness to discuss physics or other work related questions, I really appreciate that fact that you always have something interesting to say. It is sometimes infuriating (probably on purpose) but always interesting or hilarious. This,

combined with the fact that I literally know you are the kind of person who would run towards an explosion to check if everyone is ok, make me proud of once having been your "Senior Advisor". *Marcus Aldén*, I am grateful for the opportunities you and the division has given me and thankful for all your input on my articles. You are a great Head of Division, even though you are surprisingly bad at telling Scanic accents apart and possibly a bit misguided when it comes to which sport is the best. *Per-Erik Bengtsson*, thanks for providing me with fun and interesting teaching opportunities. You are always fun to talk to and I am very fond of your enthusiasm and competitiveness when it comes to sport, games and quizzes.

Sharing things is not always easy so I would also like to thank *Maria Ruchkina, Yupan Bao and Pengji Ding* for gracefully sharing the basement lab with me and my weird Lidar setup. I admire how all of you have such positive attitudes in the lab even when your laser systems are giving you huge problems.

I would like to give special acknowledgement to all my collaborators from the Biology Department, especially to *Susanne Åkesson and Jens Rydell*. *Susanne*, thanks for giving me the opportunity to go on several field campaigns with LUMBO. It is always a joy and an inspiration to listen to you when you talk about your research. *Jens*, your enthusiasm for the underappreciated members of the order Chiroptera is a delight to experience and it has made me realize that bats are probably the coolest animals around.

I would also like to take the opportunity to acknowledge my collaborators previously or currently affiliated with South China University, including but not limited to *Sune Svanberg, Katarina Svanberg, Guangyu Zhao, Shiming Zhu, Wansha Li*. Thanks for letting us come and carry out our joined field campaign in Guangzhou. It was very hot and humid but such a fun and interesting experience.

I would also like to thank *Jeremie Zoueu* and all his students and colleagues at Institut National Polytechnique Félix Houphouët-Boigny in Yamasourkro, Ivory Coast, for welcoming us to their country, their lush university campus and allowing us to practically take over a big part of their lab for two weeks.

Thanks to *Fauna Photonics* for great cooperation and exchange of ideas, especially *Alfred Strand* and *Klas Rydhmer* who were the most self-reliant and efficient master students a co-supervisor could wish for. Also thanks *to Mikael Ljungholm, Johan Källman, Alem Gebru, Mariam Andersson*, and *Alexandra Andersson* for cooperation on different Lidar related projects.

I should also thank the life size paper cut-out of Justin Bieber that was a funny/creepy resident of the lab floor for many years, since it was influential in me doing a master thesis project at the division. I saw it during a lab viewing in a course I was taking and thought: "This is a place where they do serious research without taking themselves too seriously". Never underestimate the power of humor and silliness.

Most of all, I would like to thank all of my friends and my whole family for all their love and support. *Mom* and *Dad,* thanks for always being there, and for teaching me the importance of knowledge, compassion, and cooperation at a young age. I may not always be very good at telling you, but I am incredibly proud to have you as my parents.

Funding

I would like to thank the organizations and foundations that have made this research possible:

- Swedish Energy Agency (Energimyndigheten)
- European Research Council (ERC)
- Knut and Alice Wallenberg Foundation
- The Swedish Research Council through Linnaeus grants to the Center for Animal Movement Research (CAnMove) and the Lund Laser Centre (LLC).

References

1. C. P. Kenaley, "Revision of the Stoplight Loosejaw Genus Malacosteus (Teleostei: Stomiidae: Malacosteinae), with Description of a New Species from the Temperate Southern Hemisphere and Indian Ocean," Copeia **4**, 886–900 (2007).
2. C. Weitkamp, ed., *Lidar: Range-Resolved Optical Remote Sensing of the Atmosphere* (Springer Science & Business, 2006), Vol. 102.
3. R. Measures, *Laser Remote Sensing: Fundamentals and Applications* (Krieger Publishing Company, 1984).
4. T. Fujii and T. Fukuchi, eds., *Laser Remote Sensing* (CRC press, 2005).
5. V. A. Kovalev and W. E. Eichinger, *Elastic Lidar: Theory, Practice, and Analysis Methods* (John Wiley & Sons, 2004).
6. R. O. Dubayah and J. B. Drake, "Lidar Remote Sensing for Forestry," J. For. **98**, 44–46 (2000).
7. W. Y. Yan, A. Shaker, and N. El-Ashmawy, "Urban Land Cover Classification Using Airborne LiDAR Data: A Review," Remote Sens. Environ. **158**, 295–310 (2015).
8. P. S. Argall and R. J. Sica, "Lidar," Encycl. Imaging Sci. Technol. 869–889 (2002).
9. D. M. Winker, J. R. Pelon, and M. P. McCormick, "The CALIPSO Mission: Spaceborne Lidar for Observation of Aerosols and Clouds," Proc. SPIE **4893**, 1 (2003).
10. J. Eaves and E. Reedy, *Principles of Modern Radar* (Springer Science & Business Media, 2012).
11. J. Scheer and W. A. Holm, *Principles of Modern Radar* (SciTech Publishing, 2010).
12. L. Mei and M. Brydegaard, "Atmospheric Aerosol Monitoring by an Elastic Scheimpflug Lidar System," Opt. Express **23**, A1613 (2015).
13. L. Mei and P. Guan, "Development of an Atmospheric Polarization Scheimpflug Lidar System Based on a Time-Division Multiplexing Scheme," Opt. Lett. **42**, 3562–3565 (2017).
14. M. Brydegaard, E. Malmqvist, S. Jansson, J. Larsson, S. Török, and G. Zhao, "The Scheimpflug Lidar Method," in *SPIE Proceedings* (2017), Vol. 10406.
15. L. Mei and M. Brydegaard, "Development of a Scheimpflug Lidar System for Atmospheric Aerosol Monitoring," in *EPJ Web of Conferences* (EDP Sciences, 2016), Vol. 119, p. 27005.

16. E. O. Hulbert, "Observations of a Searchlight Beam to an Altitude of 28 Kilometers," J. Opt. Soc. Am. **27**, 377–382 (1937).

17. L. Elterman, "The Measurement of Stratospheric Density Distribution with the Searchlight Technique," J. Geophys. Res. **56**, (1951).

18. L. Elterman, "Aerosol Measurements in the Troposphere and Stratosphere," J. Air Pollut. Control Assoc. **17**, 596–596 (1967).

19. C. Kirkeby, M. Wellenreuther, and M. Brydegaard, "Observations of Movement Dynamics of Flying Insects Using High Resolution Lidar," Sci. Rep. **6**, 1–11 (2016).

20. M. Brydegaard, "Advantages of Shortwave Infrared LIDAR Entomology," Imaging Appl. Opt. 2014 LW2D.6 (2014).

21. M. Brydegaard, "Towards Quantitative Optical Cross Sections in Entomological Laser Radar – Potential of Temporal and Spherical Parameterizations for Identifying Atmospheric Fauna," PLoS One **10**, (2015).

22. S. Zhu, E. Malmqvist, W. Li, S. Jansson, Y. Li, Z. Duan, K. Svanberg, H. Feng, Z. Song, G. Zhao, M. Brydegaard, and S. Svanberg, "Insect Abundance over Chinese rice Fields in Relation to Environmental Parameters, Studied with a Polarization-Sensitive CW Near-IR Lidar System," Appl. Phys. B Lasers Opt. **123**, 1–11 (2017).

23. G. Sun, L. Qin, Z. Hou, X. Jing, H. Feng, F. Tan, and S. Zhang, "Small-scale Scheimpflug Lidar for Aerosol Extinction Coefficient and Vertical Atmospheric Transmittance Detection," **26**, 3908–3910 (2018).

24. L. Mei, Z. Kong, and P. Guan, "Implementation of a Violet Scheimpflug Lidar System for Atmospheric Aerosol Studies," Opt. Express **26**, A260–A274 (2018).

25. G. Zhao, E. Malmqvist, S. Török, P. . E. Bengtsson, S. Svanberg, J. Bood, and M. Brydegaard, "Particle Profiling and Classification by a Dual-Band Continuous-Wave Lidar System," Appl. Opt. **57**, 10164–10171 (2018).

26. L. Mei and M. Brydegaard, "Continuous-Wave Differential Absorption Lidar," Laser Photonics Rev. **9**, 629–636 (2015).

27. E. Siemann and W. . Weisser, *The Various Effects of Insects on Ecosystem Functioning* (Springer, 2004), Vol. 173.

28. *World Malaria Report 2018* (2018).

29. J. L. Gallup and J. D. Sachs, "The Economic Burden of Malaria," Am. J. Trop. Med. Hyg. **64**, 85–96 (2001).

30. E. Worrall, S. Basu, and K. Hanson, "Is Malaria a Disease of Poverty? A Review of the Literature," Trop. Med. Int. Heal. **10**, 1047–1059 (2005).

31. H. M. Ferguson, A. Dornhaus, A. Beeche, C. Borgemeister, M. Gottlieb, M. S. Mulla, J. E. Gimnig, D. Fish, and G. F. Killeen, "Ecology : A Prerequisite for Malaria Elimination and Eradication," PLoS One Med. **7**, 1–7 (2010).

32. J. W. Chapman, V. A. Drake, and D. R. Reynolds, "Recent Insights from Radar Studies of Insect Flight," Annu. Rev. ofEntomology **56**, 337–356 (2011).

33. V. A. Drake and D. R. Reynolds, *Radar Entomology: Observing Insect Flight and Migration* (Cabi, 2012).

34. V. A. Drake, "Distinguishing Target Classes in Observations from Vertically Pointing Entomological Radars," Int. J. Remote Sens. **37**, 3811–3835 (2016).

35. J. A. Shaw, N. L. Seldomridge, D. L. Dunkle, P. W. Nugent, L. H. Spangler, J. J. Bromenshenk, C. B. Henderson, J. H. Churnside, and J. J. Wilson, "Polarization Lidar Measurements of Honey Bees in Flight for Locating Land Mines," Opt. Express **13**, 5853 (2005).

36. K. S. Repasky, J. A. Shaw, R. Scheppele, C. Melton, J. L. Carsten, and L. H. Spangler, "Optical Detection of Honeybees by Use of Wing-Beat Modulation of Scattered Laser Light for Locating Explosives and Land Mines," Appl. Opt. **45**, 1839 (2006).

37. D. S. Hoffman, A. R. Nehrir, K. S. Repasky, J. A. Shaw, and J. L. Carlsten, "Range-Resolved Optical Detection of Honeybees by Use of Wing-Beat Modulation of Scattered Light for Locating Land Mines," Appl. Opt. **46**, 3007 (2007).

38. M. J. Tauc, K. M. Fristrup, K. S. Repasky, and J. A. Shaw, "Field Demonstration of a Wing-Beat Modulation Lidar for the 3D Mapping of Flying Insects," OSA Contin. **2**, 332–348 (2019).

39. M. Brydegaard, A. Gebru, and S. Svanberg, "Super Resolution Laser Radar with Blinking Atmospheric Particles - Application to Interacting Flying Insects," Prog. Electromagn. Res. **147**, 141–151 (2014).

40. M. Brydegaard, A. Merdasa, A. Gebru, H. Jayaweera, and S. Svanberg, "Realistic Instrumentation Platform for Active and Passive Optical Remote Sensing," **70**, 372–385 (2016).

41. J. Warnatz, U. Maas, and R. W. Dibble, *Combustion Physical and Chemical Fundamentals, Modeling and Simulation, Experiments, Pollutant Formation*, 4th ed. (Springer-Verlag Berlin Heidelberg, 2006).

42. A. C. Eckbreth, *Laser Diagnostics for Combustion Temperature and Species* (CRC Press, 1996), Vol. 3.

43. A. McIlroy, J. B. Jeffries, K. Kohse-Höinghaus, and J. B. Jeffries, *Applied Combustion Diagnostics* (Taylor and Francis, New York, 2002).

44. B. Kaldvee, A. Ehn, J. Bood, and M. Aldén, "Development of a Picosecond Lidar System for Large-Scale Combustion Diagnostics.," Appl. Opt. **48**, B65–B72 (2009).

45. B. Kaldvee, J. Wahlqvist, M. Jonsson, C. Brackmann, B. Andersson, P. van Hees, J. Bood, and M. Alden, "Room-Fire Characterization Using Highly Range-Resolved Picosecond Lidar Diagnostics and CFD Simulations," Combust. Sci. Technol. **185**, 749–765 (2013).

46. B. Kaldvee, J. Bood, and M. Aldén, "Picosecond-Lidar Thermometry in a Measurement Volume Surrounded by Highly Scattering Media," Meas. Sci. Technol. **22**, (2011).

47. B. Kaldvee, C. Brackmann, M. Aldén, and J. Bood, "Highly Range-Resolved Ammonia Detection Using Near-Dield Picosecond Differential Absorption Lidar.," Opt. Express **20**, 20688–97 (2012).

48. B. Kaldvee, "Development and Application of Single-Ended Picosecond Laser Diagnostics," Lund University (2012).

49. W. H. Mcmaster, "Polarization and the Stokes Parameters," Am. J. Phys. **22**, 351–362 (1954).

50. S. L. Jacques, "Polarized Light Imaging of Biological Tissues," in *Handbook of Biomedical Optics*, D. A. Boas, C. Pitris, and N. Ramanujam, eds. (CRC Press, Boca Raton, FL, 2011), pp. 649–669.

51. R. B. Miles, W. R. Lempert, and J. N. Forkey, "Laser Rayleigh Scattering Review," Meas. Sci. Technol. **12**, 33–51 (2001).

52. M. I. Mishchenko, L. D. Travis, and A. A. Lacis, *Scattering, Absorption, and Emission of Light by Small Particles* (Cambridge university press, 2002).

53. W. Demtröder, *Atoms, Molecules, and Photons*, 2nd ed. (Springer, 2006).

54. M. Aldén, J. Bood, Z. Li, and M. Richter, "Visualization and understanding of combustion processes using spatially and temporally resolved laser diagnostic techniques," Proc. Combust. Inst. **33**, 69–97 (2011).

55. J. Borggren, W. Weng, A. Hosseinnia, P.-E. Bengtsson, M. Aldén, and Z. Li, "Diode Laser-Based Thermometry Using Two-Line Atomic Fluorescence of Indium and Gallium," Appl. Phys. B Lasers Opt. **123**, 1–10 (2017).

56. I. S. Burns, X. Mercier, M. Wartel, R. S. M. Chrystie, J. Hult, and C. F. Kaminski, "A Method for Performing High Accuracy Temperature Measurements in Low-Pressure Sooting Flames Using Two-Line Atomic Fluorescence," Proc. Combust. Inst. **33**, 799–806 (2011).

57. B. E. A. Saleh, M. C. Teich, and B. E. Saleh, *Fundamentals of Photonics* (Wiley New York, 1991), Vol. 22.

58. W. J. Smith, *Modern Optical Engineering* (2007).

59. A. Gebru, S. Jansson, R. Ignell, C. Kirkeby, J. C. Prangsma, and M. Brydegaard, "Multiband Modulation Spectroscopy for the Determination of Sex and Species of Mosquitoes in Flight," J. Biophotonics **11**, 1–13 (2018).

60. O. Sotavalta, "Flight-Tone and Wing-Stroke Frequency of Insects and the Dynamics of Insect Flight," Nature **170**, 1057 (1952).

61. R. F. Chapman, *The Insects: Structure and Function*, 5th ed. (Cambridge Univeristy Press, 2012).

62. A. R. Parker and N. Martini, "Structural Colour in Animals - Simple to Complex Optics," Opt. Laser Technol. **38**, 315–322 (2006).

63. S. A. Combes, "Materials, Structure, and Dynamics of Insect Wings as Bioinspiration for MAVs," Encycl. Aerosp. Eng. 1–10 (2010).

64. E. Shevtsova, C. Hansson, D. H. Janzen, and J. Kjaerandsen, "Stable Structural Color Patterns Displayed on Transparent Insect wings," Proc. Natl. Acad. Sci. **108**, 668–673 (2011).

65. N. Katayama, J. K. Abbott, J. Kjærandsen, Y. Takahashi, and E. I. Svensson, "Sexual Selection on Wing Interference Patterns in Drosophila melanogaster," Proc. Natl. Acad. Sci. **111**, 15144–15148 (2014).

66. A. Gebru, M. Brydegaard, E. Rohwer, and P. Neethling, "Probing Insect Backscatter Cross Section and Melanization Using kHz Optical Remote Detection System," J. Appl. Remote Sens. **11**, 016015 (2017).

67. K. Peiris, B. Drolet, L. Cohnstaedt, and F. Dowell, "Infrared Absorption Characteristics of *Culicoides sonorensis* in Relation to Insect Age," Am. J. Agric. Sci. Technol. **2**, 49–61 (2014).

68. V. S. Mayagaya, K. Michel, M. Q. Benedict, G. F. Killeen, R. A. Wirtz, H. M. Ferguson, and F. E. Dowell, "Non-Destructive Determination of Age and Species of *Anopheles gambiae* s.l. Using Near-Infrared Spectroscopy," Am. J. Trop. Med. Hyg. **81**, 622–630 (2009).

69. Z. S. Li, B. Li, Z. W. Sun, X. S. Bai, and M. Aldén, "Turbulence and Combustion Interaction : High Resolution Local Flame Front Structure Visualization Using Simultaneous Single-Shot PLIF Imaging of CH , OH , and CH_2O in a Piloted Premixed Jet Flame," Combust. Flame **157**, 1087–1096 (2010).

70. M. Richter, Z. Li, J. Rosell, and M. Alde, "Simultaneous Burst Imaging of Dual Species Using Planar Laser-Induced Fluorescence at 50 kHz in Turbulent Premixed Flames," Appl. Spectrosc. **71**, 1363–1367 (2017).

71. C. M. Vagelopoulos and J. H. Frank, "An Experimental and Numerical Study on the Adequacy of CH as a Flame Marker in Premixed Methane Flames," Proc. Combust. Inst. **30**, 241–249 (2005).

72. H. A. Michelsen, C. Schulz, G. J. Smallwood, and S. Will, "Laser-Induced Incandescence: Particulate Diagnostics for Combustion, Atmospheric, and Industrial Applications," Prog. Energy Combust. Sci. **51**, 2–48 (2015).

73. J. Carpentier, "Improvements in Enlarging or Like Cameras," GB Pat. No.1139 (1901).

74. T. Scheimpflug, "Improved Method and Apparatus for the Systematic Alteration or Distortion of Plane Pictures and Images by Means of Lenses and Mirrors for Photography and for Other Purposes," GB Pat. No.1196 (1904).

75. H. Mayer, "Theodor Scheimpflug His Personality and Lifework," Ophthalmic Res **26**, 3–9 (1994).

76. U. Wandinger and A. Ansmann, "Experimental Determination of the Lidar Overlap Profile with Raman Lidar," Appl. Opt. **41**, 511–514 (2002).

77. J. Guerrero-Rascado and M. Costa, "Infrared Lidar Overlap Function: an Experimental Determination," Opt. Express **18**, 20350–20359 (2010).

78. G. Biavati, G. Di Donfrancesco, F. Cairo, and D. G. Feist, "Correction Scheme for Close-Range Lidar Returns," Appl. Opt. **50**, 5872–5882 (2011).

79. K. F. Renk, *Basics of Laser Physics* (Springer-Verlag Berlin Heidelberg, 2012).

80. C. C. Davis, *Lasers and Electro-Optics: Fundamentals and Engineering* (Cambridge university press, 2014).

81. K. B. MacAdam, A. Steinbach, and C. Wieman, "A Narrow-Band Tunable Diode Laser System with Grating Feedback, and a Saturated Absorption Spectrometer for Cs and Rb," Am. J. Phys. **60**, 1098–1111 (1992).

82. M. Andersson, "Short-Wave Infrared Lidar on Atmospheric Aerosols," Lund University (2017).

83. E. Warrant, *Invertebrate Vision* (Elsevier Ltd., 1980), Vol. 283.

84. A. D. Briscoe and L. Chittka, "The Evolution of Color Vision in Insects," Annu. Rev. Entomol. **46**, 471–510 (2001).

85. J. R. Riley, "Angular and Temporal Variations in the Radar Cross-Sections of Insects," in *Proceedings of the Institution of Electrical Engineers* (IET, 1973), Vol. 120, pp. 1229–1232.

86. S. Jansson, P. Atkinson, R. Ignell, and M. Brydegaard, "First Polarimetric Investigation of Malaria Mosquitoes as Lidar Targets," IEEE J. Sel. Top. Quantum Electron. **25**, 1–8 (2019).

87. M. Brydegaard, A. Gebru, C. Kirkeby, S. Akesson, and H. Smith, "Daily Evolution of the Insect Biomass Spectrum in an Agricultural Landscape Accessed with Lidar," ILRC27 Proc. 2–5 (2015).

88. D. R. Reynolds and J. R. Riley, *Flight Behaviour and Migration of Insect Pests. Radar Studies in Developing Countries.* (Natural Resources Institute (NRI), 1997).

89. J. Eklöf, "Vision in Echolocating Bats," Göteborg University (2003).

90. J. Rydell and L. Bach, "Mortality of Bats at Wind Turbines Links to Nocturnal Insect Migration ?," 823–827 (2010).

91. J. Rydell, L. Bach, M.-J. Dubourg-Savage, M. Green, L. Rodrigues, and A. Hedenström, "Bat Mortality at Wind Turbines in Northwestern Europe," Acta Chiropterologica **12**, 261–274 (2010).

92. M. Brydegaard, "New Mobile Observatory for Aero-Fauna Studies," SPIE Newsroom 8–11 (2015).

93. S. Jansson, E. Malmqvist, M. Brydegaard, J. Rydell, and S. Åkesson, "Occurrence of Insects and Bats at Wind Farms as Revealed by Scheimpflug Lidar," in prep. (2019).

94. A. Moore, "Automated Identification of Optically Sensed Aphid (Homoptera : Aphidae) Wingbeat Waveforms," (2002).

95. W. G. Brogdon, "Measurement of Flight Tone Differentiates Among Members of the *Anopheles gambiae* Species Complex (Diptera : Culicidae)," 681–684 (1998).

96. Y. Chen, A. Why, G. Batista, A. Mafra-Neto, and E. Keogh, "Flying Insect Classification with Inexpensive Sensors," J. Insect Behav. **27**, 657–677 (2014).

97. P. Stoica and Y. Sel, "Model-Order Selection A Review of Information Criterion Rules," IEEE Signal Process. Mag. **21**, 36–47 (2004).

98. A. Andersson, "Unbiasing Entomological kHz Scheimpflug LIDAR Data," Lund University (2018).

99. A. Runemark, M. Wellenreuther, H. H. E. Jayaweera, S. Svanberg, and M. Brydegaard, "Rare Events in Remote Dark-Field Spectroscopy: An Ecological Case Study of Insects," IEEE J. Sel. Top. Quantum Electron. **18**, 1573–1582 (2012).

100. A. Gebru, E. Rohwer, P. Neethling, and M. Brydegaard, "Investigation of Atmospheric Insect Wing-Beat Frequencies and Iridescence Features Using a Multispectral kHz Remote Detection System," J. Appl. Remote Sens. **8**, 083503 (2014).

101. S. Jansson and M. Brydegaard, "Passive kHz Lidar for the Quantification of Insect Activity and Dispersal," Anim. Biotelemetry 1–10 (2018).

102. E. Kristensson, A. Ehn, J. Bood, and M. Alde, "Advancements in Rayleigh Scattering Thermometry by Means of Structured Illumination," in *Proceedings of the Combustion Institute* (2015), Vol. 35, pp. 3689–3696.

103. E. Herrala, J. T. Okkonen, T. S. Hyvarinen, M. Aikio, and J. Lammasniemi, "Imaging spectrometer for process industry applications," in *Optical Measurements and Sensors for the Process Industries* (International Society for Optics and Photonics, 1994), Vol. 2248, pp. 33–41.

104. X. Wang, Z. Duan, M. Brydegaard, S. Svanberg, and G. Zhao, "Drone-Based Area Scanning of Vegetation Fluorescence Height Profiles Using a Miniaturized Hyperspectral Lidar System," Appl. Phys. B **124**, 207 (2018).

105. F. Gao, J. Li, H. Lin, and S. He, "Oil Pollution Discrimination by an Inelastic Hyperspectral Scheimpflug Lidar System," Opt. Express **25**, 25515–25522 (2017).

106. M. Brydegaard, J. Larsson, S. Török, E. Malmqvist, G. Zhao, S. Jansson, M. Andersson, S. Svanberg, S. Åkesson, and F. Laurell, "Short-Wave Infrared Atmospheric Scheimpflug Lidar," in *EPJ Web of Conferences* (EDP Sciences, 2018), Vol. 176.

107. Z. Guan, M. Brydegaard, P. Lundin, M. Wellenreuther, A. Runemark, E. I. Svensson, and S. Svanberg, "Insect Monitoring with Fluorescence Lidar Techniques: Field Experiments," Appl. Opt. **49**, 5133–42 (2010).

Summary of papers

Paper I **E. Malmqvist, S. Jansson, S. Török, M. Brydegaard, "Effective parameterization of laser radar observations of atmospheric fauna",**
In this paper, the method we use for extracting fauna observations from atmospheric Lidar data and reducing the observations to a set of descriptive parameters is described. Kilohertz-Lidar data are used, the essential steps are walked through and a glimpse of the obtainable data product is presented.
I evaluated the data, with input from Mikkel Brydegaard and Samuel Jansson. I made all the figures and wrote the manuscript with input from the other authors.

Paper II **G. Zhao, M. Ljungholm, E. Malmqvist, G. Bianco, L.A, Hansson, S. Svanberg, M. Brydegaard. "Inelastic hyperspectral Lidar for profiling aquatic ecosystems",**
An aquatic laser-diode-based inelastic light detection and ranging (Lidar) system with spatiotemporal resolution and number of spectral bands, is presented. Elastic as well as molecular ranging is demonstrated by using the water Raman band, and by observing fluorescence from chlorophyll and from dye-tagged organisms.
I contributed to the experiments, instrumentation and had inputs on the manuscript. I co-supervised the master student who carried out the pilot studies with the system.

Paper III **M. Brydegaard, E. Malmqvist, S. Jansson, J. Larsson, S. Török, G. Zhao. "The Scheimpflug Lidar method"**
A review over the applications of Scheimpflug Lidar method is presented. A raytracing program used to simulate Scheimpflug Lidar signals for a beam with finite width is described as well as elastic and inelastic application of the method, e.g. atmospheric research (DIAL, aerosols), entomology, diagnostics of industrial and combustion processes, and monitoring of aquatic fauna and of vegetation.
I carried out the measurements and data evaluation for the combustion applications. I took part in the field campaign resulting in the polarimetric Lidar data and made the data evaluation. Contributed to the experiments

and instrumentation for the aquatic applications. I had input on the manuscript.

Paper IV **E. Malmqvist, S. Jansson, S.Zhu, Li, W, Svanberg, K, Svanberg, J. Rydell, Z. Song, J. Bood, M. Brydegaard, S. Åkesson. "The bat-bird-bug battle: Daily flight activity of insects and their predator over a rice field revealed by high-resolution Scheimpflug Lidar "**

The paper presents the results of the first Lidar study applied to continuous and simultaneous monitoring of aerial insects, bats and birds. It illustrates how common patterns of flight activity, e.g. insect swarming around twilight, depend on predation risk and other constraints acting on the faunal components. Flight activity was monitored over a rice field in China during one week in July 2016, using a high-resolution Scheimpflug Lidar system.

I participated in the field experiments in China. I carried out the data evaluation with input from Samuel Jansson and Mikkel Brydegaard. I made all the figures. I was main responsible for the manuscript. Me and Jens Rydell wrote the manuscript with input from Susanne Åkesson and the other authors.

Paper V **E. Malmqvist, M. Brydegaard, M. Aldén, J. Bood. "Scheimpflug Lidar for combustion diagnostics"**

A portable Lidar system developed for large-scale (~1-20 m) combustion diagnostics is described and demonstrated. The system is able to perform remote backscattering measurements with range and temporal resolution. Results from simulations of the range capabilities and range resolution of the system are presented and its temporal resolution is also discussed. Various applications, important for combustion diagnostics, are also demonstrated, including Rayleigh scattering thermometry, aerosol detection and laser-induced fluorescence measurements.

I built the instrumentation, planned and carried out the experiments with help from Joakim Bood and Mikkel Brydegaard. I evaluated the data and made the figures. I wrote the manuscript with help from Joakim Bood, and with input from the other authors.

Paper VI **E. Malmqvist, J. Borggren, M. Aldén, J. Bood. "Lidar thermometry using two-line atomic fluorescence"**

In this paper, Scheimpflug Lidar has been combined with the thermometric technique two-line atomic fluorescence, to carry out stand-off, spatially resolved temperature measurements. One-dimensional flame temperature profiles were measured at different

heights above a porous-plug burner, located at a distance of 1.5 m from the Lidar system. The technique was also used to demonstrate two-dimensional temperature measurements in the same flame.
Me and Jesper Borggren planned and carried out the experiments with input from Joakim Bood. Jesper and I carried out the data analysis. I made the figures. The manuscript was written by me, with input from Joakim and the other authors.

Appendix A:

Equations

The equations describing the range and resolution of Scheimpflug-Lidar are derived in this Appendix.

A1. Range equation

From Fig. *A1* it is clear that the horizontal range for a pixel, z_{pix}, is:

$$z_{pix} = \frac{D}{\tan(\gamma_{pix})} \tag{A1}$$

To attain z_{pix}, the distance D and the sampling angle γ_{pix} must be found from the known system parameters; the detector angle, α, the length of detector, l_{det}, the pixel width, l_{pix}, the pixel number, m, and the focal length, f. First of all, the angle ϕ is found:

$$tan(\phi) = \frac{a - f_{rec}}{\frac{f_{rec}}{tan(\alpha)}} = \left[thin\ lens\ formula: a = \frac{f_{rec} b}{b - f_{rec}}\right] = \frac{f_{rec} tan(\alpha)}{b - f_{rec}} \rightarrow$$

$$\phi = arctan\left(\frac{f_{rec} tan(\alpha)}{b - f_{rec}}\right) \tag{A2}$$

With this angle, D may be derived:

$$sin(\phi) = \frac{D}{J} \rightarrow D = J * sin(\phi) = \left[J = \frac{b}{tan(\alpha)}\right] = \frac{b}{tan(\alpha)} * sin(\phi) \tag{A3}$$

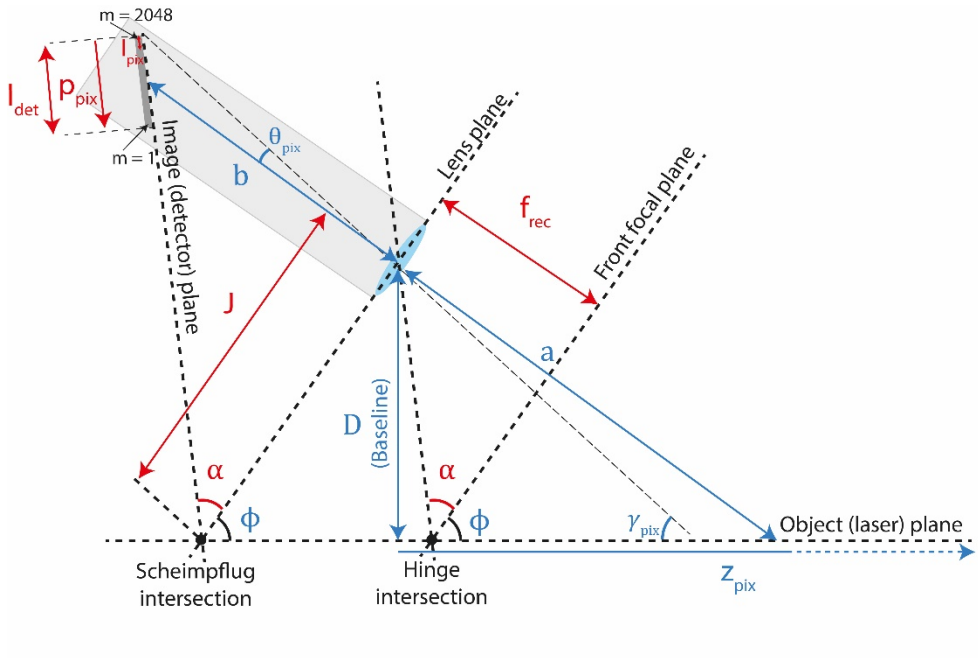

Figure A1. *Schematic of a scheimpflug Lidar setup defining the directions, angles and distances needed to derive the equations for range and resolution.*

The position of the pixels along the detector is:

$$p_{pix} = ml_{pix} - \frac{l_{det}}{2}, \tag{A4}$$

where the center of the detector corresponds to p_{pix}.= 0. The positions of the pixel projected onto the optical axis ($p_{pix,y}$ and $p_{pix,x}$ positions) must be determined:

$$p_{pix,y} = p_{pix}\, cos(\alpha) \tag{A5}$$

$$p_{pix,x} = b + p_{pix} sin(\alpha) \tag{A6}$$

With the definitions in Eq. A4, A5, and A6, the pixels with the positions corresponding to a low m will observe far ranges while the pixels with high n will observe short ranges. Eq. A5 and A6 can then be used to obtain the angle, θ_{pix}, between the pixel and the optical axis:

$$tan(\theta_{pix}) = \frac{p_{pix,y}}{p_{pix,x}} \tag{A7}$$

Using Eq. A5 and A6 in A7 results in:

$$tan(\theta_{pix}) = \frac{p_{pix}\, cos(\alpha)}{b + p_{pix} sin(\alpha)} \tag{A8}$$

The angle at which the pixel observe the laser beam can now be demined:

$$\gamma_{pix} = \frac{\pi}{2} - \phi + \theta_{pix} \rightarrow \tag{A9}$$

$$tan(\gamma_{pix}) = tan\left(\frac{\pi}{2} - \phi + \theta_{pix}\right) \tag{A10}$$

By using trigonometrical rules and substituting Eq. A8 into Eq. A10:

$$\tan(\gamma_{pix}) = \frac{\tan\left(\frac{\pi}{2} - \phi\right) + \tan(\theta_{pix})}{1 - \tan\left(\frac{\pi}{2} - \phi\right)\tan(\theta_{pix})} = \frac{b \cdot \tan\left(\frac{\pi}{2} - \phi\right) + p_{pix}\left[sin(\alpha) \cdot \tan\left(\frac{\pi}{2} - \phi\right) + cos(\alpha)\right]}{b + p_{pix}\left[sin(\alpha) - cos(\alpha) \cdot \tan\left(\frac{\pi}{2} - \phi\right)\right]} \tag{A11}$$

A full expression for the range of a pixel, z_{pix}, can now be derived, by substituting equation A11 into A1:

$$z_{pix} = \frac{D}{\tan(\gamma_{pix})} = D \cdot \frac{b + p_{pix}\left[sin(\alpha) - cos(\alpha) \cdot \tan\left(\frac{\pi}{2} - \phi\right)\right]}{b \cdot \tan\left(\frac{\pi}{2} - \phi\right) + p_{pix}\left[sin(\alpha) \cdot \tan\left(\frac{\pi}{2} - \phi\right) + cos(\alpha)\right]} =$$

$$= D \cdot \frac{b + p_{pix}[sin(\alpha) - cos(\alpha) \cdot \cot(\phi)]}{b \cdot \cot(\phi) + p_{pix}[sin(\alpha) \cdot \cot(\phi) + cos(\alpha)]} \tag{A12}$$

Where ϕ is given by Eq. A2, D is given by Eq. A3, and p_{pix} is given by Eq. A4. If the system is focused on optical infinity, b can be determined since the distance between the lens and pixel monitoring infinity, along the optical axis, is equal to f_{rec}. For instance, when infinity is placed at the end of the detector, b is:

$$b = f_{rec} + \frac{l_{det}}{2} sin(\alpha)\,, \tag{A13}$$

and ϕ becomes:

$$\phi = arctan\left(\frac{f_{rec} tan(\alpha)}{f_{rec} + \frac{l_{det}}{2} sin(\alpha) - f_{rec}}\right) = arctan\left(\frac{2 f_{rec}}{l_{det}\ cos(\alpha)}\right) \tag{A14}$$

When $f_{rec} >> l_{det}$:

$$\phi \approx \frac{\pi}{2} \rightarrow z_{pix} \approx \ D \cdot \frac{b + p_{pix} sin(\alpha)}{p_{pix}\, cos(\alpha)} = \frac{D}{tan(\theta_{pix})} \qquad (A15)$$

where:

$$p_{pix} = l_{det} - ml_{pix}$$

If infinity is not placed on the detector, a reference signal from a hard target at a known range, may be used to determine b. When b has been determined, the range of all the pixels can be obtained.

A2. Resolution

To obtain an expression for the range resolution, dz_{pix}, the derivative of z_{pix} may be found, by using the division rule and then substitute z_{pix}^2 obtained from Eq. A12 into the result. This gives:

$$dz_{pix} = \frac{-z_{pix}^2 \mathrm{bcos}(\alpha)[1 + \cot^2(\phi)]}{D^2 \left[b + p_{pix}[sin(\alpha) - cos(\alpha) \cdot \cot(\phi)]\right]^2} dp_{pix} \rightarrow \qquad (A16)$$

$$\left[A = D^2[sin(\alpha) - cos(\alpha) \cdot \cot(\phi)]\right]$$

$$\left[B = -z_{pix}^2 \mathrm{bcos}(\alpha)[1 + \cot^2(\phi)]\right]$$

$$\rightarrow \ dz_n = \frac{z_{pix}^2 B}{\left[D^2 b + p_{pix} A\right]^2} \qquad (A17)$$

Appendix B:

Scheimpflug vs ToF Lidar

Table B1. Properties of Scheimpflug-Lidar compared with ToF-Lidar. The range resolution of S-Lidar is limited by imaging properties while the resolution in ToF-Lidar depends on temporal properties. The limiting factors of the resolution during transmittance of the beam, the collection of the signal and the sampling are presented. PSF is refering to the point spread functions of the telescopes.

	Signal intensity	**Range resolution**	**Limiting factor of range resolution**		
			Transmitter	**Receiver**	**Sampling**
S-Lidar	Constant	Tangential	Beam width, PSF	FoV, PSF	Pixel pitch (width)
ToF-Lidar	$1/z^2$	Constant	Pulse duration	Bandwidth	Sampling rate

Appendix C:

Assembling and aligning a system

This is a point-by-point description of how to assemble and align a typical systems utilized for fauna monitoring in this work. Here it is assumed that the length of the baseline (distance between transmitter and receiver) has been calculated, and the holders for the telescopes have been attached at the right positions on the aluminum bar. This description is made for a system that use a Glaz sensor and its software, but the approach should be similar with any line-array detector.

C1. List of terms

Transmitter: The telescope which expands and transmits the telescope.

Monitor: The middle telescope where the monitor camera should be.

Receiver: The Newton telescope with which the signal is collected and detected with the line array camera.

Monitor camera: 2D sensor used to observe how the laser beam propagates

Line-scan camera: Glaz sensor which records the signal.

Tripod: Motorized equatorial mount (Sky-Watcher, EQ8) holding the whole system.

Bar: Aluminum cross bar on which the telescope mounts are attracted.

Driver: Laser driver controlling current and modulation of laser.

C2. Putting up the system and balancing the mount

1. Place the telescopes on the aluminium bar when it is off the tripod to check the balance both along the bar and along the telescopes. Remember to put both cameras and the laser on the telescopes or the balance will not be right.
2. Mark approximately where the telescopes should be to be balanced on the bar.
3. Take off the telescopes from the bar.
4. Make sure the two axes on the tripod are not locked.
5. Place it at the balance point you found in step 1.
6. Place the telescopes on the bar at the balance positions you have found in step 2 and put the cameras and laser in place.
7. Start with balancing the whole telescope mount (bar + telescope) with the tripod's counter weights. Check so it is balanced in several positions. If it is not, move the counterweights to balance the system.
8. Put the counterweight rod parallel to the ground and check if the system is balanced in the other axis. If the whole aluminum bar rotates when it is placed horizontally to the ground, you need to adjust the position of the telescope that weighs it down.
9. When all axes are balanced, lock the axes.
10. Connect the tripod to a power supply.
11. Turn on the tripod.

C3. Aligning the system on termination

The best time to align the system is during twilight (morning or evening) when it is dark but you can still see. It is hard to see the laser spot with the monitor camera during the day and it is hard to find the termination when it is too dark.

1. Remove the line-array camera from the Newton telescope and place the monitor camera there instead.
2. Move the telescope mount with the tripod controller so the Newton telescope is looking straight at the termination. That is, the termination should be exactly in the middle of the monitor camera image. Turn the knobs on the focal stage to find focus.

3. Remove the monitor camera from the Newton telescope and put the line-array camera back. The back of the camera (where the coaxial connectors are located) should be pointing in the forward direction, and the plane of the camera should be aligned with the transmitter telescope.
4. Remove the laser from the transmitter telescope and put the monitor camera there.
5. Use the adjustment screws on the holder of the transmitter telescope (NOT the tripod controller) to find the termination and place it in the center of the image.
6. Turn the knobs on the focal stage to find focus.
7. Put the monitor camera in the monitor telescope and use the adjustment screws on its holder to find the termination and place it in the center of the camera image.
8. During the day a filter should be used in front of the monitoring camera.
9. Put the laser back in the transmitter telescope.
10. Now the system should be VERY roughly aligned.
11. Connect the laser driver to a power supply with the correct voltage.
12. Connect the laser to the driver. Make extra sure the polarity is correct or you will burn the laser.
13. Turn on the program (Glaz UI) controlling the line array camera.
    a. If you want to trigger the system internally (camera is master) connect the "sync" port on the camera to the "strobe" port on the laser driver with a coaxial cord. Put the trigger tab in the program to "Internal". Put trigger delay to 50 microseconds. The sampling rate may be set in the program (4-4000 Hz). If one laser is used and background subtraction is enabled, the effective sampling rate will be half of this number.
    b. If you want to trigger externally, connect the "trig" port on the camera to the to the external source, i.e. a DAQ. Connect the same port on the DAQ to the "strobe" port on the laser driver. In this case the maximum allowed integration time has to be calculated and 30 microseconds should be subtracted from this value (1 / (sampling frequency) - 30 μs).
14. Make sure that the boxes "remove background", "flip pixel order", and "loop" are checked in the program.

15. Make sure the save box is unchecked so you are not saving files during alignment.
16. Set the number of slots in the program to 2 if you only have one laser or 3 if you have 2 lasers.
17. Turn on the laser by turning the key on the driver.
18. Hopefully the laser spot will show up on the termination. If it is not in the center of the termination, then place it there with the adjustment screws on the transmitter telescope holder.
19. Focus the laser on the termination by turning the knobs on the focal stage.
20. A peak representing the termination should now show up on the linear-array camera.
21. Place this peak in the middle of the sensor by turning the adjustment screws on the transmitter telescope holder.
22. This may move the laser off the termination; use the tripod controller to move it back while looking at the monitor camera.
23. Try to make this peak as narrow as possible by changing the focus of the linear array camera and possibly of the laser.
24. Use the adjustment screws on the holder to the transmitter telescope to move the termination peak to the end of the sensor
25. Try to optimize the focus of the line-array camera and the laser once again. You can also try to rotate the line-scan camera to improve the signal.
26. You should have a narrow peak at the termination position and an air signal from the whole range. This air signal is often increasing somewhat from short ranges to far ranges.
27. If focus is achieved, there should hopefully also be insect observations over the whole range showing up as narrow peaks.
28. When the system is aligned, select a folder to save to in the program, select a name for the files, and remember to check the save box.

Printed by Media-Tryck, Lund 2019 NORDIC SWAN ECOLABEL 3041 0903

LUND UNIVERSITY

Faculty of Engineering
Department of Physics
Lund University
Lund Reports on Combustion Physics, LRCP-218
ISBN 978-91-7753-995-7 (print)
ISBN 978-91-7753-996-4 (pdf)
ISSN 1102-8718
ISRN LUTFD2/TFCP-218-SE